Measurements and Control of Charge Transport through Single DNA Molecules via STM Break Junction Technique

by

Limin Xiang

A Dissertation Presented in Partial Fulfillment
of the Requirements for the Degree
Doctor of Philosophy

Approved March 2016 by the
Graduate Supervisory Committee:

Nongjian Tao, Chair
Ian Gould
Stuart Lindsay

ARIZONA STATE UNIVERSITY

May 2016

ABSTRACT

Charge transport in molecular systems, including DNA (Deoxyribonucleic acid), is involved in many basic chemical and biological processes. Studying their charge transport properties can help developing DNA based electronic devices with many tunable functionalities. This thesis investigates the electric properties of double-stranded DNA, DNA G-quadruplex and dsDNA with modified base.

First, double-stranded DNA with alternating GC sequence and stacked GC sequence were measured with respect to length. The resistance of DNA sequences increases linearly with length, indicating a hopping transport mechanism. However, for DNA sequences with stacked GC, a periodic oscillation is superimposed on the linear length dependence, indicating a partial coherent transport. The result is supported by the finding of delocalization of the highest occupied molecular orbitals of Guanines from theoretical simulation and by fitting based on the Büttiker's theory.

Then, a DNA G4-duplex structures with a G-quadruplex as the core and DNA duplexes as the arms were studied. Similar conductance values were observed by varying the linker positions, thus a charge splitter is developed. The conductance of the DNA G-tetrads structures was found to be sensitive to the π-stacking at the interface between the G-quadruplex and DNA duplexes by observing a higher conductance value when one duplex was removed and a polyethylene glycol (PEG) linker was added into the interface. This was further supported by molecular dynamic simulations.

Finally, a double-stranded DNA with one of the bases replaced by an anthraquinone group was studied via electrochemical STM break junction technique.

Anthraquinone can be reversibly switched into the oxidized state or reduced state, to give a low conductance or high conductance respectively. Furthermore, the thermodynamics and kinetics properties of the switching were systematically studied. Theoretical simulation shows that the difference between the two states is due to a difference in the energy alignment with neighboring Guanine bases.

ACKNOWLEDGMENTS

There have been many people who helped me realize my dream, but first I would like to thank my advisor Prof. Nongjian Tao for supporting me in the past 6 years. Dr. Tao brought me into the academics and taught lots of important skills. Whenever I encounter some problems in my projects, he always helps and encourages me to solve them. He is not only my mentor, but also my friend during my Ph.D. career.

I would like to thank my committee members Prof. Stuart Lindsay and Prof. Ian R. Gould for their discussions on the progresses of my projects during my technical reviews.

I would like to thank my collaborators Dr. Vladimiro Mujica, Dr. Mark A. Ratner, Dr. David N. Beratan, Dr. Nadrian C. Seeman, Dr. Ruojie Sha and Mr. Chaoren Liu for their excellent work.

I would like to thank my friends and colleagues in Tao Group including Dr. Joshua Hihath, Dr. Ismael Diez-Perez, Dr. Shaoyin Guo, Dr. Thomas Hines, Dr. Christopher Bruot, Dr. Julio L. Palma, Dr. Wei Wang, Dr. Xiaonan Shan, Dr. Xianwei Liu, Mr Yunze Yang, Ms Yueqi Li and many other group members. I really enjoy the six years with them in the family of BB center.

Finally, I would like to thank my parents who live thousands miles away and my wife who is just beside me for their endless love. It is my parents who encourage me to pursue my Ph.D. in U.S., and it is my wife who showed up and gave me a warm embrace when I was having my most difficult time during my Ph.D. study. I would like to express my gratitude to them.

TABLE OF CONTENTS

Page

LIST OF TABLES

LIST OF FIGURES

Figure Page

Figure Page

Figure Page

CHAPTER 1

INTRODUCTION TO MOLECULAR ELECTRONICS

1.1 Introduction

The investigations of electrical junctions, in which small molecular assemblies or single molecule act as conductors connecting conventional electrical components like metals, is named the field of molecular electronics[1]. The field was originated from a seminal paper published by Aviram and Ratner in which they proposed a single molecular rectifier[2]. The field of molecular electronics started to develop rapidly in the past two decades, mainly due to the advances in organic synthesis, the invention of scanning probe microscopes (SPM) and the developments of nanofabrication technique. A lot of experimental methods have been developed to study the electric properties of single molecule or small molecular assemblies. These include mercury drop junction[3-5], crossed-wire junction[6-8], conducting probe Atomic Force Microscopy (CP-AFM) junction[9-11], Scanning Tunneling Microscopy (STM) break junction[12-14], Mechanical-controlled break junction (MCBJ)[15-17] and several other experimental methods[18-21]. Combining solid state physics, organic chemistry, biophysics and engineering, the field of molecular electronics is seeking to understand and build up electronic devices on a molecular scale.

Exploring the charge transport mechanism is one of the basic tasks for researchers in the field of molecular electronics. By studying length dependence, temperature dependence, solvent dependence and current-voltage (I-V) characteristics of conductance value for different molecules with various chemical structures, people are trying to seek for and understand new charge transport mechanism. To date, it is widely accepted that non-resonant tunneling is responsible for charge transport for relatively shorter molecules[22-24], while for longer molecules, incoherent hopping transport starts to dominate[25-28]. Besides these, new charge transport mechanism is also being discovered in recent years. Understanding the charge transport mechanism is important for understanding the charge transport/transfer involved in many biological processes and electronics devices.

The next step after understanding the charge transport is to build up electronic devices based on molecules[29]. To date, many attempts have been made to build up single molecular devices with different functionalities such as diodes[30-33], transistors[34-36] and switches[37-44]. In addition to those devices mimicking the conventional silicone based electronic devices, researchers are also studying the interplay between the mechanical, thermoelectric, magnetic, optic properties and electric properties and developing single molecular sensors. Realizing these device applications is the ultimate goal for the field of molecular electronics.

This thesis will focus on the study of charge transport through DNA, an important biomolecule which stores our gene information. First, an introduction on the background and research methods of molecular electronics will be given. Then, by studying dsDNA molecules with different length and sequences, a new charge transport mechanism will be discussed. Then the following two sections will introduce DNA based single molecular electronic device. One section will introduce a DNA G-quadruplex based single molecular charge splitter. The other section will introduce an electrochemical gate-controlled single molecular switching behavior based on modified dsDNA. Finally, a summary of the three works will be made and comments on the limitations and implications of these works, and on future research directions will be given.

1.2 Charge transport theory

Understanding the charge transport mechanism is the most fundamental task in the field of molecular electronics. Like the field of mechanics including classic mechanics and quantum mechanics, the charge transport theory also falls into classic regime and quantum regime. This section will introduce the charge transport behaviors of molecular systems in the two main regimes.

1.2.1 Characteristic length

When an electron transports through a system, there are two important characteristic lengths involved. The first characteristic length is the momentum relaxation length L_m. It indicates the distance the electron can transfer in a system before colliding with impurities or defects. It can also be affected by the scattering of an electron with a phonon. The second characteristic length is the phase relaxation length L_ϕ. The phase information makes the electron behave like a wave, thus L_ϕ indicates the distance an electron can transfer before losing its coherence as a wave.

1.2.2 Ballistic regime ($L \ll L_m$ and L_ϕ) and Landauer formula

In this regime, the behavior of an electron is described as a wave in the quantum mechanics. Considering a simple 1-dimension (1D) case where a molecule is bridged in between two electrodes (Figure 1.1a), charge transport only occurs through the lowest unoccupied molecular orbital (LUMO) of the molecule represented by the barrier in between the Fermi levels of the two electrodes (Figure 1.1b).

The net current from the left electrode to the right electrode I_L given by:

$$I_L = e\int_0^\infty v_g(k)T(k)\, f\left[E(k),\mu_L\right]n(k)\,dk \text{, Equation 1.1}$$

Here v_g is the electron group velocity, T(k) is the transmission probability, f(E) is the Fermi-Dirac distribution function, μ_L is the chemical potential of the left electrode, n(k) is the density of states and $n(k)dk = 2\frac{1}{L}\frac{L}{2\pi}dk$. If one uses energy space instead of the k space, Equation 1.1 becomes:

$$\begin{aligned} I_L &= e\int_0^\infty v_g(k)T(k)\, f\left[E(k),\mu_L\right]\frac{2}{2\pi}\frac{1}{hv_g}dE \\ &= \frac{2e}{h}\int_0^\infty T(E)\, f\left[E,\mu_L\right]dE \end{aligned} \text{, Equation 1.2}$$

The net current I is given by:

$$I = I_L - I_R = \frac{2e}{h}\int_0^\infty T(E)\left[f(E,\mu_L) - f(E,\mu_R)\right]dE \text{, Equation 1.3}$$

Under a small bias voltage and k_BT is much smaller than the Fermi energy, one has:

$$f(E,\mu_L) - f(E,\mu_R) \approx -eV\frac{\partial f(E,\mu)}{\partial E} = e\delta(E-\mu) \text{, Equation 1.4}$$

Therefore, from Equation (1.3), the conductance of the molecule can be expressed as:

$$G = \frac{2e^2}{h} T\left(E_f\right), \text{ Equation 1.5}$$

Where E_f is the Fermi level of the two electrodes. Equation 1.5 is one of the most ubiquitous Equations in the field of molecular electronics and also named as the Landauer formula. $\frac{2e^2}{h} = 77.48\mu S$ is called conductance quantum and denoted by G_0. If there are multiple transport channels in a molecular system, Equation (1.5) becomes:

$$G = \frac{2e^2}{h} \sum_{i,j} T_{ij}\left(E_f\right), \text{ Equation 1.6}$$

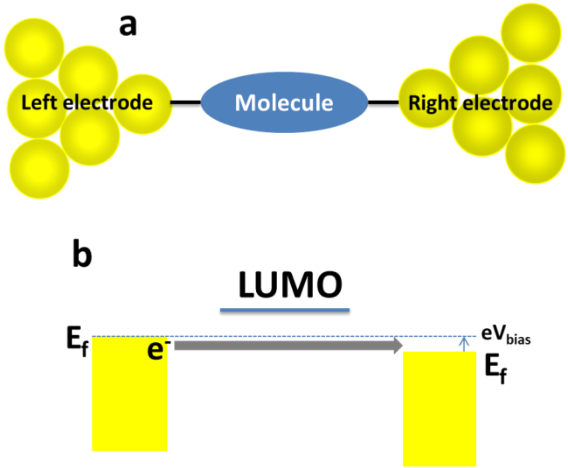

Figure 1.1: Charge transport through a molecule and Laudauer formula. (a) A molecule is bridged between two electrodes. (b) A small bias voltage V_{bias} is applied. Electron will go through the LUMO level of the molecule from the Fermi level of the left electrode to the Fermi level of the right electrode, thus generating current.

1.2.3 Non-Equilibrium Green's Function Formalism (NEGF) and superexchange model

To calculate the transmission probability in the Landauer formula, one can use the NEGF approach. The transmission probability can be related to the T operator where the molecular energy level acts as a barrier[45].

$$\sum_{i,j} T_{ij}\left(E\right) = 4\pi^2 \sum_{l,r} \left|T_{lr}\right|^2 \delta\left(E - E_l\right)\delta\left(E - E_r\right), \text{ Equation 1.7}$$

Where E_l and E_r is the energy level of left electrode and right electrode respectively. T_{lr} is the T operator, expressed by:

$$T_{lr} = V + VG\left(E\right)V \text{ , Equation 1.8}$$

The first term represents the direct transport from the left electrode to the right electrode, which can be neglected if the current transporting through the molecule dominates the total current. V is the coupling between the molecule and electrode. G(E) is the Green Function given by:

$$G\left(E\right) = \frac{1}{E - H + i\Gamma} \text{, Equation 1.9}$$

Where H is the Hamiltonian of the whole system and Γ^{-1} is the lifetime matrix of the molecule.

A more realistic case is that the two electrodes will be separated by N bridges states (N=1, 2, 3…N, Figure 2a). In this case, the superexchange model is found to be a good approximation to describe it. There are two assumptions in this model: 1. The energy of those N bridge states is far away from the Fermi level of the two electrodes. 2. The coupling only exists between the two neighboring states (tight-binding model) and it is much smaller than the energy difference between the bridge states and Fermi level. Thus in Equation (1.6), the molecular conduction can be expressed as:

$$G = \Gamma_1^L \Gamma_N^R \left| G_{1N}\left(E_f\right)\right|^2 \text{, Equation 1.10}$$

Where Γ_1^L is the coupling between the left electrode and first bridge state, Γ_N^R is the coupling between the right electrode and the N bridge state. The Green function is given by:

$$G_{1N}\left(E_f\right) = \frac{V_{1,2}}{\left(E_f - E_1 + \Sigma_1\left(E\right)\right)\left(E_f - E_N + \Sigma_N\left(E\right)\right)} \prod_{j=2}^{N-1} \frac{V_{j,j+1}}{E_f - E_j} \text{, Equation 1.11}$$

Where $\Sigma_1\left(E\right)$ and $\Sigma_N\left(E\right)$ are the associated shift in the energy level when the 1 or N state couples with the electrode respectively. E_j (j=1,2…N) is the energy of the j state and $V_{j,j+1}$ (j=1,2…N-1) is the coupling between the j state and j+1 state.

If one further neglects $\Sigma_1\left(E\right)$ and $\Sigma_N\left(E\right)$. E_j (j=1,2…N) and $V_{j,j+1}$ (j=1,2…N-1) are all the same constant denoted by E_B and V_B respectively. Equation (1.10) predicts that the molecular conductance G:

$$G \propto \left(\frac{V_B}{E_f - E_B}\right)^{2N} = \exp\left(-\frac{2}{a}\ln\left(\frac{E_f - E_B}{V_B}\right)\cdot Na\right) = e^{-\beta d} \text{, Equation 1.12}$$

Where a is the length of each repeating unit (one bridge state). Thus in the superexchange model, the molecular conductance has an exponential decay with respect to the molecular length d. This dependence has been observed in many molecule systems with different β, also named the decay constant (Figure 2b).

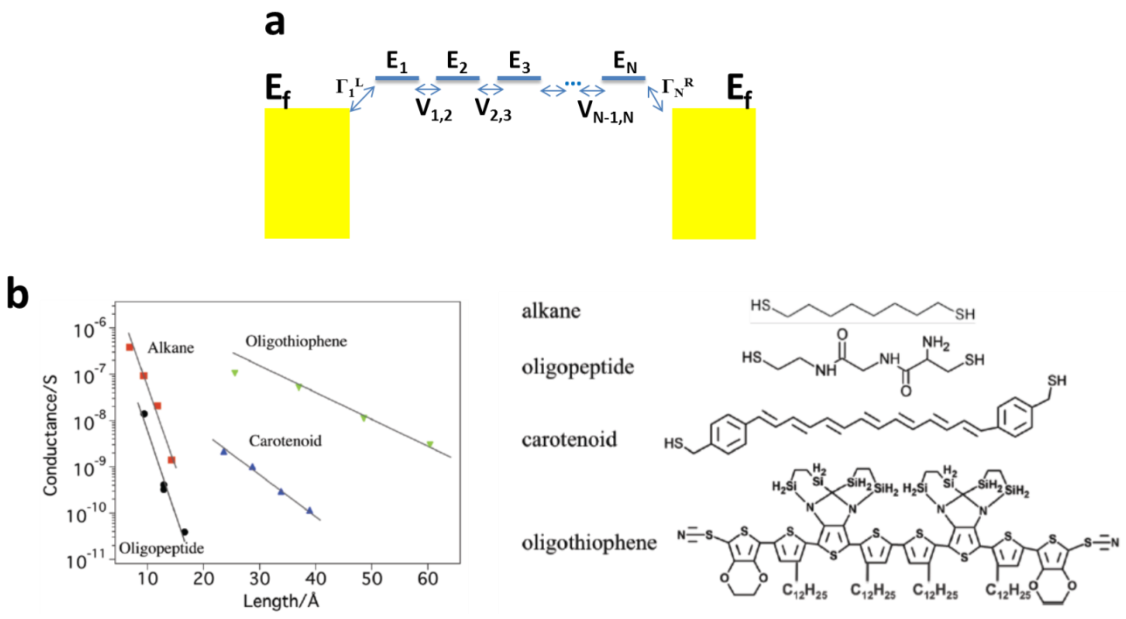

Figure 1.2: Coherent tunneling transport and superexchange model. (a) Superechange model where two electrodes are separated by N states. Only coupling between neighboring states is considered. (b) Length dependence of conductance for alkane[46], oligopeptide[47], carotenoid[48] and oligothiophene[49] system. All of them exhibit an exponential decay with different decay constant β, indicating tunneling transport mechanism.

1.2.4 Classic regime ($L >> L_m >> L_\phi$) and incoherent hopping transport.

When the number of bridge states N gets large, the time scale that an electron require to transport through the system gets longer. The electron can interact with the molecular vibration, thus losing its coherence and becoming totally incoherent[1]. Here I first consider a simple case with two scattering events. The transmission probability is denoted as T_1 and T_2. If one neglects any interference effect, i. e. the electron loses its phase information, then the total transmission probability T_{12} would be:

$$\frac{1}{T_{12}} = \frac{1}{T_1} + \frac{1}{T_2}\text{, Equation 1.13}$$

Thus the resistance value (inverse of the conductance) will be a linear combination of the two resistance values:

$$R_{12} = R_1 + R_2\text{, Equation 1.14}$$

When N scattering events exist, the resistance will have a linear dependence on the N (or the length).

$$R = R_c + \alpha N\text{, Equation 1.15}$$

Where R_c is the contact resistance and α is the unit resistance. This linear dependence has been observed for many different kinds of long molecular wire, e.g. oligophenyleneimine[26] (Figure 1.3a).

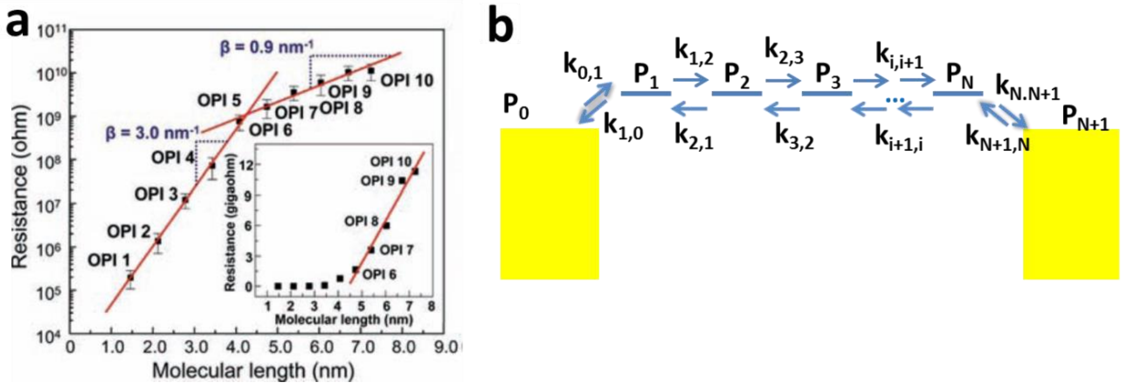

Figure 1.3: The resistance value of OPI molecular wire and sequential hopping transport mechanism. (a) The resistance of OPI molecular wire versus molecular length. A large β value was found for shorter OPI molecules and a small β value was found for longer OPI

molecules. Resistance of longer OPT molecules has a linear dependence on length[26]. Reprinted with permission from ref. [[26]]. (b) A sequential hopping model with N hopping sites, where the electron starts from left electrode, hops onto each of the individual hopping sites and reaches the right electrode.

1.2.5 Thermally activated incoherent hopping transport and steady-state flux method

One of the explanations for the linear dependence on length is called thermally activated incoherent hopping transport. The electron has to overcome activation energy to hop onto the next hopping site. This sequential hopping model was developed from the classic Donor-Bridge-Acceptor system and successfully explained the linear dependence of the resistance on molecular length[50]. Considering a N bridge sites system, where the charge transfer still only occurs in between two neighboring sites, one uses $k_{i,j}$ to represent the charge transfer rate from the i site to the j site (Figure 1.3b).0 state and N+1 state represent the left and right electrode respectively. P_i is the charge density on the i state. Under the assumption of steady-state, i.e. all the states reach an equilibrium, the master Equations of this system can be written as:

$$\begin{aligned}
&\frac{dP_1}{dt} = -\left(k_{1,0} + k_{1,2}\right)P_1 + k_{0,1}P_0 + k_{2,1}P_2 = 0 \\
&\frac{dP_2}{dt} = -\left(k_{2,1} + k_{2,3}\right)P_1 + k_{1,2}P_1 + k_{3,2}P_3 = 0 \\
&\ldots \qquad\qquad , \text{Equation 1.16} \\
&\frac{dP_{N-1}}{dt} = -\left(k_{N-1,N-2} + k_{N-1,N}\right)P_{N-1} + k_{N-2,N-1}P_{N-2} + k_{N,N-1}P_N = 0 \\
&\frac{dP_N}{dt} = -\left(k_{N,N-1} + k_{N,N+1}\right)P_N + k_{N-1,N}P_{N-1} = 0
\end{aligned}$$

Notice that $k_{N+1,N}$ is neglected here. The electron transfer rate of the whole system $k_{0,N+1}$ can be expressed as:

$$k_{0,N+1} = \frac{k_{N,N+1} P_N}{P_0}, \text{ Equation 1.17}$$

If all the charge transfer rates between the N bridge sites are the same and denoted as k, by solving the linear Equations (1.16) one has:

$$k_{0,N+1} = \frac{\left(k_{0,1} / k_{1,0}\right) k}{k / k_{N,N+1} + k / k_{1,0} + N - 1}, \text{ Equation 1.18}$$

Therefore, the total resistance of the system can be expressed:

$$R = \frac{k_{N,N+1}^{-1} + k_{1,0}^{-1}}{e^2 \rho\left(E_f\right)} e^{E_a / k_B T} + \frac{N-1}{e^2 \rho\left(E_f\right)} k^{-1} e^{E_a / k_B T}, \text{ Equation 1.19}$$

Where E_a is the activation originated from $e^{E_a / k_B T} = \frac{k_{1,0}}{k_{0,1}}$. $\rho(E_F)$ is the density of states at the Fermi level. This model explained the linear dependence of the total resistance value on the molecular length (or N). Meanwhile, it also gives a physical meaning to the activation energy E_a, indicating that the hopping process is temperature-dependent and the activation energy comes from the energy gap between the Fermi level of the electrodes and the energy level of the hopping sites.

1.3 Scanning Tunneling Microscopy (STM) break junction technique

Invented in 1981, the STM was used to image a conductive surface at the atomic level. The atomic resolution of STM is based on the quantum tunneling, where the tunneling current has an exponential dependence with respect to the distance, given by:

$$I = I_0 e^{-\beta L} \text{ , Equation 1.20}$$

Here I_0 depends on the electron density at the Fermi level and bias voltage. β is the decay constant of the medium. L is the distance. The STM system can precisely measure the current and distance information at the same time. If one applies this to the field of molecular electronics, then a question will come out: what will the current-distance trace look like if there is a molecule bridging between the two electrodes?

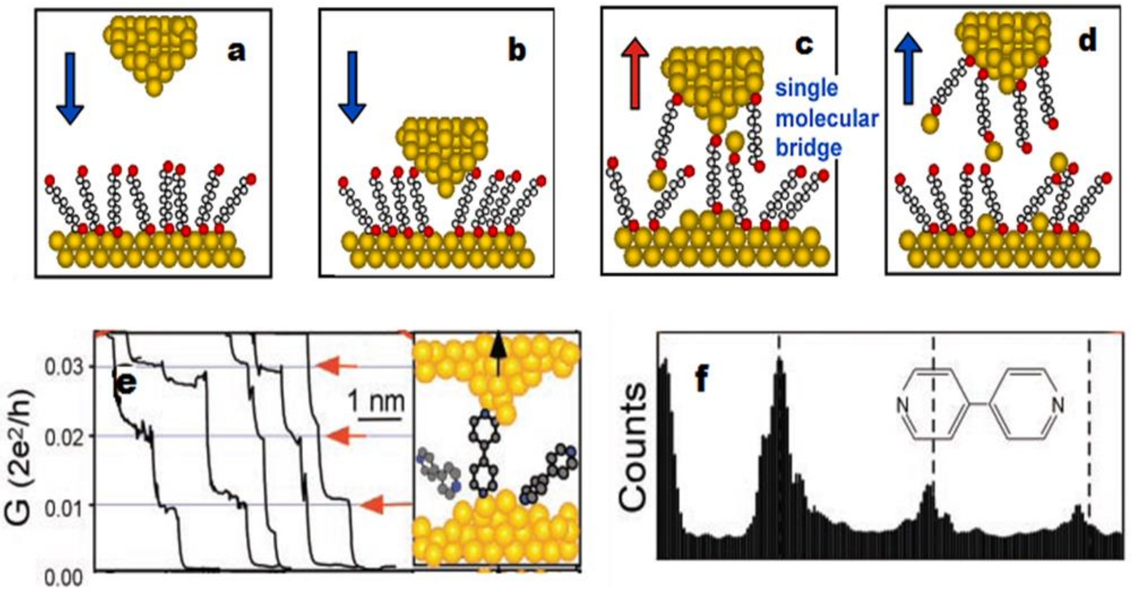

Figure 1.4: Scanning Tunneling Microscopy break junction (STM-BJ) technique. (a)-(d) Current-distance trace collections during the STM break junction technique. The Au surface was modified with octanedithiol molecule. Reprinted with permission from ref. [51]. (e) Representative current-distance trace when bipyridine molecule bridges in

between two Au electrodes[12]. Plateaus indicate the formation of a molecular junction. (f) Conductance histogram of bipyridine molecule[12], showing multiple peaks. The lowest peak is attributed to the conductance of a single molecule. The higher peaks are all integral multiple of the lowest conductance that are attributed to multiple molecules bridging between the two electrodes. Reprinted with permission from ref. [[12]].

In 2003, Tao and co-workers invented the STM break junction technique[12] and answered the question. In their approach the Au surface was immersed in the solution of the molecules (Figure 1.4a). Then the tip was repeatedly brought into and out of contact with a gold to create Au–Molecule–Au junctions (Figure 1.4b). During the pulling process (Figure 1.4c) the current was recorded versus distance, and a step in the current indicated the formation of a molecule bridged between the substrate and tip electrodes (Figure 1.4e). Further pulling will cause the breakdown of the molecular junction (Figure 1.4d) and the current will drop abruptly. Thousands of current–distance traces were collected and projected onto the conductance scale, from which a conductance histogram was constructed (Figure 1.4f). The conductance histogram sometimes will give multiple peaks. The conductance at the lowest peak is attributed to the conductance of a single molecule and the other peaks are due to multiple molecules bridging in-between.

In the past decade, the STM break junction technique has been widely used in the field of molecular electronics by several groups around the world. Since it relies on a statistical study of single molecule, it has been proved to be a robust and valuable technique in the field of molecular electronics. Moreover, due to the flexibility of the STM system, a lot of controllable physical parameters can be easily introduced into the experiments, e.g. voltage, light, force and gate voltage. Thus it provides a way to study the interplay between mechanical, thermoelectric, optic, chemical properties and the electric properties. Additionally, the STM can not only be performed in ultra-high vacuum but also in air and some other low-conductivity solvents. By coating the STM tip with Apeizon wax, the STM can be used in water, which is essentially the medium for all biological systems. These make STM break junction technique an excellent tool to carry out single molecule study.

1.4 Gate-controlled molecular junction

Two-terminal devices are most likely to be seen in the field of molecular electronics, but three-terminal devices are highly desired because traditional silicone-based electronics relies heavily on the three-terminal devices. Three main types of gating methods, the back gate[52, 53], electrochemical gate[14, 34, 38, 54] and chemical gate[55-58] have been developed to mimic the gate voltage in silicone-based electronics. Among them, electrochemical gate can be easily realized by inserting an extra reference electrode in a conductive environment (e.g. aqueous solution, ionic liquid). The large gate field created by the electrochemical potential allows electrochemists to control the energy levels on the molecules, thus affecting the energy alignment between the molecules and electrodes.

By using the electrochemical gate as the third terminal, researchers have developed single molecular transistor and single molecular switch. Diez-Perez et al.[34] reported the n-type field effect transistor behavior for coronene molecule. The molecular conductance can be enhanced up to two orders of magnitude higher when a negative gate voltage was applied. More interestingly, people observed different experimental results when studying redox molecules. For example, Osorio et al.[36] observed a peak at the redox potential when measuring the conductance of a bipyridinium molecule under different gate voltages (Figure 1.5a). The molecule will have the highest conductance when gate potential is at its redox potential, and this can be explained by the two-step hopping model[59]. However, Baghernejad et al.[38] observed some quite different results. In this work, they were able to show that the conductance of an anthraquinone-based molecule was switched between two states at different potential voltages (Figure 1.5b). They obtained a lower conductance when the gate voltage is above the redox potential and a higher conductance when the gate voltage is below the redox potential. An abrupt change was observed when the gate voltage is at the redox potential. The inconsistent here is possibly due to the reason that the two-step hopping model cannot be applied to a redox system which has two electrons transfer involved, since it requires too much energy to make two electrons hop onto one molecular orbital at the same time.

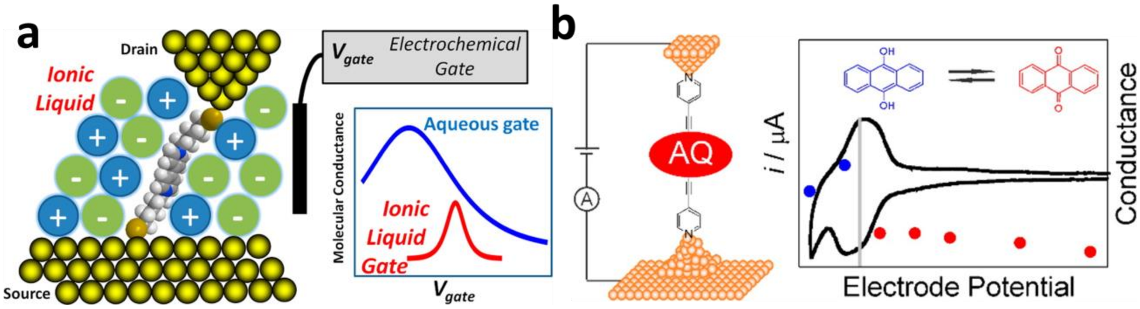

Figure 1.5: Electrochemical gate-controlled STM-BJ experiments on redox molecules. (a) Conductance of 1,1′-bis(6-(acetylthio)hexyl)-4,4′-bipyridinium hexafluorophosphate molecule under different gate voltage. The conductance reaches maximum at the redox potential. The difference between aqueous and ionic liquid is the difference in the so-called gating efficiency[36]. Reprinted with permission from ref. [36]. (b) Conductance of an

anthraquinone based molecule under different gate voltage. The conductance changes abruptly at the redox potential. Black line is the cyclic voltammogram. Circular dots are the conductance value data points. Reprinted with permission ref. [[38]].

1.5 Charge transport/transfer in DNA

Charge transport/transfer in DNA has been extensively studied by photochemical methods and electrochemical methods. It was widely accepted that charge transport through short DNA is coherent tunneling while for long DNA, it is sequential hopping. This behave is similar to some other organic conjugated molecules. The transition from tunneling to hopping has been observed by many groups using various methods. Giese et al.[60] reported the transition from tunneling to hopping at the distance of 3 base pairs for AT base pair. In this work they used the photolysis of 4'-acylated nucleotide to generate a radical cation. The radical cation propagated through the bridge consisting of AT base pairs. Finally they measured the oxidized damaged product with respect to the length of the AT base pairs to indicate the charge transfer efficiency.

One of the most widely used photochemical method is developed by Prof. Federick D. Lewis and Prof. Michael R. Wasielewski in 1997[61, 62]. In this approach they modified the two ends of DNA with a hole donor and a hole acceptor group respectively while the double helical structure still remains (Figure 1.6). A time-resolved fluorescence spectroscopy was used to monitor the intensity at 575 nm and 525 nm to characterize the donor and acceptor species with the hole respectively. A charge transfer rate constant can be extracted by plotting the intensity vs. time. In a later work, they were also able to observe a transition from tunneling to hopping transport at 3 AT base pairs distance[63], consistent with Giese et al.'s work[60].

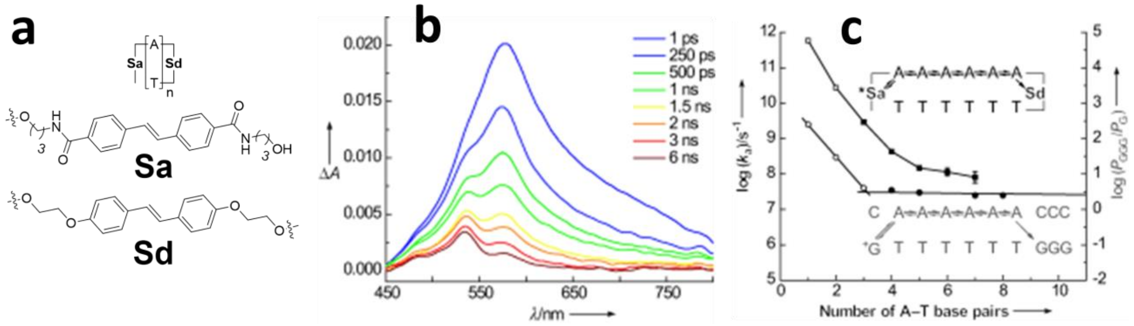

Figure 1.6: Photochemistry study on DNA charge transport. (a) Structures of DNA with hole donor and hole acceptor. (b) Transition absorption spectroscopy recorded from 1ps to 6 ns. The peak around 575 nm is due to the Sa excited state with a hole. The peak around 525 nm is due to the Sd with a hole. By plotting the intensity ratio A_{575nm}/A_{525nm} vs. time, one can extract the charge transfer rate constant. (c) Charge transfer rate constant is plotted vs. the number of n in Figure 1.6a. The square represents the data in Lewis et al.'s work[63] and the circle represents the data in Giese et al.'s work[60]. Reprinted with permission from ref. [[63]].

Another major platform that has been effectively used is the electrochemical methods developed by Prof. Jacqueline K. Barton[64, 65]. Typically a thiol-modified dsDNA will be immobilized onto a Au surface. A redox group (anthraquinone, methylene blue or nile blue) will be modified into the DNA sequence and intercalate in between the base pairs (Figure 1.7). The redox group will be spaced by the DNA sequence from the Au electrode. Thus by measuring the cyclic voltammograms under different sweeping rate and applying Laviron analysis[66], one can obtain the charge transfer rate constant.

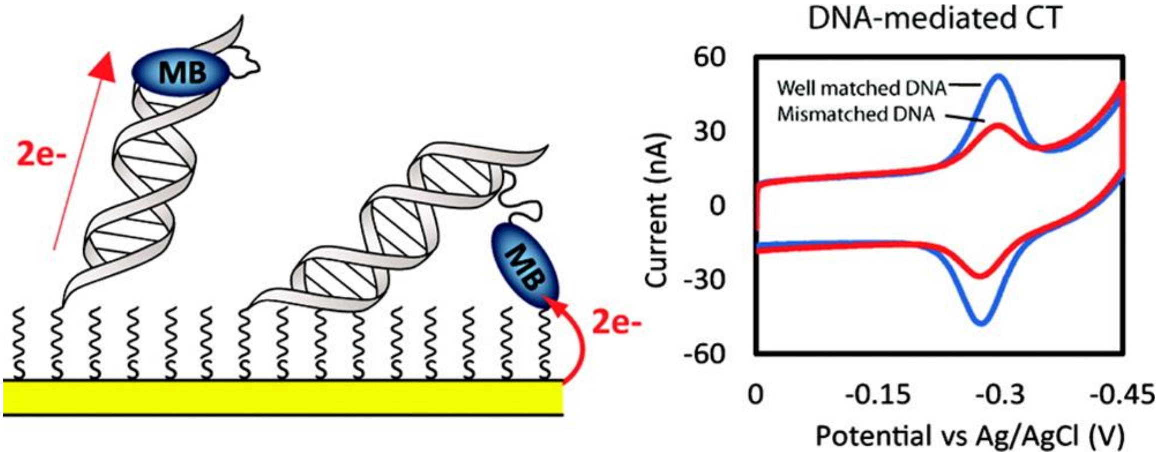

Figure 1.7: Electrochemistry study of DNA charge transport via cyclic voltammograms. DNA was immobilized onto the Au surface via thiol groups. The methylene blue (MB) was intercalated into the dsDNA. By measuring the peak separation (in mV) in the cathodic and anodic peak of the cyclic voltammograms under different sweeping rates and applying the Laviron analysis[66], one can obtain the charge transfer rate constant. Reprinted with permission from ref. [[67]].

It is worth to mention that both photochemical and electrochemical methods measure the charge transfer rate constant, but the results have orders of magnitude difference. This is probably due to the reason that the charge transfer rate constant was measured under excited state of DNA in photochemical methods, but ground state for electrochemical methods[65].

Chemists prefer to use chemical groups and characterization technique to study the charge transfer/transport in DNA, but physicists and engineers want to use a more direct way. That is direct measurements of charge transport by bridging two electrodes with DNA molecules. In this method, a bias voltage will be applied and the current will be recorded to obtain the conductance value (or resistance value) of the DNA molecules. For example, Porath et al. bridged the DNA molecules in between the Au surface and a Au nanoparticle, and then utilized conductive AFM to directly obtained the current-voltage (I-V) characteristic[68]. Xu et al.[69] also reported STM break junction measurements on dsDNA modified with thiol linker. In this work, they found out that charge transport through GC base pair is sequential hopping while for AT base pair (up to 4 base pairs), it is coherent tunneling (Figure 1.8).

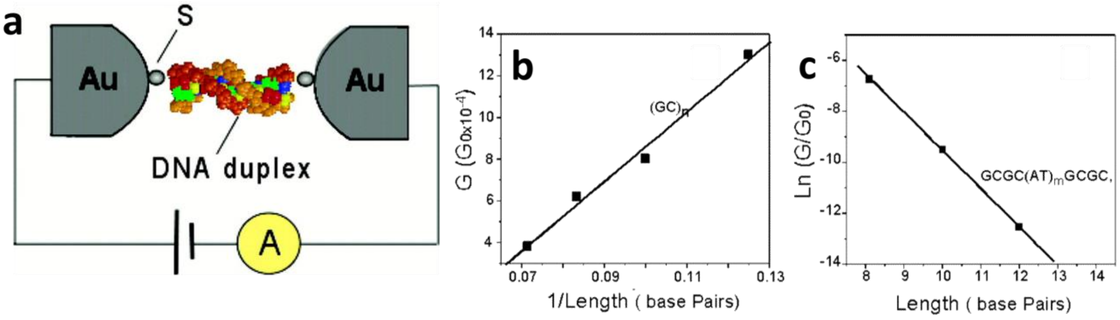

Figure 1.8: STM-BJ study on charge transport through DNA. (a) STM break junction measurements of dsDNA with thiol terminated group. The dsDNA bridges between two Au electrodes. A bias voltage was applied and the current was recorded to obtain the conductance. (b) Conductance of $(GC)_n$ dsDNA vs 1/length. The linear trend indicates a sequential hopping transport mechanism. (c) Natural logarithm of $GCGC(AT)_mGCGC$ dsDNA conductance vs length (total number of base pairs). The exponential dependence of the conductance on length indicates a coherent tunneling transport mechanism. Reprinted with permission from ref. [[69]].

Besides these experimental methods, charge transport through DNA has also been studied by theoretical models[70-72] and computational simulations[73-75]. Jortner et al.[71]

proposed that charge transport through GC base pairs is mainly through hopping between neighboring Guanine or Adenine bases (Figure 1.9a). Renaud et al.[73] found that the charge transport is coherent tunneling for short AT base pairs (less than 3), but incoherent hopping for longer AT base pairs (Figure 1.9b). Their calculations results successfully explained the photochemical results by Lewis et al.[63] Combining these experimental and theoretical results, it is reasonable to conclude that charge transport through shorter DNA sequences with AT base pairs is coherent tunneling while for longer DNA sequences with AT base pairs and GC base pairs, the transport will be hopping dominated.

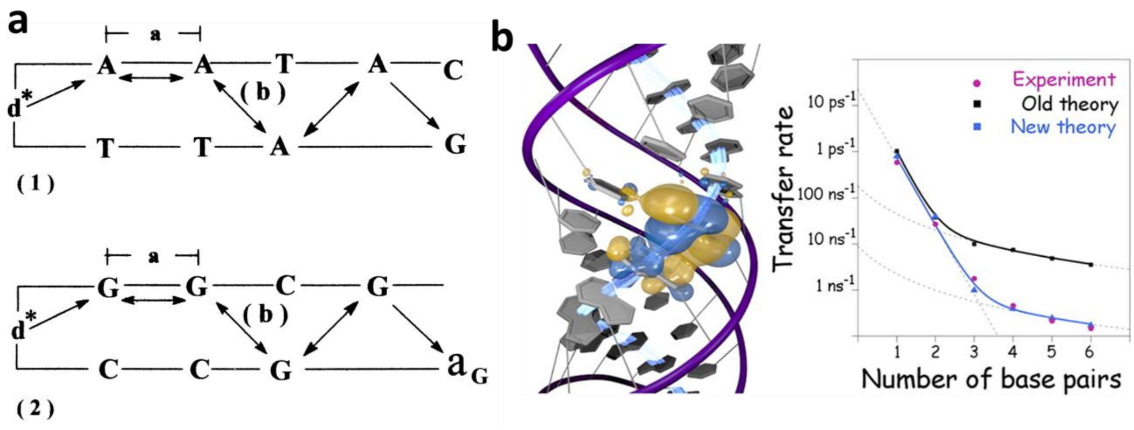

Figure 1.9: Theory on charge transport through DNA. (a) It is predicted that DNA charge transport is hopping through neighboring Guanine or Adenine bases. Reprinted with permission from ref[[71]]. (b) According to the computational simulations, the charge transport for AT base pairs exhibits a transition from tunneling regime to hopping regime, consistent with experimental results[63]. Reprinted with permission from re[[73]].

CHAPTER 2

INTERMEDIATE TUNNELING-HOPPING REGIME IN DNA CHARGE TRANSPORT

Adapted with permission from Limin Xiang, Julio L. Palma, Christopher Bruot, Vladimiro Mujica, Mark A. Ratner & Nongjian Tao*. “Intermediate tunneling–hopping regime in DNA charge transport” *Nature Chem.* **2015,** *7,* 221-226. Copyright 2015 Nature Publish Group.

2.1 Introduction

Charge transport and charge transfer processes in double helical DNA have received many interests over the past two decades since it is relevant to the oxidative damage of DNA, which is critical to the viability of all living organisms[76, 77]. The observation of long-range charge transport in DNA[78, 79] and advances in construction of DNA nanostructures[80] have stimulated the interest in exploring DNA as building blocks for nano devices applications. Understanding the charge transport through DNA is both important to the understanding of DNA oxidation in biological system and building up electronic devices based on DNA.

Charge transport in DNA have been studied by many experimental methods[60, 61, 64, 69, 78, 81-84], theoretical models[70-72] and computer simulations[72, 73, 85, 86]. It is widely accepted that charge transport through DNA is coherent tunneling for shorter DNA molecules, but sequential hopping for longer DNA molecules[87]. In the tunneling regime, the resistance will increase exponentially with respect to the length[70], while in the hopping regime, resistance value has a linear dependence on length[71]. This linear trend is because that the hole starts to treat each purine base (Adenine or Guanine) as a hopping site. However, Renaud et al. showed that strong electronic coupling between the π-electrons of neighboring base pairs can lead to delocalization of the holes among several base pairs in dsDNA[18], potentially can induce coherence in the transport.

In this chapter, a new charge transport mechanism was found for dsDNA. I found the evidence of an intermediate regime where coherent and incoherent processes coexist by measuring the resistance in DNA bridged between two electrodes with respect to the DNA sequence and length. The resistance of DNA generally increases linearly with length, indicating an incoherent hopping. But for DNA sequences with stacked guanine-cytosine base pairs, a periodic oscillation was found to superimpose on the linear dependence, indicating a partial coherent transport. The result is further supported by the finding of strong delocalization of the highest occupied molecular orbitals (HOMOs) of GC from theoretical simulation and modeled based on Büttiker's theory of coherent correction on hopping transport.

2.2 Experimental methods

All the DNA samples were purchased from Bio-Synthesis Inc. (HPLC purified with certificate of analysis via Mass Spectroscopy). $Na_2HPO_4 \cdot 2H_2O$ (for HPLC, ≥98.5%) and NaH_2PO_4 (for HPLC, ≥99.0%) were purchased from Fluka, and $Mg(OAc)_2$ (ACS reagent, 99.5%-102%) was purchased from Sigma-Aldrich. All the reagents were used without further purification. Multigene Mini Thermal Cycler (Model: TC-050-18) was used to anneal DNA solution samples. Phosphate buffer (pH = 7.0) was prepared by dissolving $Na_2HPO_4 \cdot 2H_2O$ (198 mg), NaH_2PO_4 (133 mg) and $Mg(OAc)_2$ (47 mg) in 10 mL D.I. water. dsDNA solution was prepared by mixing 90 µL PBS buffer with 10 µL of 100 µM ssDNA solution (dissolved in deionized water) and annealed by varying temperature from 80 ℃ to 8 ℃ at the rate of 4 min/℃, and then kept at 4 ℃. The annealing process for longer strand DNA ($n \geq 6$) is: 5 min at 95 °C, cooling from 90 ℃ to 76 ℃ at the rate of 5 min/℃, further cooling from 76 ℃ to 26 ℃ at the rate of 15 min/℃, holding at 25 ℃ for 30 mins, then kept at 4 ℃. This step-wise process helped prevent the formation of ssDNA hairpin structures. See further details in Figure 2.7 and Figure 2.8. All the other experiment setups can be found in previous reports[69].

I carried out the measurements in a 2.5 µM dsDNA solution. 50 µL phosphate buffer was added into the sample holder. A small bias voltage (10 mV to 30 mV) was applied between the gold tip and the gold substrate in a STM break junction setup. Exponential decay in the current-distance traces was observed in the phosphate buffer in the absence of DNA molecules (see the black traces in Figure 2.1b). However, after adding 5-µM dsDNA solution steps appear in the current-distance traces (see the red traces in Figure 2.1b). I collected a large number of current-distance traces (~5000) in each experiment, and constructed conductance histograms with an algorithm described previously[48]. The algorithm counted only the traces showing counts exceeding a preset threshold in the histograms (Figure 2.1c). For each sequence, the measurement was repeated 3-4 times on different days. In addition to pure phosphate buffer, measurement in ssDNA solution was also carried out as a further control experiment. The absence of steps in the current-distance traces in ssDNA indicates no hairpin formation in the samples.

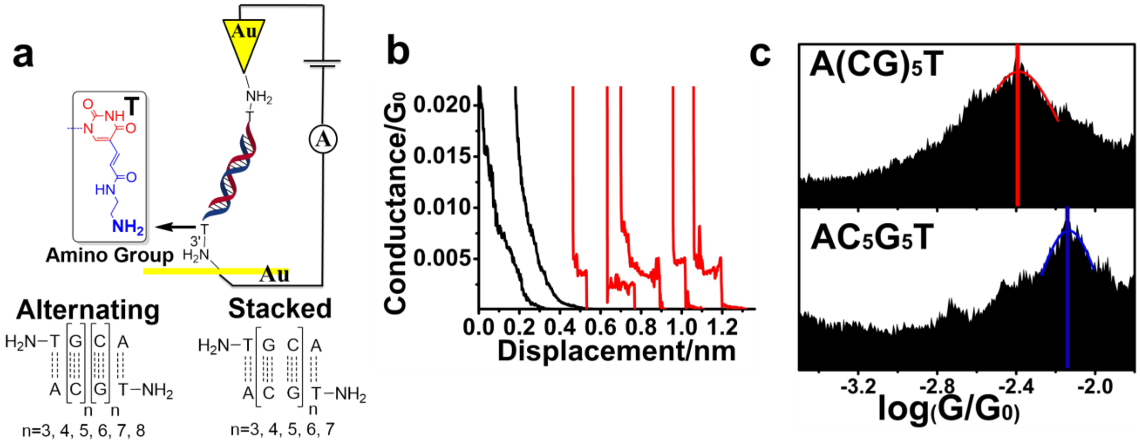

Figure 2.1: Conductance measurements of dsDNA using STM-BJ. (a) The DNA sequences measured in this work. Amine modified T base was used as the terminated group. Two series of sequences: alternating and stacked sequences were measured. (b) Individual current-distance traces of A(CG)$_5$T (red lines which have plateau features) in aqeuous solution, and control experimets performed in the absence of DNA molecules (black lines with exponential decay). (c) Conductance histograms of A(CG)$_5$T and AC$_5$G$_5$T. The red and blue lines indicate the peak position, which is attributed to the conductance of single DNA duplex.

Quantum chemical calculations were performed to obtain orbital energies at equilibrium (zero bias) of the dsDNA sequences at the INDO/S level with a minimal basis set, which has been shown to be a reliable method for the description of electronic coupling between base pairs of DNA[49,50]. Electronic coupling calculations were performed under the two-state model[51] framework and the systems were set at the conformation of canonical B-DNA and only the base pairs were considered while the backbone was removed. Two neighboring stacked base pairs and approximated the donor and acceptor states by the HOMO orbitals of each Watson-Crick base pair in the present of the neighboring base pair and Hamiltonian in the basis of atomic orbitals were used to obtain the coupling coefficient.

2.3 The linear trend for alternating sequences

I first studied the DNA sequence 5'-A$(CG)_n$T-3' with n = 3, 4, 5, 6 and 7. Note that all the DNA sequences are self-complementary, so one dsDNA will consist of two ssDNA sequences. I carried out the STM-BJ experiments and measure their resistance values with respect to the number of n (or the length). A linear trend was found for this series of sequences (Figure 2.1a), consistent with Xu et al.'s work[69]. This is because that the charge transport mechanism is mainly sequential hopping[25, 88]. In this model, the hole will treat each of the Guanine base as one hopping site and hop through the whole sequence. This is further supported by the molecular orbital spatial distribution calculations (Figure 2.1b). The calculated HOMO of each Guanine will mainly localized on one Guanine, thus the hole has to hop onto each of the Guanine before it reaches the right electrode.

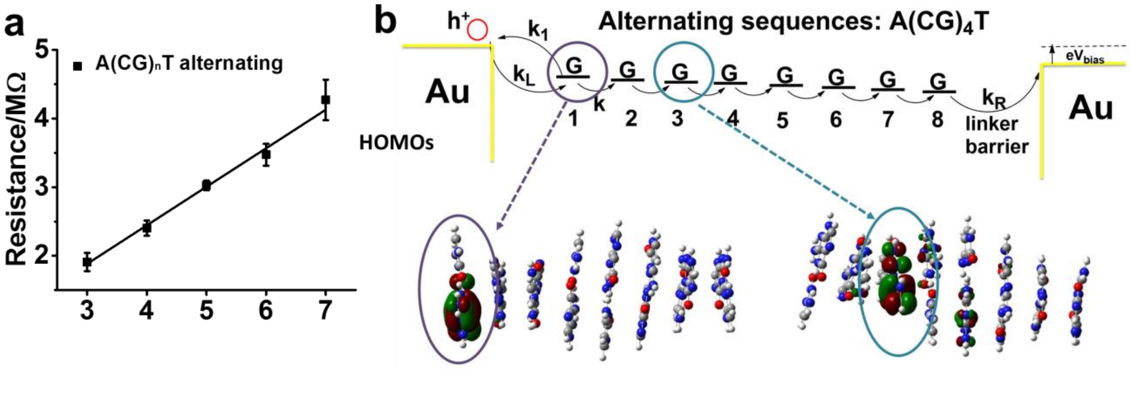

Figure 2.2: The linear trend for the alternating sequences. (a) The resistance value of alternating sequences has a linear dependence on the number of n (or length). (b) The sequential hopping transport mechanism is responsible for the transport. The hole starts

from left electrode, hops onto each of the Guanine base and then reaches the right electrode. The HOMO level of each Guanine will mainly localize on each Guanine.

In the hopping transport mechanism, the resistance of the DNA molecule is proportional to the inverse of the hole transport rate, k_{ET}, given by[89] $R=\left[e^2 k_{ET}\rho\left(E_F\right)\right]^{-1}$, where e is the elementary charge and $\rho(E_f)$ is the density of states at the Fermi level. According to a sequential hopping model based on the steady-state flux method, the resistance is described by[50, 89],

$$R=\frac{k_L^{-1}+k_R^{-1}}{e^2\rho\left(E_f\right)}e^{E_a/k_BT}+\frac{N-1}{e^2\rho\left(E_f\right)}k^{-1}e^{E_a/k_BT} \text{, Equation 2.1}$$

where k_L, k_R and k are the hole transfer rate constants from left electrode to the first G of the DNA, from the last G of the DNA to the right electrode and between adjacent hopping sites, respectively, E_a is the activation energy, k_B is the Boltzmann constant, and T is temperature. The first term of Equation 2.1 represents the electrode-molecule contact resistance, and the second term in Equation 2.1 describes the efficiency of hole hopping along DNA. By fitting the length dependence of resistance with Equation 2.1, the slopes for the alternating is 0.56±0.05 MΩ.

2.4 Trend for stacked sequences: the smaller slope

I first examine the structural difference by looking at the 3D structures of alternating sequence and stacked sequence with n=4. Figure 2.3 clearly shows the difference in the stacking of neighboring G bases in the two DNA sequences. In the alternating sequence, the nearest neighbor Gs do not overlap with each other, which is in contrast to the stacked sequence, where the nearest neighbor Gs stack on top of each other, leading to a stronger electronic coupling between the adjacent G bases[90, 91]. This expectation is further confirmed by electronic coupling calculations based on INDO/S Hamiltonian. The coupling strength between neighboring Gs are 0.10 eV and 0.14 eV for alternating sequences and stacking sequences, respectively. The strong electronic coupling in the stacked G DNA indicates that holes may delocalize over several neighboring G bases, thus making the HOMO level higher[92].

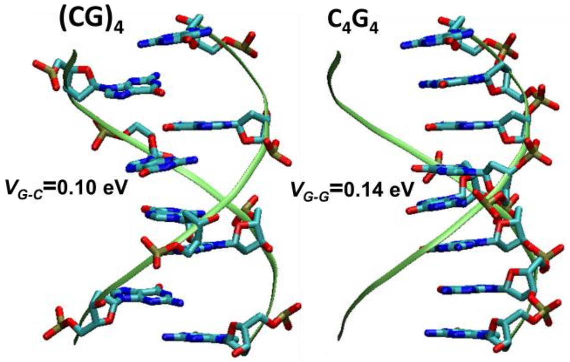

Figure 2.3: The 3D structure view for alternating sequence and stacked sequence, showing a strong stacking interaction between neighboring Guanines in stacked sequence.

The stronger coupling strength in stacked sequence is supported by the experimental results. Figure 2.4a shows the resistance value of stacked sequences comparing to alternating sequences. The stacked and alternating sequences are different by the sequence order, but their charge transport properties are significantly different. First, the stacked G sequence is less resistive than that of the corresponding alternating sequence with the same length. This is consistent with calculations of the higher HOMO level for stacked sequences, which makes the resistance value lower (Figure 2.4b and 2.4c). The finding is also consistent with results reported in literatures. For example, Saito et al.[93] reported that GGG moiety was easier to oxidize than G based on a photoinduced DNA cleavage measurement. Ratner et al.[94] reported that the ionization potentials of GG and GGG were lower than G by 0.5 and 0.7 eV, respectively. Second, the overall resistance of stacked and alternating G sequences increases linearly with length, which is due to hopping transport[25, 88], but the slope of stacked G DNA is smaller than that of the alternating sequences. In other words, the resistance of the stacked sequences depends on the length more weakly. Again, this is consistent with the calculations of higher coupling strength for neighboring Guanines in stacked sequences.

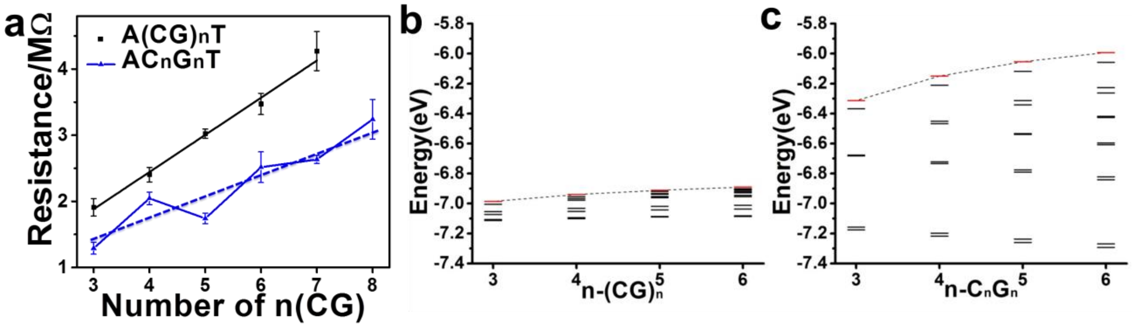

Figure 2.4: Comparison of resistance value and HOMO levels for alternating and stacked sequences. (a) The resistance value for alternating sequences (black) and stacked sequences (blue). The periodic oscillation effect will be discussed later. (b) HOMO levels for alternating sequences with n = 3, 4, 5 and 6. (c) HOMO levels for stacked sequences with n=3, 4, 5 and 6. Stacked sequences have a higher HOMO level than that of alternating sequences.

2.5 Trend for stacked sequences: the oscillation behavior

The last striking observation in Figure 2.4a is the oscillation of resistance superimposed on the linear trend of resistance for the stacked G DNA sequences. Similar behaviors in the length dependence of resistance have been observed in coherent transport, in some systems such as 1D atomic wires[95], and predicted for 1D conjugated molecular systems involving strong overlap of π-electrons[96]. By assuming coherent resonant tunneling, the periodic oscillation has also been predicted for DNA molecules[85]. However, in those coherent transport systems, the overall resistance varies little with the length, which is in contrast to the observation here in stacked G DNA sequences. Another observation that is not predicted by the coherent transport model is that the oscillation effect diminishes with respect to the molecular length.

The origin of the resistance oscillation in 1D metallic wires and conjugated molecular systems is the delocalization of electrons in the systems. Those electrons are reflected by the boundaries and form standing waves causing interference[95]. The molecular orbital spatial distribution calculations for stacked G sequences were performed and the occupied molecular orbitals are delocalized over 2-3 base pairs, and their energy levels are close to the Fermi level of the electrodes (Figure 2.5a). In another word, in contrast to the alternating sequences, where the hopping site is one G base, the hopping site in the stacked G sequences consists of 2-3 base pairs (Figure 2.5a). This delocalization domain has also been reported by Barton et al.[97] for charge transfer through stacked A domains, and by Majima et al.[83] for charge transfer in DNA sequences containing stacked GAG bases. The former reported a periodicity in the charger transfer yield vs. length, and the latter reported an oscillation effect depending on the location of the delocalization region (stacked GAG) in the sequence. The delocalization of holes over several bases suggests that the coherency of holes does not become fully washed out over a short distance, and the sequential hopping model must be corrected to include this coherent part. The conclusion is also consistent with the theory by Renaud et al.[73] for

Poly(A)-Poly(T) DNA hairpins, and the analysis by Venkatramani et. al[98] for peptide nucleic acids (PNA).

The partially coherent and incoherent charge transport has been previously studied in semiconductor devices. In 1988, Büttiker[99] developed a theory which includes a coherent correction to the completely incoherent charge transport in 1D systems. Here I apply the theory to the charge transport in stacked G DNA sequences (Figure 2.5a), and found that the total resistance of the DNA can be described as,

$$R_{tot} = R_0 + \frac{h}{e^2} \frac{N-1}{1-2e^{-B(N-1)}\cos\left[C\left(N-1\right)\right]} T^{-1} \text{, Equation 2.2}$$

where R_0, is the contact resistance (including also the hopping rate between the two stacked G regions in the middle of the molecule), and the second term describes hopping transport with a coherent correction. In Equation 2.2, T is the transmission probability from one G to the adjacent G, $B = -\frac{w_0}{v\tau_i}$, is the decay of coherence over distance, i.e. the coherence length, where v is the velocity of the carrier, τ_i is the inelastic scattering time, and w_0 = 0.33 nm is the base pair distance in B-form DNA, $C = \frac{2\sqrt{2mE}}{\hbar} w_0$, where m and E are the mass and energy of the holes. Note that Equation 2.2 is similar to Equation 2.1 except for the denominator in the second term of Equation 2.2, which is the correction of the coherent transport[99]. The cosine function leads to the periodic oscillation in the length dependence of the resistance and the exponential decay function determines that the oscillation will diminish as the length increases.

Figure 2.5b shows the fit of the experimental data (blue) to the model (red) given by Equation 2.2. The contact resistance R_0 was set to be 0.76 MΩ, which was obtained by extrapolating the plot of the resistance in Figure 2.2a to zero length. Several parameters can be obtained from the fitting. First, the resistance per GC base pair is 0.31±0.01 MΩ. The slope for the alternating is 0.56±0.05 MΩ, which gives a ratio of 1.8 between the two slopes. According to Marcus theory, the charge transfer rate is proportional to the square of the coupling. The square of the ratio of the electronic coupling strengths between the stacked and alternating sequences is about $1.4^2 = 1.96$, which is consistent with the observed ratio of the slopes. Second, the energy of the holes calculated from the fitting parameter C is 0.29±0.02 eV. Finally, $v\tau_i$ is 0.56±0.06 nm, which gives a coherence length of ~2 base pairs, consistent with other experimental work[60, 63] and theoretical calculations[85, 100] for charge transport through stacked A sequences. The experimental data can be accurately described with the Büttiker's theory with reasonable physical parameters, which further supports the conclusion of partial coherent component in the hopping transport mechanism in the stacked G sequences.

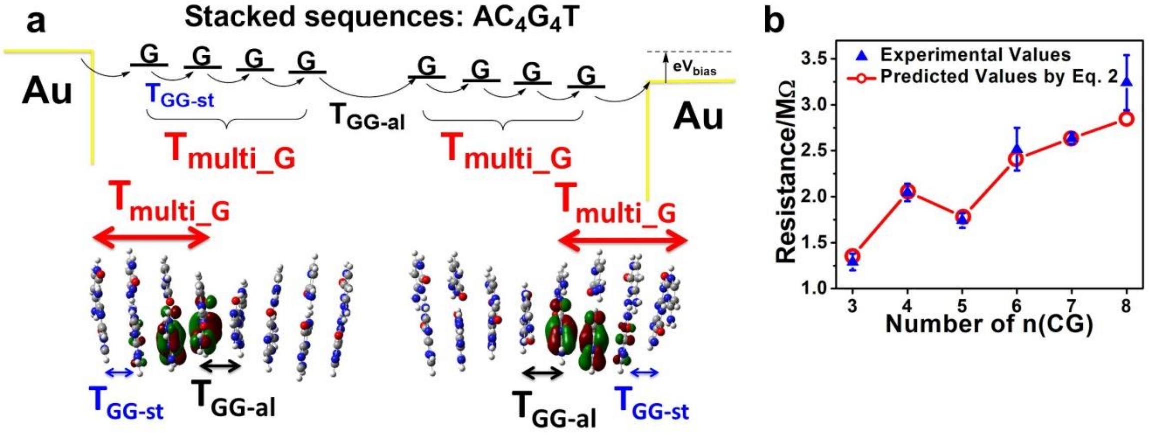

Figure 2.5: Intermediate tunneling-hopping charge transport in stacked DNA sequences. (a) Top: Schematic illustration of intermediate tunneling-hopping transport mechanism in stacked sequences, where T_{multi_G} is the transmission probability via the stacked G-segments of the DNA including the coherent correction, $T_{GG\text{-}st}$ is the transmission probability between two adjacent stacked Guanines and $T_{GG\text{-}al}$ is the transmission probability between the two stacked G-segments. $T_{GG\text{-}st}$ and $T_{GG\text{-}al}$ have incoherent components only. Bottom: HOMO levels of C_4G_4 show the delocalization of the orbitals, in contrast to Figure 2.2, indicating that the coherent tunneling transport coexists with incoherent hopping transport through the stacked G-segments. Note: there is no delocalization between the fourth G and fifth G in the middle, like the Guanines in alternating sequences. (b) Experimental resistance (blue triangle) and prediction of the Büttiker theory (see Equation 2.2) of partial coherent charge transport (red circle on red line), indicating that the oscillation is caused by the coherent processes when holes transport through stacked G-segments. Error bars were the standard deviations calculated from 3-4 sets of experiments for each individual DNA sequence.

2.6 Terminate groups for DNA sequences

Finally I also compared out alternating sequences results with those DNA sequences reported by Xu et al. before[69]. Xu et al.'s DNA sequences have a thiol terminated group that is connected to the sugar ring while the DNA sequences have the amine terminated group that is connected to the T base (Figure 2.6a). The data show the contact via the DNA T base in this present work is 3-6 times more conductive than the sugar contact in Xu et al.'s work (Figure 2.6b). This observation supports that charge transport in DNA is mainly through the π-stacking pathway of the base pairs but not the sugar backbone[101].

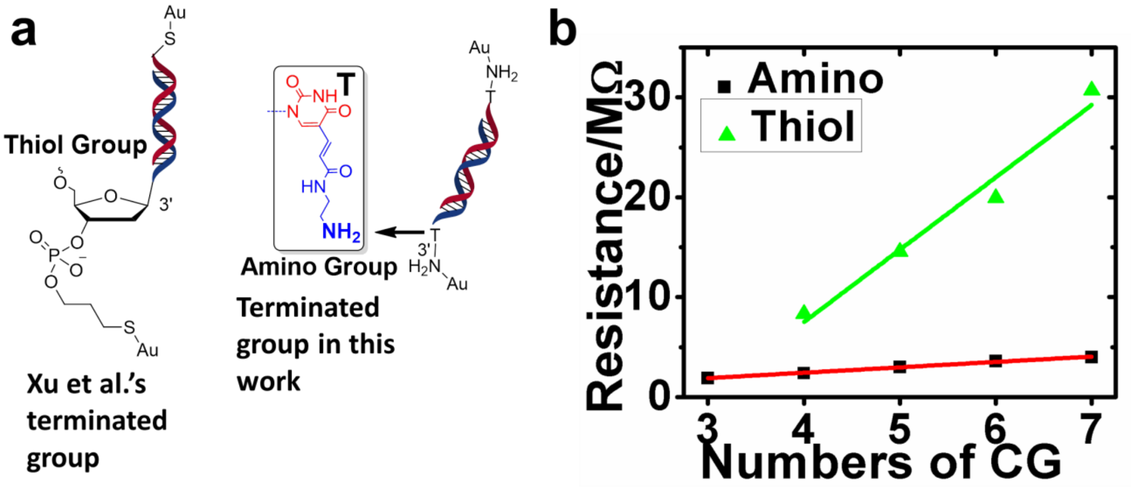

Figure 2.6: DNA sequences with thiol and amine terminated group. (a) Structures of Xu et al's thiol terminated group and the amine terminated group in this present work. Thiol group was connected to the sugar ring while amine group was connected to the T base. (b) resistance value of Xu et al's data (green) and the data in this present work (black) for alternating GC sequences. The DNA sequences in this present work is much more conductive than the DNA sequences in Xu et al.'s work.

2.7 Other supporting data

To check the formation of the dsDNA, I performed nondenaturing polyacrylamide gel electrophoresis on all the dsDNA sequences I studied. The electrophoretic measurement was performed at 200 V, and 10 ℃ for 3 hrs using 50 pmol of each sample and with 10% nondenaturing PAGE gels in 1×TAE Mg^{2+} buffer. The gels were subsequently stained with ethidium bromide (EB) and scanned in a Biorad Gel Doc XR+ system for sample visualization. DNA samples include 5'-A$(CG)_n$T-3' (n=3,4,5,6,7) and

5’-AC$_n$G$_n$T-3’ (n=3,4,5,6,7 and 8) sequences. These samples were annealed in two different ways. The first one involved ramping the temperature from 80 ℃ to 8 ℃ within 4 hours (kept at a certain Celsius degree for 3 minutes and 20 seconds, then decrease the temperature by one Celsius degree), and then kept at 4 ℃. The electrophoresis data show the formation of hairpin structures for some of the longer DNA molecules (Figure 2.7). The second annealing involves stepwise temperature changes: 1) annealing at 95 ℃ for 5 min; 2) cooling from 90 ℃ to 76 ℃ at the rate of 1 ℃ per 5 minutes; 3) further cooling from 75 ℃ to 26 ℃ at the rate of 1 ℃ per 15 minutes; 4) then holding the temperature at 25 ℃ for 30 mins, and finally 5) kept the sample at 4 ℃. This sample annealing process did not produce any hairpin structures (Figure 2.8).

The melting temperature can be accurately predicted on IDT (integrated DNA technologies) website (http://www.idtdna.com/analyzer/Applications/OligoAnalyzer/). The sequence with the lowest melting temperature is AC$_3$G$_3$T sequence, with a melting temperature of 50.9 ± 1.4 ^{o}C under the buffer condition, much higher than the room temperature (22 ^{o}C). Therefore the dsDNA sequences are very stable in B-form and ‘breathing’ or opening/closing of the strands won’t have any effect on the experimental results.

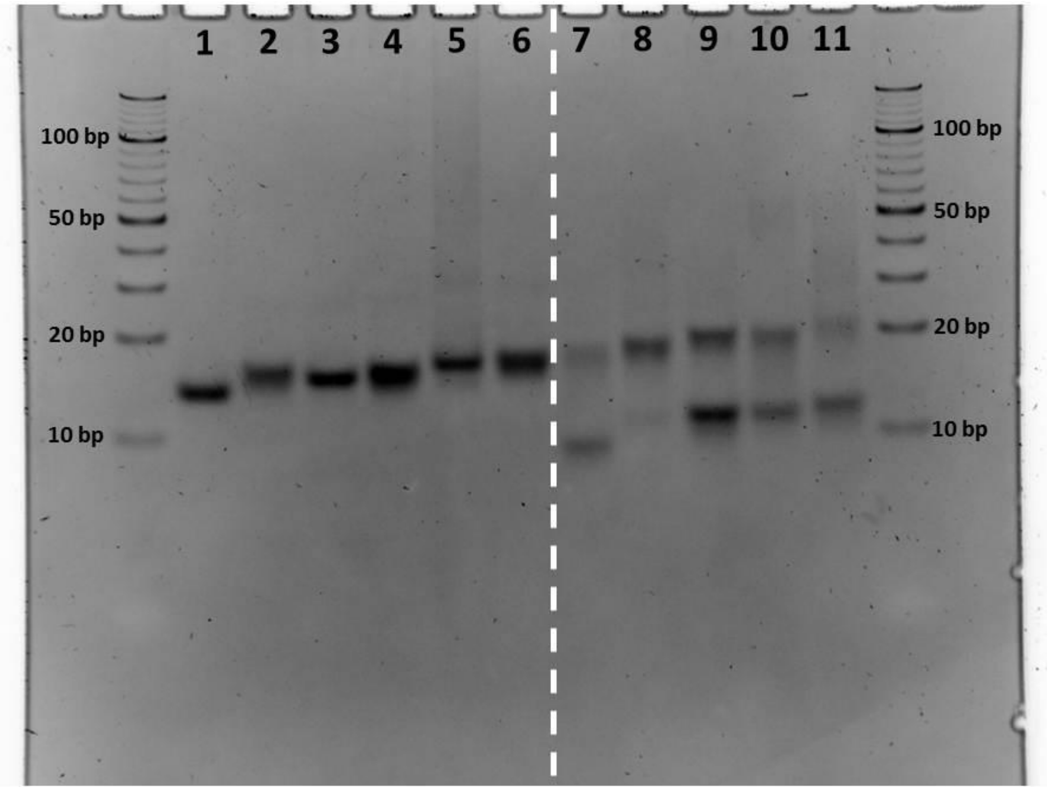

Figure 2.7: Nondenaturing PAGE gel electrophoresis of dsDNA after a smooth annealing process. From 1 to 11 are A(CG)$_3$T, AC$_3$G$_3$T, A(CG)$_4$T, AC$_4$G$_4$T, A(CG)$_5$T, AC$_5$G$_5$T, A(CG)$_6$T, AC$_6$G$_6$T, A(CG)$_7$T, AC$_7$G$_7$T, AC$_8$G$_8$T dsDNA sequences respectively. Hairpin bands with relative high gel mobility appear in long DNA molecules (from column 7 to column 11).

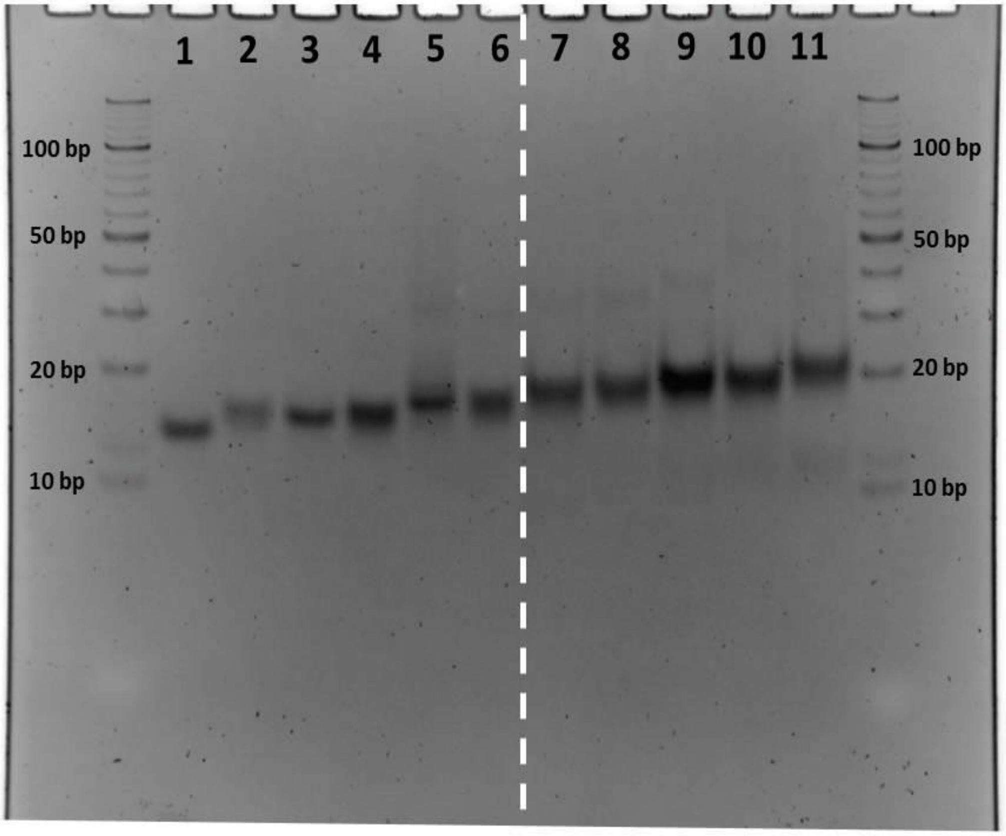

Figure 2.8: Nondenaturing PAGE gel of dsDNA after the programed annealing process. From 1 to 11 are $A(CG)_3T$, AC_3G_3T, $A(CG)_4T$, AC_4G_4T, $A(CG)_5T$, AC_5G_5T, $A(CG)_6T$, AC_6G_6T, $A(CG)_7T$, AC_7G_7T, AC_8G_8T dsDNA respectively. Only a single band was showed for each of the sequences.

For each of the dsDNA sequence, a conductance histogram was constructed from thousands of current-distance traces. A Gaussian fit was used to fit the conductance peak and the peak position was taken as the conductance value. See Figure 2.9 for all the conductance histograms.

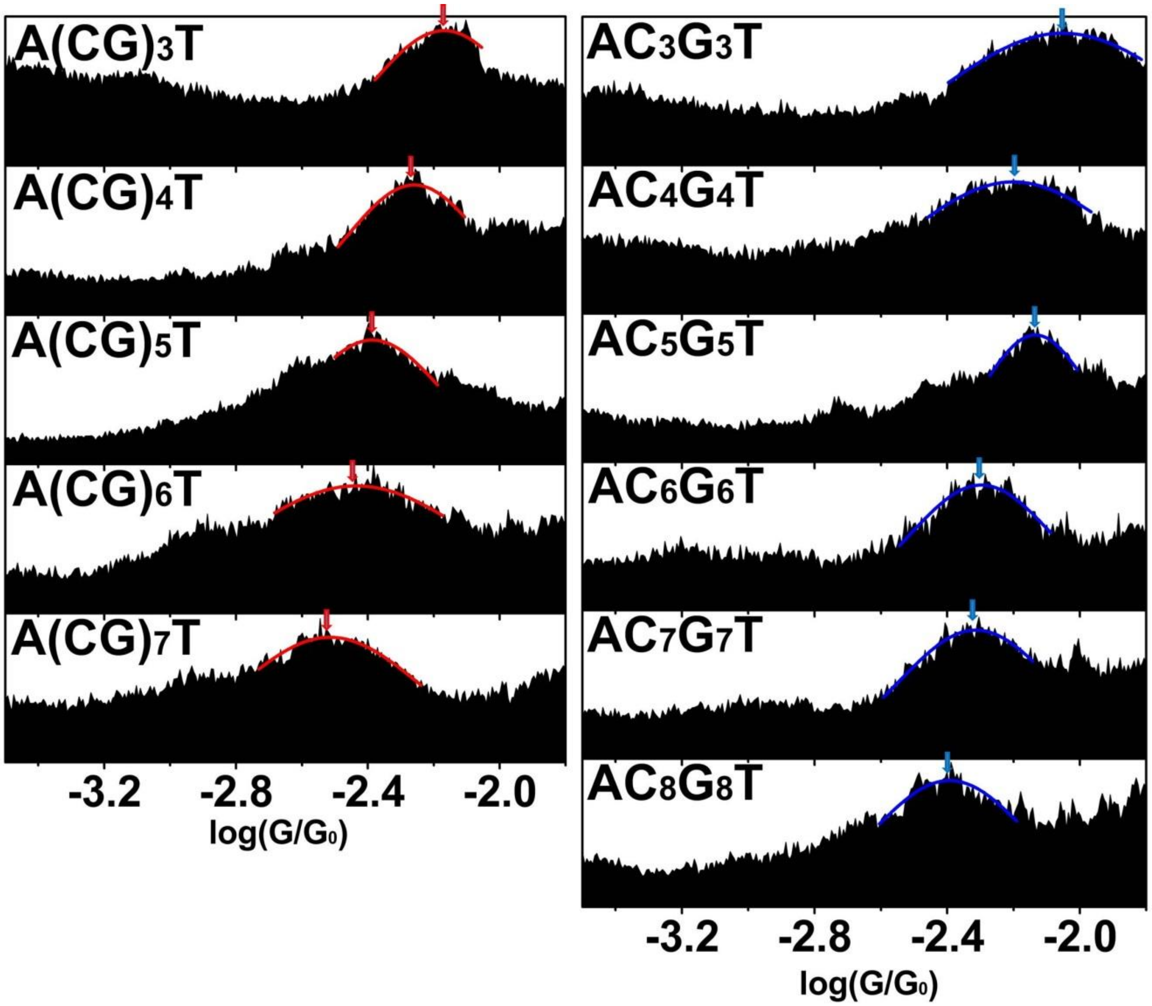

Figure 2.9: Conductance histograms of alternating and stacked double helical DNA.

To examine the robustness of the conductance measurements, the experiment for each DNA sequence was repeated three to four times. The results are presented as error bars in Figure 2.2, 2.4 and 2.5., and listed in Table 2.1, showing the reproducibility of the linear dependence and the oscillation behavior. The standard deviation was calculated by: $\sigma = \sqrt{\frac{1}{N}\sum_{i=1}^{N}\left(x_i - \mu\right)^2}$, where N is the number of sets, x_i is the peak position in each individual set of experiment and μ is the peak position obtained by compiling all the 3-4 histograms. Meanwhile it is worth to point out that the photo-induced electron transfer study of stacked G sequences may also showed a weaker oscillation in the charge transfer rate[102].

Table 2.1: Conductance values for all sets of experiments from alternating $A(CG)_nT$ and stacked AC_nG_nT sequences.

Sequences	**Exp.1**	**Exp.2**	**Exp.3**	**Exp.4**
$A(CG)_3T$	-2.17	-2.22	-2.17	
$A(CG)_4T$	-2.27	-2.31	-2.29	-2.27
$A(CG)_5T$	-2.35	-2.36	-2.37	
$A(CG)_6T$	-2.42	-2.46	-2.45	
$A(CG)_7T$	-2.50	-2.52	-2.56	
AC_3G_3T	-1.95	-2.00	-2.00	
AC_4G_4T	-2.19	-2.18	-2.22	-2.20
AC_5G_5T	-2.10	-2.16	-2.13	
AC_6G_6T	-2.29	-2.30	-2.22	
AC_7G_7T	-2.30	-2.33	-2.31	
AC_8G_8T	-2.35	-2.43	-2.44	-2.43

To check the robustness of the oscillation behavior, I also tried DNA sequences with thiol terminated group, same with the terminated group in Xu et al.'s work[69]. The oscillation behavior was also observed in the sequences with thiol terminated group, with a smaller amplitude (Figure 2.10). This is because in the DNA sequences with thiol terminated group, the contact resistance R_0 dominates the total resistance according to Equation 2.2.

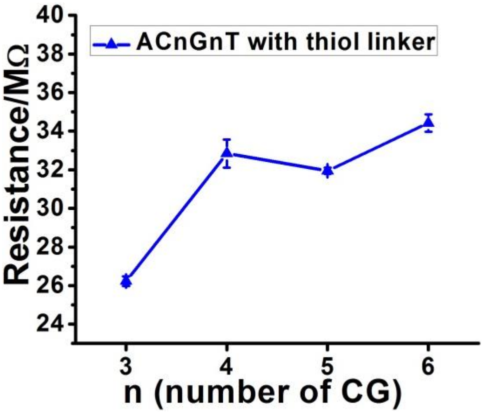

Figure 2.10: Resistance value of AC_nG_nT (n = 3,4,5,6) with thiol linker vs. number of CG.

To check the dependence of the resistance value on the bias voltage and bias polarity, I performed current-voltage (I-V) measurements on $A(CG)_4T$ and AC_4G_4T sequences. A linear and symmetry I-V was observed (Figure 2.11). Therefore, I concluded the resistance value of the dsDNA sequences does not depend on bias voltage or bias polarity.

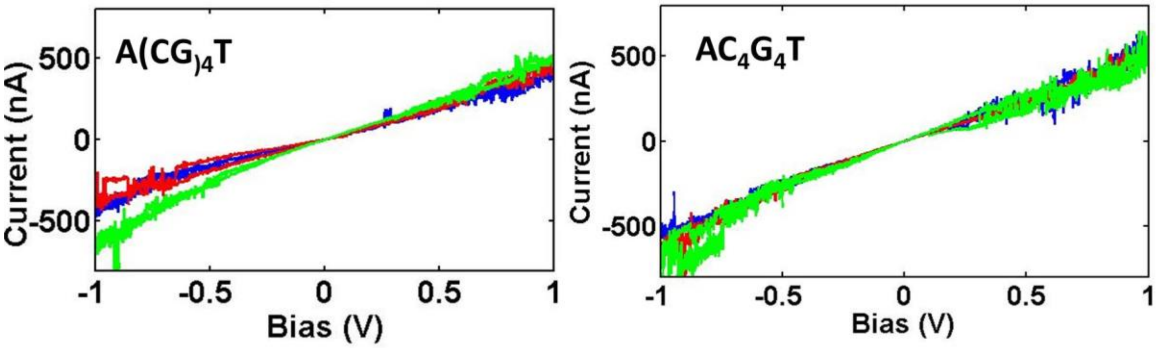

Figure 2.11: Representative individual current-voltage (I-V) curve of $A(CG)_4T$ (left) and AC_4G_4T (right) sequences. Note: The bias voltage range is limited by the leakage current which is caused by the electrochemical reactions of the system.

The electronic coupling strength in the calculations can be defined as:

$$H_{DA} = \langle \varphi_D | H | \varphi_A \rangle \text{, Equation 2.3}$$

where, φ_D and φ_A represent the diabatic wave functions of the donor and acceptor, respectively. Such states under the "two-state model" framework obtaining the diabatic molecular orbitals were approximated based on the block diagonalization of the adiabatic Hamiltonian of the whole system[103] at the INDO/S level of theory.

To better understand difference in the charge transport properties between the alternating and stacked G DNA sequences, the electronic structures of GCG (alternating) and G3 (stacked) segments were calculated. For the alternating segment, the HOMOs are mostly localized on a single G base and their energies are close to that of a GC base pair as shown in Figure 2.12. In contrast, the HOMOs of the G3 sequence are delocalized, and their energy levels split (Figure 2.13). These results indicate a strong electronic coupling between neighboring G bases in the stacked DNA sequences. The delocalization of the HOMOs of the stacked sequences challenges the traditional view of each base acting as a hopping site.

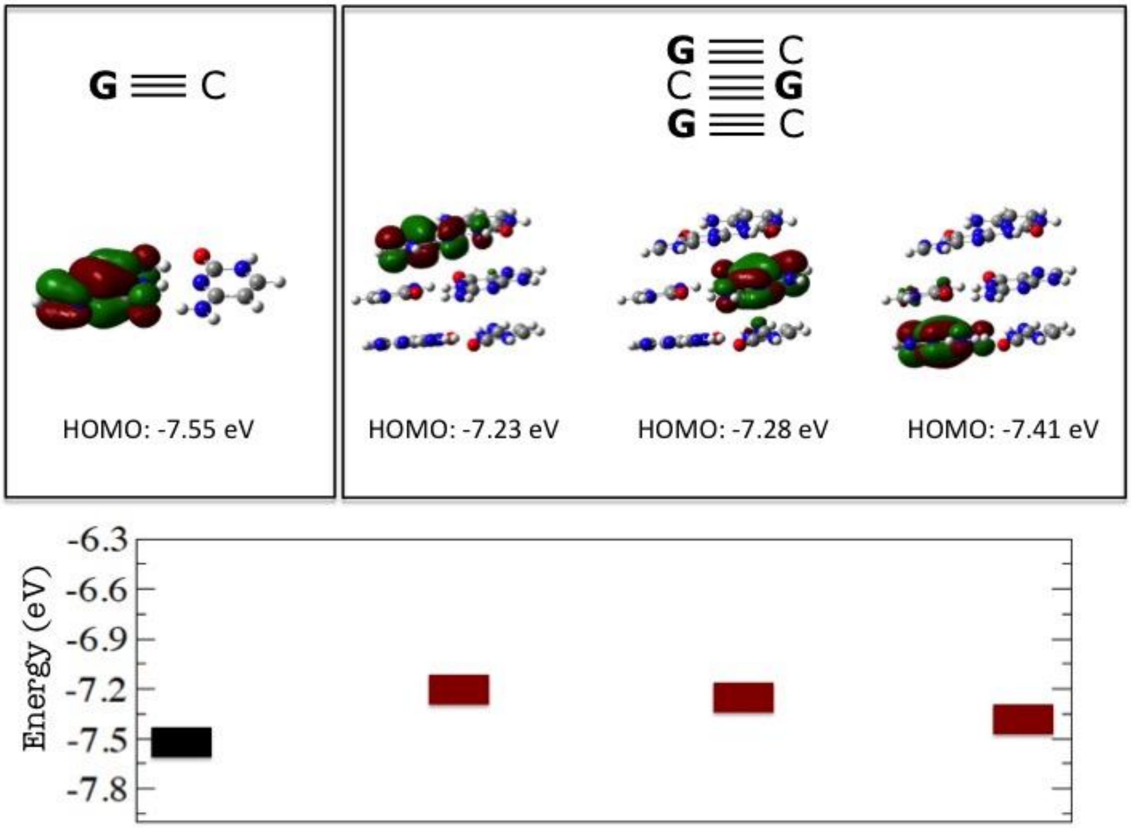

Figure 2.12: HOMOs (top) and their energy levels (bottom) of one G-C base pair, and GCG sequence. The HOMOs of GCG are localized and almost degenerate.

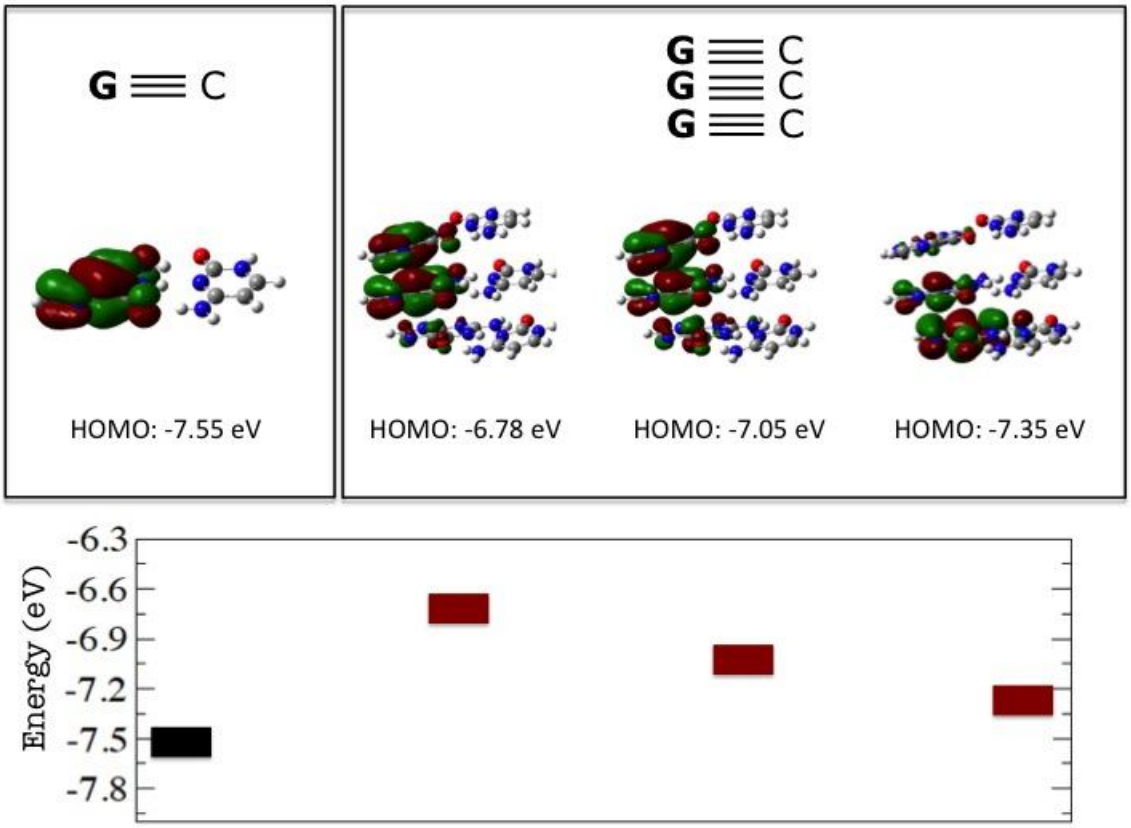

Figure 2.13: HOMOs and their energy levels of the G-C base pair, and G3 sequence. The HOMOs of G3 are delocalized and their energy levels split, due to the strong electronic coupling strength.

The spatial distribution for $(CG)_4$ and C_4G_4 is shown in Figure 2.14. As seen on the left panel, the HOMOs of the alternating sequences are mostly localized in single G base pairs while the stacked sequences show substantial delocalization (right panel). The energy levels of the alternating sequences are quasi degenerate while the energy levels of stacked sequences present a higher degree of energy splitting, indicating a strong electronic coupling in the latter case. The delocalization of the energy orbitals and strong electronic coupling in the stacked G sequences support the intermediate coherent and incoherent charge transport.

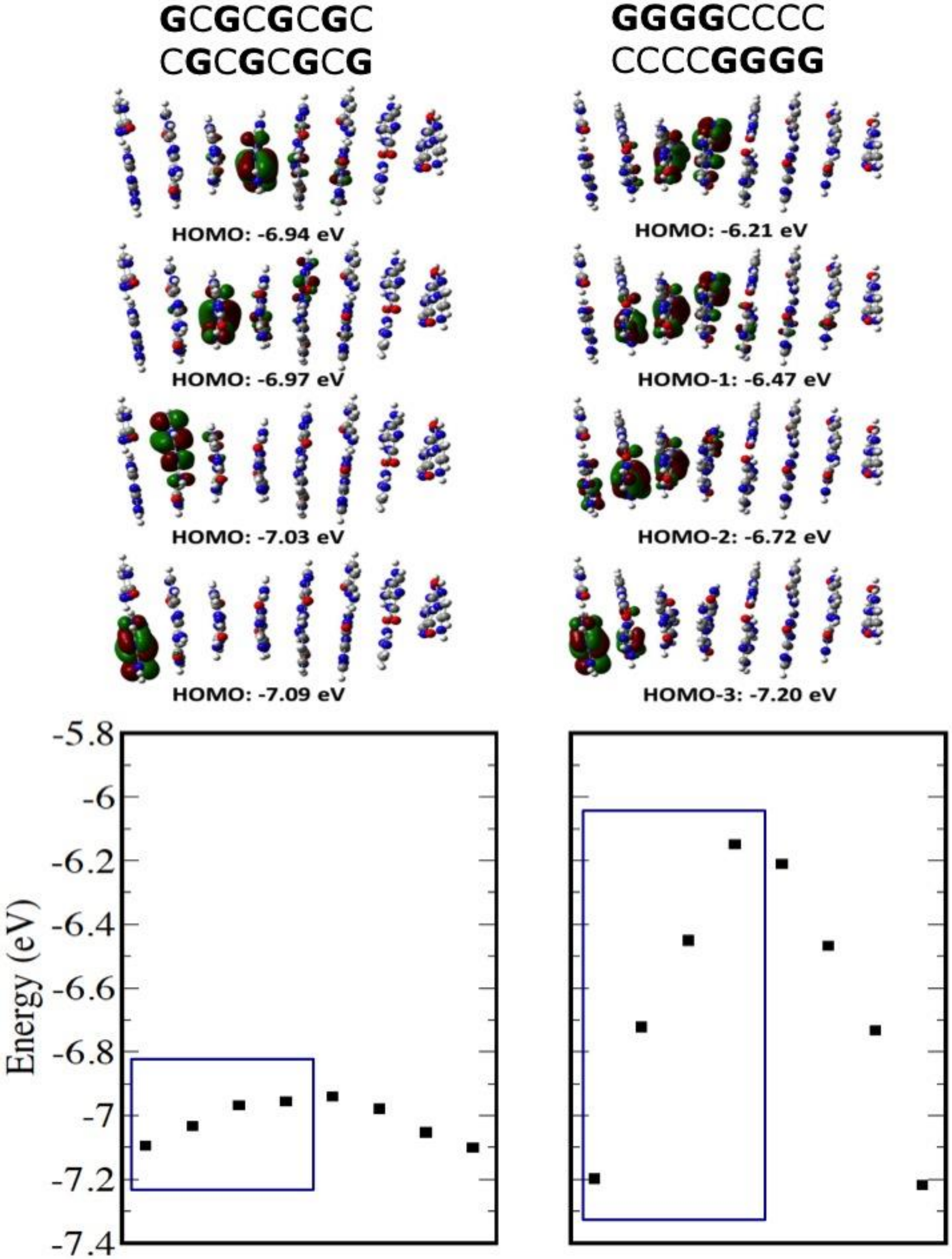

Figure 2.14: HOMOs and energy levels of $(CG)_4$ and C_4G_4.Top: Comparison of HOMOs between $(CG)_4$(left) and C_4G_4(right). Bottom: Energy diagram of the HOMOs of the

alternating (left) and stacked (right) sequences. The energy levels outlined by the square correspond to the HOMOs shown in the top panel.

To examine the robustness of the fitting of experimental data to the Büttiker model, I have considered the possibility of a phase shift, *Δϕ*, due to the interactions of the electron wave with the boundaries, and Equation 2.2 becomes,

$$R_{tot} = R_0 + \frac{h}{e^2}\frac{N-1}{1-2e^{-B(N-1)}\cos\left[C\left(N-1\right)+\Delta\phi\right]}T_{GG-st}^{-1}$$, Equation 2.4

From the fitting, the unit resistance $\frac{h}{e^2 T_{GG-st}}$ = 0.32±0.01 MΩ, B = 0.56±0.07 nm^{-1}, C = 2.5±0.2 rad and $\Delta\phi$ = -0.5±0.6 rad. The fitting quality, and major parameters, $\frac{h}{e^2 T_{GG-st}}$, B and C remain unchanged by including the phase shift, $\Delta\phi$, in the fitting (Figure 2.15).

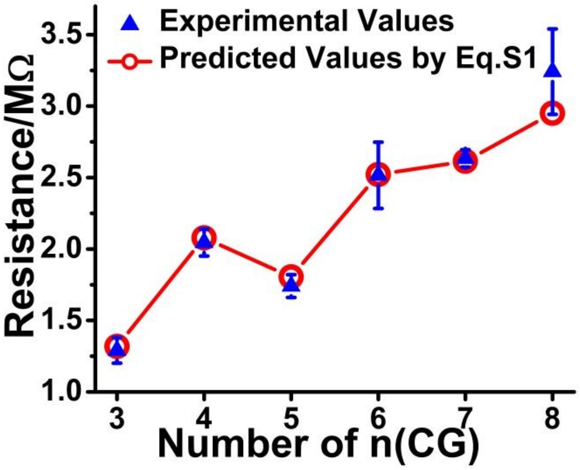

Figure 2.15: Fitting to Equation 2.4 (the Büttiker model with a phase shift associated with the reflection of electron waves at the boundaries of the molecular junction).

I also performed the fitting by regarding the contact resistance as an unknown parameter (Figure 2.16). From the fitting, the unit resistance $\frac{h}{e^2 T_{GG-st}}$ = 0.35±0.03 MΩ, B = 0.53±0.05 nm, and C = 2.38±0.05 rad, which are similar to the parameters with fixed R_0. The parameters obtained from the fitting almost remain the same, which further indicate the robustness of the fitting.

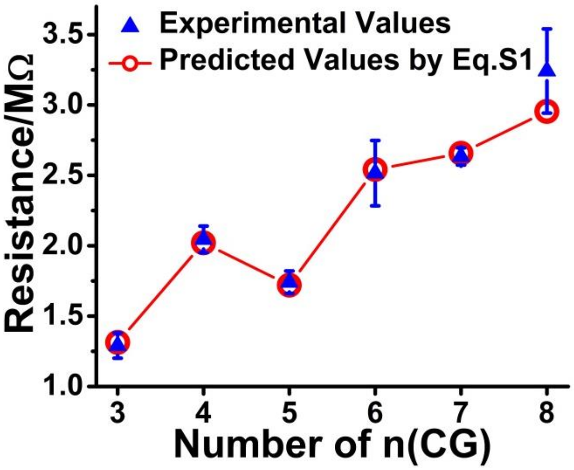

Figure 2.16: Fitting to the Büttiker model with the contact resistance as a fitting parameter (rather than fixed as assumed in Figure 2.5).

2.8 Conclusions and perspectives

In this chapter I studied charge transport in dsDNA with alternating G and stacked G sequences[104]. In the former case, the resistance increases linearly with the number of base pairs (length) that can be described with the hopping model, in which each G base acting as a hopping site. In the latter case, the overall resistance follows the linear dependence but there is a periodic oscillation superimposed on the linear dependence, indicating coherent corrected hopping regime of charge transport. Then by calculations I revealed that the HOMOs in the stacked G are delocalized over several G bases, which supports the observation of the partially coherent tunneling and incoherent hopping charge transport mechanism. The experimental resistance vs. length dependence for stacked sequences can be modeled based on the Büttiker's theory.

The present work used a phenomenological description which involves partial coherence[104], but the studies do not establish the specific physical origins of the coherence, nor do they provide testable molecular designs that might be used to manipulate the coherence. Collaborating with Prof. David N. Beratan's group, we establish a first-principle theory and enable the engineering of molecular assemblies that support extended coherent transport, and these principles are tested in DNA structures. The theory found that orbital symmetry (even or odd number of Guanines) controls the resistance oscillation in the resistance of DNA, and that weakening the interaction between two stacked-G segments can enhance the oscillation. This work will be published and discussed elsewhere.

CHAPTER 3

SELF-ASSEMBLING CHARGE SPLITTER AND CHARGE TRANSPORT JUNCTIONS BASED ON GUANINE QUADRUPLEXES

The work in this chapter is contributed by my collaborators Ruojie Sha, Chaoren Liu, Alexander Balaeff, David N. Beratan, Nongjian Tao, Nadrian C. Seeman and me.

3.1 Introduction

The studies of double-stranded DNA have produced a molecular-level understanding of charge transfer and transport mechanisms in these biological macromolecules[62, 68, 72, 73, 87]. Yet, the dream of self-assembling circuitry at the nanoscale demands junction structures that can gate charge flow[29, 105]. It is widely accepted that current in DNA flows down the stack of nucleotide base pairs[87, 101], and current flowing through different helixes in DNA double crossover (DX) molecules does not interfere with each other despite the crossovers in the backbone[106]. To design a current splitter or combiner with DNA, a diverging splitting route of base stacking is necessary. One of the approaches is splitting one double-stranded DNA into two double-stranded DNA to form a “Y” shape three-way junction (Figure 3.1a) by Young et al.[107], though the charge transport efficiency is small compared to duplex DNA due to the weak base stacking at the crossing. To keep a strong base stacking, one possible way is to use extending guanine quadruplex (G4) with duplexes (Figure 3.1b) proposed by Venczel and Sen[108]. In this design, the charge injected from different duplexes merges in G4 and exits to two other duplexes, thus providing a prototype for the charge splitter and charge combiner. A photochemical study of these G4 junctions achieved charge splitting to different duplexes when the junctions were stabilized by counter-ions K^+ and Sr^{2+}. However, the charge transfer to different directions is measured by measuring the guanine oxidation on duplex branches, which is different from a steady charge flowing in electronic devices[109].

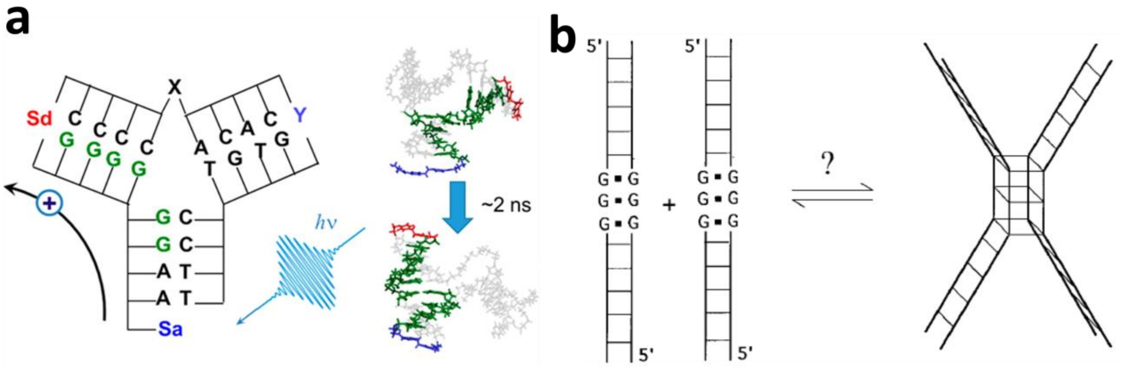

Figure 3.1: Two possible designs to realize a charge splitter based on DNA. (a). A “Y”-shape three-ways junction constructed from double stranded DNA. Photochemical study indicates charge can transfer from Sa to Sb locating at different ends (one as shown in the picture and another is replacing the Y. Reprinted with permission from ref. [107]. (b). Another possible design of charge splitter using the G-quadruplex structure with extending duplexes as the arms. Reprinted with permission from ref. [108].

In this chapter, I investigate the charge transport properties of two series of G4-duplexes junctions based on the structure of extending G-quadruplex with duplexes using Scanning Tunneling Microscopy break junction technique and computational simulations. By connecting one duplex to one electrode and varying the duplex which connects to the other electrode (denoted as L1-2 and L1-4, see Figure 3.2a), I found their conductance values are nearly the same, indicating charge can go through two different pathways. However, the conductance of these G4-duplex junctions is much smaller than that of DNA duplex with the same sequence. Molecular dynamics simulations suggest that the lower conductance is mainly due to the weak base stacking at one G4-duplex interface which is caused by duplex backbone repulsion and geometrical mismatch between G4 and duplexes. By removing one duplex arm and adding a flexible linker between the G4 and duplex, the conductance of the modified G4-duplex can reach up to the conductance level of duplex. Molecular dynamics simulations reveal a recovered G4-duplex base stacking in the modified junctions, supporting the experimental findings. The studies suggest charge-combining and charge-splitting structures, and further confirm the importance of base stacking in charge transport through DNA structures, which will be helpful towards building up single molecular devices based on DNA in the future.

3.2 Methods

Synthesis of DNA strands. All DNA strands were synthesized on an Applied Biosystems 394 DNA synthesizer, removed from the support, and deprotected using routine phosphoramidite procedures.All DNA strands have been purified by denaturing polyacrylamide gel electrophoresis.

Assembly of G4-duplex. G4-duplex was annealed using the following annealing protocol: 5 minutes at 95 ℃, 1 hour at 65 ℃, 16 hours at 37 ℃, 4 hours at room temperature in 100 mM Na_2HPO_4, 100 mM KH_2PO_4, 10 mM Mg Acetate, pH ~7.5 at 5 μM final DNA concentration. G4-duplex were then purified by native PAGE on a temperature-controlled unit maintained at 20 ℃. Bands were visualized by UV shadowing, cut out and electro-eluted in 100 mM Na_2HPO_4, 100 mM KH_2PO_4, 10 mM Mg Acetate, pH ~7.5 inside 3500 MWCO dialysis membrane on a horizontal electrophoresis unit. After the electro-elution, the solutions of G4-duplex were concentrated by using Millipore Amicon Ultra-0.5 Centrifugal Filter Units (NMWL 3,000) and a native gel was run to check the purity of those purified G4-duplex.

Conductance measurement. I carried out the measurements in a 1 μM DNA solution at room temperature (22 ℃). 50 μL phosphate buffer (same with the one used in assembly of G4) was added into the sample holder. A small bias voltage (varying from 10 mV to 100 mV, positive or negative) was applied between the gold tip and the gold substrate in the STM break junction measurement (Figure 3.2a). Exponential decay in the current-displacement (I-d) traces was observed in the phosphate buffer in the absence of DNA molecules. However, once 10 µL DNA solution of 5 µM was added, plateaus would be observed in the I-d traces. I collected a large number of I-d traces (~4000) in each experiment, and constructed conductance histograms with an algorithm described previously[110]. The algorithm counted only the traces showing counts exceeding a preset threshold in the histograms. For each sequence, the measurement was repeated at least 3 times to obtain the standard deviation. Control experiment with buffer solution was also performed under the same condition with no peaks revealed in the histogram.

Molecular Dynamics Simulation. A 6-layer anti-parallel G quadruplex is built from the crystal structure of PDB:2AVH. Four DNA duplexes d(ACCG), d(CGAC), d(GCGA) and d(AGTG) are obtained from *model.it*. The attachment of duplex to the G4-duplex is optimized with respect to the stacking distance and helical parameters. The prepared G4 junctions are solvated in a 90Å×90Å×90Å water box with >15 Å padding water layer between nucleic acids and box boundary. Counter-ions of 200 Na^+, 100 K^+, 10 Mg^{2+} and 268 Cl^- are added in the solvent, which were also used in synthesis and measurements. 5 of the K^+ ions are put along the axis of the 6-layer G4 to stabilize to structure. After the solvated G4-junctions are minimized, the water molecules and counter-ions are equilibrated for 2 ns in room temperature. To avoid being trapped at the initial structure, the systems undergo a MD annealing, where several bonds between strands are applied to hold composition in high temperature. During the annealing, the systems are heated up to 90 ℃ for 0.5 ns and the temperature is gradually lowered to 40 ℃ in 0.5 ns, followed by 0.5 ns running in 40 ℃ and 0.5ns running in 25 ℃. This annealing procedure repeats 3 times. The annealed structures will be equilibrated for 5ns at room temperature (25 ℃) before production run.

Quantum Calculations. The quantum simulation of nucleic acids is conducted with ZINDO method in Gaussian 09. Since the charge transport in DNA is mediated by bases, backbones and solvents are not included in the calculation. The dangling bonds are passivated with hydrogen atoms.

NEFG Methods (Laudauer approach). In the Landauer formulism, the conductance is given by Equation 3.1.

$$I(V) = \frac{q}{h}\int T(\varepsilon)\,[f_L(\varepsilon) - f_R(\varepsilon)]d\varepsilon, \text{ Equation 3.1}$$

The f_L and f_R are Fermi functions for the left and right contacts. $T(\varepsilon)$ is the transmission coefficient $T(\varepsilon) = Tr[\Gamma_L G \Gamma_R G^+]$ and $G(\varepsilon) = \frac{1}{(\varepsilon I - H - \Sigma_L - \Sigma_R)}$, where H is the Fock matrix of the molecule and Σ , the self energy matrix, is the energy shift (real part) and broadening (imaginary part) induced by coupling to the electrodes. Here, energy shifting is not considered in the weak coupling limit. The broadening matrix $\Gamma_{R/L} = i(\Sigma_{R/L} - {\Sigma_{R/L}}^{+})$ is equal to the imaginary part of the self energy matrix. In the atomic basis set, the broadening matrix $\Gamma_{R/L}$ are a diagonal matrix with non-zero values at nitrogen and carbon s and p orbitals (ingredient of G HOMO) of the guanines at the input and output sites of the G4-duplex. Because the charge interchanges between G4-duplex and duplexes are mediated mostly by guanines, transmission energy (Fermi energy) is approximated by the average site energies of individual guanines.

3.3 Sequences design

The first series of G4-duplex is shown in Figure 3.2b. They were denoted as “conformation”-“serial code”-“number of G4 layer”-“linker position”. The structure enforces the antiparallel or parallel conformation in terms of the G4 backbone, denoted as “Anti” or “Para” respectively. The number of G4 layers varies from 5 to 6. The first series of G4-duplex is non-modified and the second series of G4-duplex is modified, denoted as “N” and “M” respectively. Finally, the positions of the two linkers connecting to the electrodes can be strand 1&2 or strand 1&4, denoted as L1-2 or L1-4 respectively. As an example, Anti-N5-L1-2 means Antiparallel Non-modified G4-duplex with 5 layers of G4 and Linker positions at strand 1&2. Note that the double helices above the G4 layers are paired differently from those below the G4 layers, allowing a two-fold axis of symmetry perpendicular to the G4 helix axis. To avoid the assembly of the mixture of duplex DNA configurations resulting from this symmetry, I have chosen DNA sequences with Watson-Crick base pairing partners above the tetrad that differ from the pairing partners below it. The amino groups were attached to the T base for surface binding to Au electrodes[104]. Sequences of L1-2 differ from L1-4 by exchanging the two duplexes at the bottom end of the G4 to keep the sequence involved in the transport pathway the same, although there may be detailed conformational differences between the pathways because of structural asymmetry of the G4-duplex. Finally, the corresponding dsDNA with the same sequence as the control experiment is shown in Figure 3.2c.

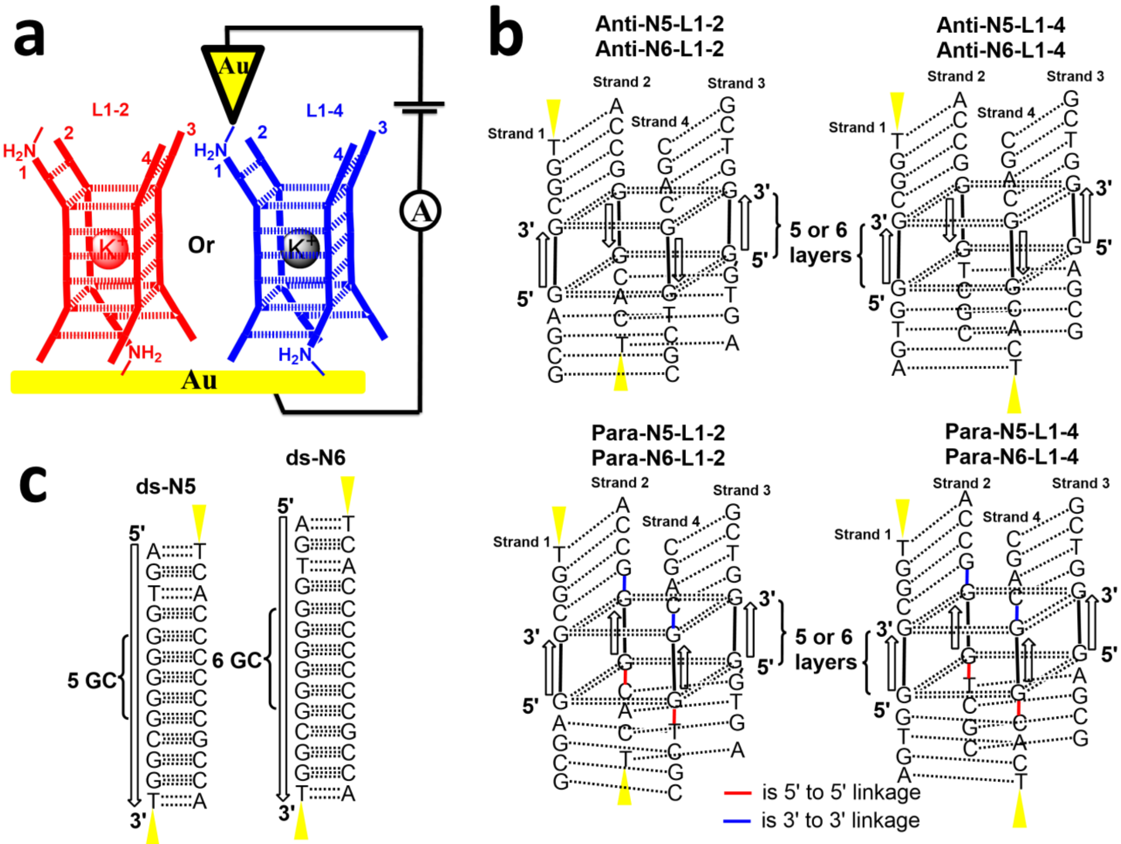

Figure 3.2: Experimental setup, structure and sequence design of non-modified G4-duplex DNA and the corresponding DNA duplex. **(a).** Conductance measurement via STM break junction technique. G4-duplex DNA bridges between the Au tip and Au

substrate via the amino group on modified T base. See text for more details on the measurements. **(b).** L1-2 (left) and L1-4 (right) G4-duplex with 5 or 6 layers of G4. The Guanines form hydrogen bonds with its neighboring Guanines and the whole structure is stabilized by the K^+. By inserting two 3' to 3' linkages at the top two duplexes (blue line) and two 5' to 5' linkages (red line) at the bottom two duplexes, one can obtain parallel conformation (bottom) instead of the antiparallel conformation (top) for the G-quadruplex in the G4-duplex structures. **(c).** DNA duplex with 5 GC or 6 GC base pairs instead of the G4 layers in the G4-duplex structure. Arrows indicate the direction of the backbone from 5' to 3'. Black dashed lines indicate hydrogen bonds. Gold triangles indicate the binding points of Au electrodes.

The purity of the G4-duplex samples was checked by 10% native PAGE gel. As seen from Figure 3.3 to 3.6, all the G4-duplex samples exhibit a single band at around 40 bp, comparing to the duplex band at around 20 bp. These indicate the formation of the desired G4-duplex samples.

Figure 3.3: Gel of Anti conformation non-modified G4-duplex. 10% native PAGE was run at 20 ℃ in 100 mM Na_2HPO_4, 100 mM KH_2PO_4, 10 mM Mg Acetate, pH ~7.5. Lane 1 contains the DNA molecular weight marker. Lane 2 contains Anti-N6-L1-4 G4-duplex structure. Lane 3 contains Anti-N6-L1-2 G4-duplex structure. Lane 4 contains Anti-N5-L1-4 G4-duplex structure. Lane 5 contains Anti-N5-L1-2 G4-duplex structure. Lane 6 contains ds-N6 double-stranded DNA.

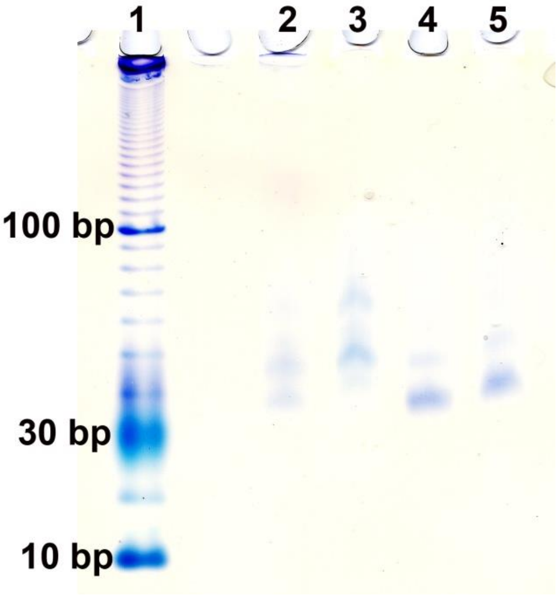

Figure 3.4: Gel of Anti conformation modified G4-duplex. 10% native PAGE was run at 20 ℃ in 100 mM Na_2HPO_4, 100 mM KH_2PO_4, 10 mM Mg Acetate, pH ~7.5. Lane 1 contains the DNA molecular weight marker. Lane 2 and lane 3 are other designs with unstable G4-duplex structures which are not used in this work. Lane 4 contains Anti-M6-L1-4 G4-duplex structure. Lane 5 contains Anti-M6-L1-2 G4-duplex structure.

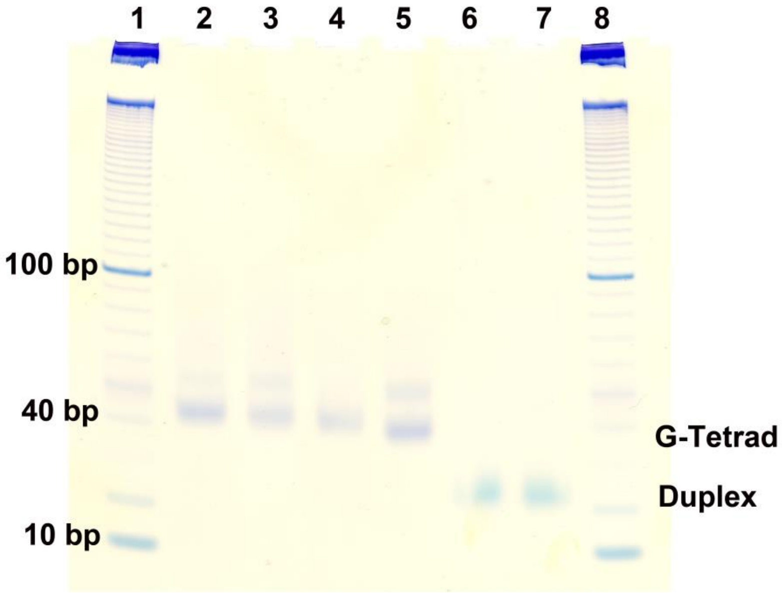

Figure 3.5: Gel of Anti or Para conformation modified G4-duplex. 10% native PAGE was run at 20 ℃ in 100 mM Na_2HPO_4, 100 mM KH_2PO_4, 10 mM Mg Acetate, pH ~7.5. Lane 1 contains the DNA molecular weight marker. Lane 2 contains Anti-M5-L1-2 G4-duplex structure. Lane 3 contains Anti-M5-L1-4 G4-duplex structure. Lane 4 contains Para-M6-L1-2 G4-duplex structure. Lane 5 contains Para-M6-L1-4 G4-duplex structure. Lane 6 contains ds-M6 double-stranded DNA. Lane 7 contains ds-M5 double-stranded DNA. Lane 8 contains the DNA molecular weight marker.

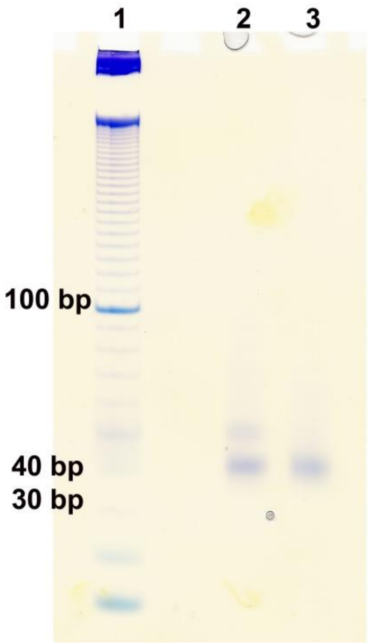

Figure 3.6: Gel of Para conformation modified G4-duplex. 10% native PAGE was run at 20 ℃ in 100 mM Na_2HPO_4, 100 mM KH_2PO_4, 10 mM Mg Acetate, pH ~7.5. Lane 1 contains the DNA molecular weight marker. Lane 2 contains Para-M5-L1-4 G4-duplex structure. Lane 3 contains Para-M5-L1-2 G4-duplex structure.

3.4 Conductance measurements

I carried out conductance measurements using STM-BJ technique (Figure 3.7a)[12]. The amino modified T was employed as the linker group, which has been shown to be an efficient linker[104]. The Au tip was coated with a wax insulation layer, which reduced the ionic leakage current below 1 pA[69]. Phosphate buffer with K^+ ion was added onto the Au surface. The tip was then pushed towards and retracted from the Au substrate repetitively. During the retracting process, the current was recorded vs. distance (I-d) and a smooth exponential decay trace indicates a clean Au surface (black trace in Figure 3.7b). Then 5 uM of G4-duplex solution was added and the experiments were repeated again. I-d traces with plateau features signal the formation of Au-DNA-Au molecular junction (blue trace in Figure 3.7b). Thousands of I-d traces were collected for each DNA sample, from which a conductance histogram was constructed (Figure 3.7c). The peak in the histograms was fitted with a Gaussian distribution where the peak position was taken as the most probable conductance of a single Au-DNA-Au molecular junction. Each G4-duplex was measured at least three times to obtain the experimental error in the conductance value.

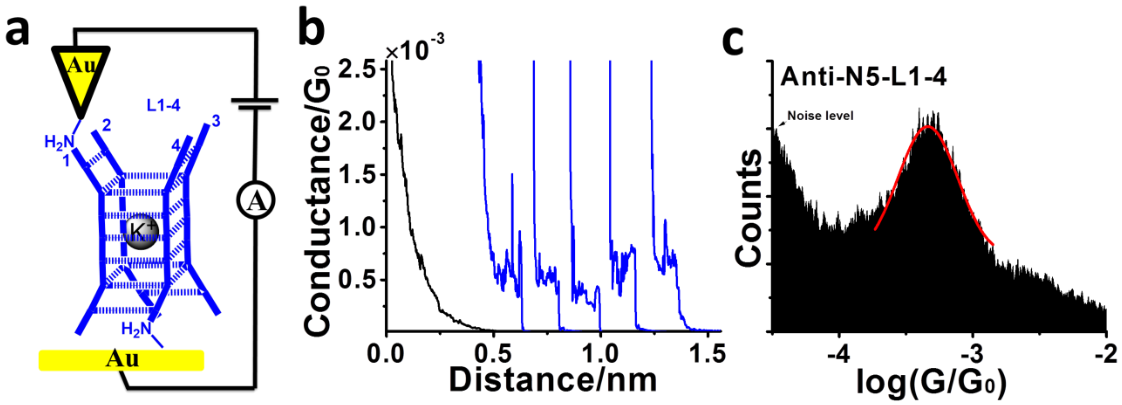

Figure 3.7: Measurement of charge transport in G4-duplexes junctions and dsDNA. **(a).** DNA molecules connected to two electrodes via the amino group on T base. **(b).** Representative current-displacement traces (current has been converted to conductance) of Anti-N5-L1-4 G4-duplex junctions (blue lines) in aqeuous solution showing plateau features in the traces, and control experimets performed in the absence of DNA molecules showing exponential decay (black lines). **(c).** Conductance histograms of Anti-N5-L1-4 G4-duplex junctions constructed from thousands of individual traces, then fitted by a Gaussian distribution function, where the peak position (blue line) indicates the conductance of the molecule. The noise level is due to the lower limit of the current

amplified in the STM scanner, which can also been seen in control experiment in buffer solution below.

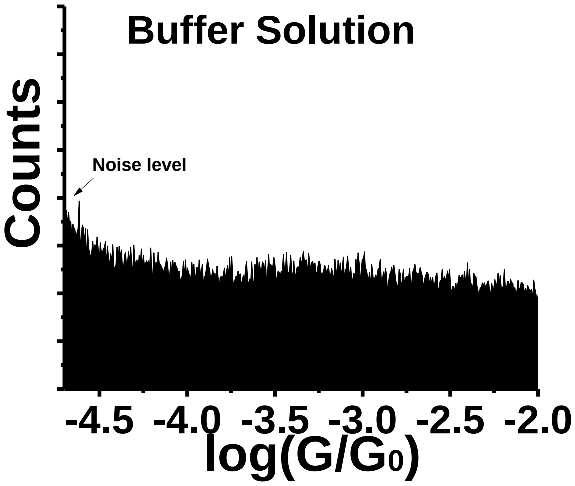

Figure 3.8**:** Histogram of phosphate buffer solution as a control experiment. No peaks are revealed. The noise level is due to the lower limit of the current amplified in the STM scanner.

Figure 3.9 (also in Table 3.2, for conductance histograms see Figure 3.10 to Figure 3.12) shows the conductance of Anti conformation (black points), Para conformation (red points) and double-stranded DNA (blue points), from which I can draw two conclusions. First, the conductance values of L1-2 and L1-4 are nearly the same, regardless of the Anti or Para conformation and number of G4 layers. This indicates the charge transport efficiency along the two different pathways is almost identical to each other. Charge injected from one of the DNA duplexes on the top can be detected on the two DNA duplexes on the bottom with almost equal probabilities, thus a charge splitter can be built up. This conclusion is supported by the G4 conductance calculations (see below) and other reported theoretical calculations[111]. Second, comparing to the conductance of dsDNA, all the G4-duplex have a much smaller conductance value (about one fifth). This is surprising as one would expect charge transport through G-quadruplex is more conductive than that through DNA duplex[111]. I will discuss each of them below.

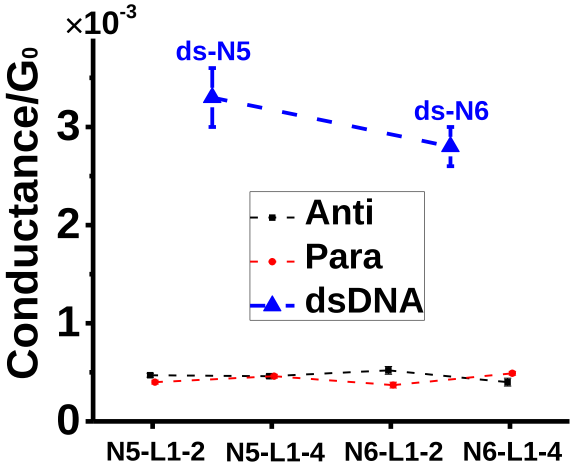

Figure 3.9: Conductance of non-modified G4-duplex in Anti and Para conformation and the duplex. The conductance of all the G4-duplex (red and black points) are all around 5×10^{-4} G_0 (see Table 3.2), which are much smaller than the conductance of dsDNA (blue points) with the same sequence.

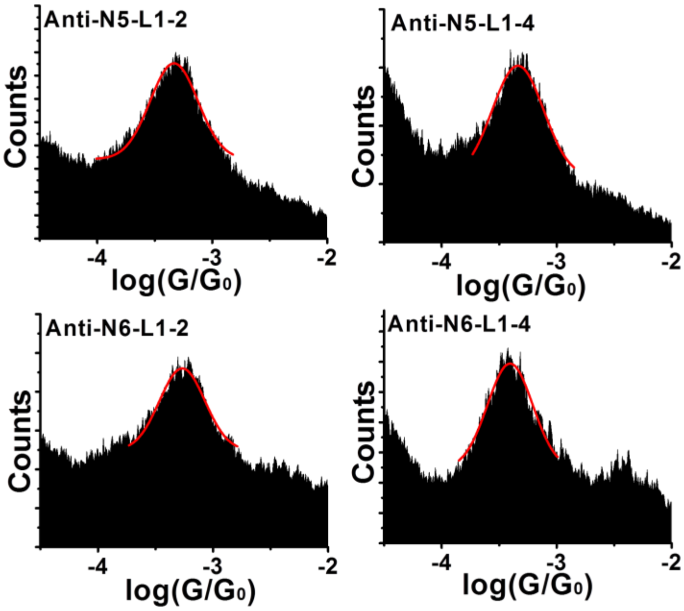

Figure 3.10: Conductance histograms of non-modified antiparallel G4-duplex.

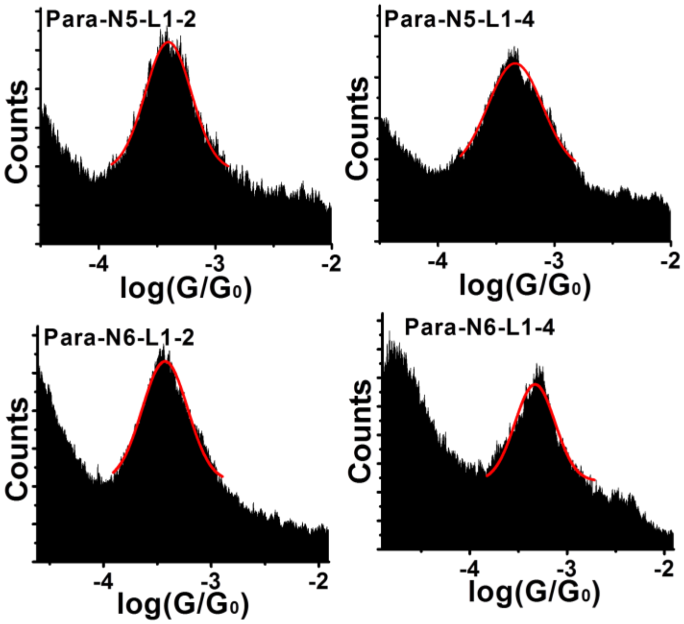

Figure 3.11: Conductance histograms of non-modified parallel G4-duplex.

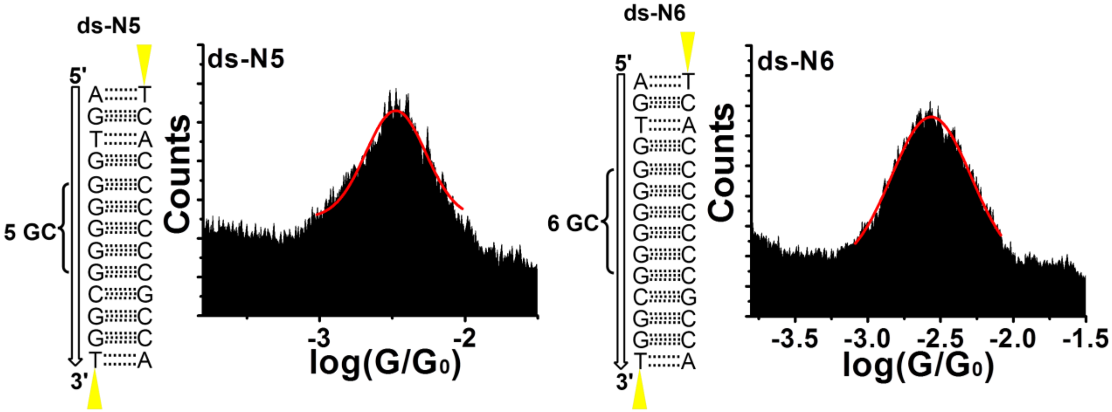

Figure 3.12: Structures and conductance histograms of double-stranded DNA as a comparison for non-modified G4-duplex.

3.5 Three dimensional structure analysis

Molecular dynamics simulations were used to study their 3D structures. First, one layer of G4 from Anti conformation and Para conformation was extracted and compared with one GC base pair in DNA duplex. The distance between two strands in G4 and in duplex is found to be different. The distance between two strands for one GC base pair is 17.5 Å (Figure 3.13c). The shape of a G4 layer in Anti conformation is a rectangle with a long side of 17.7 Å and a short side of 12.6 Å (Figure 3.13a), consistent with the results from the crystal structure PDB: 2AVH. The shape of a G4 layer in Para conformation is a square with each side of 16 Å (Figure 3.13b). A distance mismatch between duplexes and G4 strands was noticed, especially when a duplex is connected to the shorter side of the Anti G4.

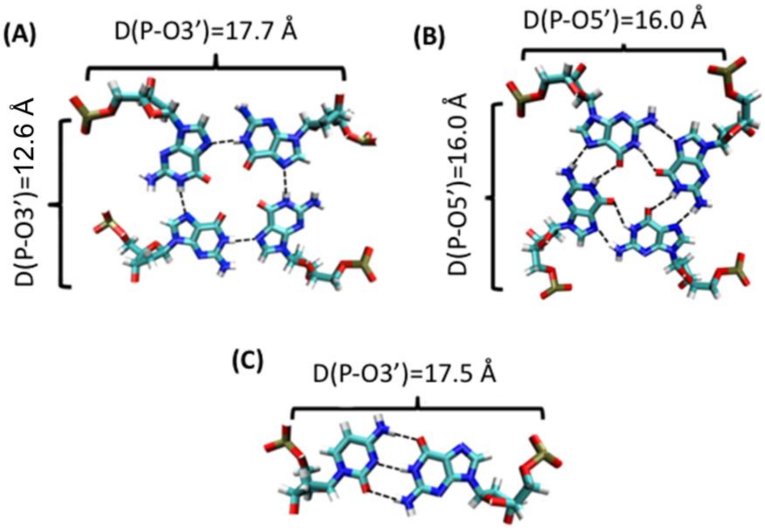

Figure 3.13: The distance between two paired bases in Anti conformation G4-duplex, Para conformation G4-duplex and DNA duplex. (a) The average structure of a G-tetrad in anti-parallel G-quadruplex. (b) The average structure of a G-tetrad in parallel G-quadruplex. (c) The average structure of a base pair in B-type DNA. Structures are averaged from a 1 ns molecular dynamics simulations.

The Guanine in the G4 layers can adopt *anti*- or *syn*- conformations, which differ by a rotation angle around the bond linking 1′-carbon on deoxyribose sugar and the N on the nucleobase (Figure 3.14a). All the Guanines will adopt *anti*- conformation in the Para conformation, but the Guanines in each strand of Anti conformation G4 will adopt *anti*- and *syn*- conformation alternatively (Figure 3.14b, c and d). For example, the six Guanines in one strand of Anti-N6-L1-4 can be *anti-syn-anti-syn-anti-syn* or *syn-anti-syn-anti-syn-anti* (Figure 3.15a). Additionally, Anti- G4 has asymmetric side length, so there are four stereoisomers for Anti-N6-L1-4 (denoted as C1 to C4 in Figure 3.15a). Although strands in Para- G4 are symmetric, different directions of duplex minor grooves and major grooves induce two stereoisomers for Para-N6-L1-4 (denoted as C1 to C2 in Figure 3.15b).

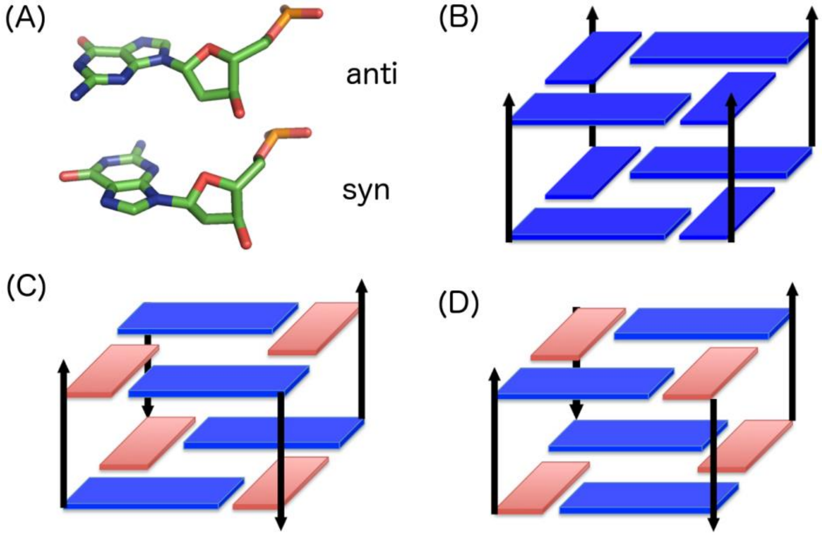

Figure 3.14: The conformation of each Guanine base in the G4 layers. (a). Guanines in *anti* and *syn* positions. (b). two stacking G-tetrads in parallel G quadruplex. (c). 5'anti-syn3' stacking G-tetrads in anti-parallel G quadruplex. (d). 5'syn-anti3' stacking G-tetrads in anti-parallel G quadruplex. Four straight arrowed lines indicate backbone directions. anti is in blue and syn is in red.

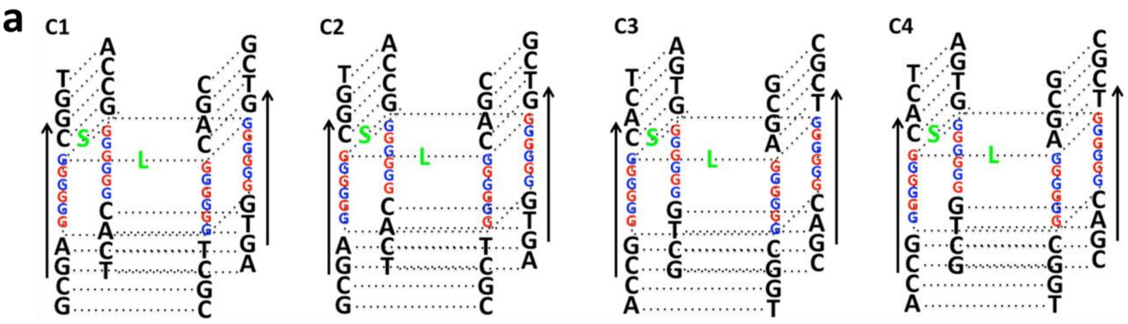

Anti-N6

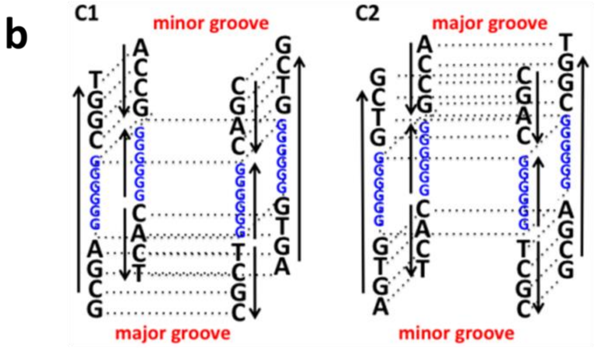

Para-N6

Figure 3.15: Different stereoisomers for Anti-N6 (and M6) and Para-N6 (and M6). (a). Possible conformation (C1-C4) for Anit-N6 (and M6) G4-duplexes. Green "S" and "L" indicate the shorter side and longer side of the G-quadruplex. The guanines in G-quadruplex are colored red or green if they are in "syn" or "anti" positions respectively. Arrowed lines indicate the backbone directions. The other two backbones without arrowed lines run from the top to the bottom. Two duplexes on the top face each other with the minor grooves, while two duplexes at the bottom face each other with their major grooves. (b). Possible conformations (C1-C2) of Para-N6 (and M6) G4-duplexes. The guanines in G-quadruplex are colored green and they are in "anti" positions. Arrowed lines indicate the backbone directions. 3'-3' linkers and 5'-5' linkers are needed to connect backbones with the opposite directions. Red colored "minor groove" and

“major groove” mean two duplexes face each other on their minor groove and major groove side respectively.

3.6 Electronic coupling and conductance calculations

The conductance through the G-quadruplex with Landauer approach was examined. The conductance is averaged with 4000 snapshots, which are extracted from 200 ns MD simulations of the G-tetrads. In the Laudauer calculation, electrodes couple with one G at the top layer and with another G at the bottom layer (see Figure 3.16 for Anti 6layers G4 as an example). The calculated conductance values when electrodes are connected to various positions are listed in Table 3.1. The conductance varies by less than 4 times for different contact positions, agreeing with the conductance of 8-layer parallel G4 junctions[111].

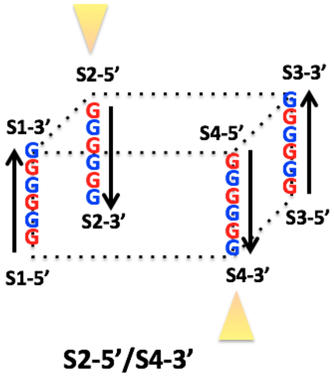

Figure 3.16: 6-layer G tetrads with S2-5’/S4-3’ electrode attachment. Red and blue guanines are at “syn” and “anti” positions respectively. Black arrowed lines indicate the backbone directions. Four strands are indexed as S1-S4. 5’ and 3’ is the backbone ends. Two yellow triangles indicate the position of the electrode attachment. As shown is an example of S2-5’/S4-3’ attachment.

Table 3.1: The conductance of 6-layer G-tetrads in the middle of junction (see Figure 3.16). The results are averaged from 4000 snapshots, which are extracted from 200 ns MD simulations. Unit is 10^{-7} G_0.

	S2-3’	S3-5’	S4-3’	S1-5’
S2-5’	2.93	5.85	2.89	5.61
S1-3’	5.39	7.67	9.01	11.51

I then look at the whole 3D structure of the G4-duplexes. Since I switch the strand paring of duplexes at the two ends of the junctions (in both Para and Anti junctions), two duplexes at one interface face each other with their major grooves, leaving enough room to accommodate backbones. However, two duplexes at another interface face each other with their minor grooves, where backbones collide and the negative charges on backbones push them apart. In the figures, the minor groove side is put on the top and major groove side is put on the bottom. This major/minor groove difference is supported by the observation in MD simulations that two duplexes at major groove side can stack well with G4 (in both Para and Anti junctions) but duplexes at minor groove side were bent, breaking the stacking (see Figure 3.17b and c).

To investigate the charge transport efficiency at the G4-duplex interfaces, the electronic coupling between two Guanines near the interfaces for Anti-N6-L1-4 and Para-N6-L1-4 in C1 conformation (Figure 3.17a, 3.17b and 3.17c) is calculated, since purines are known to be the dominant mediators of the hole transport[71, 87]. G4 and duplex stack well at the bottom interface (facing with major grooves) and V_{RMS} (root mean square coupling strength in the GG coupling, as indicated by the black arrow in Figure 3.17a) are 0.19 eV and 0.07 eV for Anti-N6-L1-4 and Para-N6-L1-4 respectively, similar to the V_{RMS} between nearest neighbor stacked GG in B-DNA (0.07eV). However, the stacking at the top interface (facing with minor grooves) is broken by backbone collision and G4-duplex geometrical mismatch, complicating the structural and electronic environment. Some hydrogen bonds near the top interface are broken. Therefore the Guanine in duplex can couple with the same strand G in G4 (intra-strand pathway as indicated by the blue arrow in Figure 3.17a), or with the cross strand G in G4 (cross-strand pathway as indicated by the red arrow in Figure 3.17a). For both Anti and Para conformations, the V_{RMS} in these pathways are within the range of 10^{-5}~10^{-3} eV (see values in Figure 3.17b and Figure 3.17c), orders of magnitude smaller than GG couplings in duplexes. Therefore, a much smaller conductance for G4-duplexes comparing to DNA duplex is expected. These results support the experimental findings and the structural analysis above.

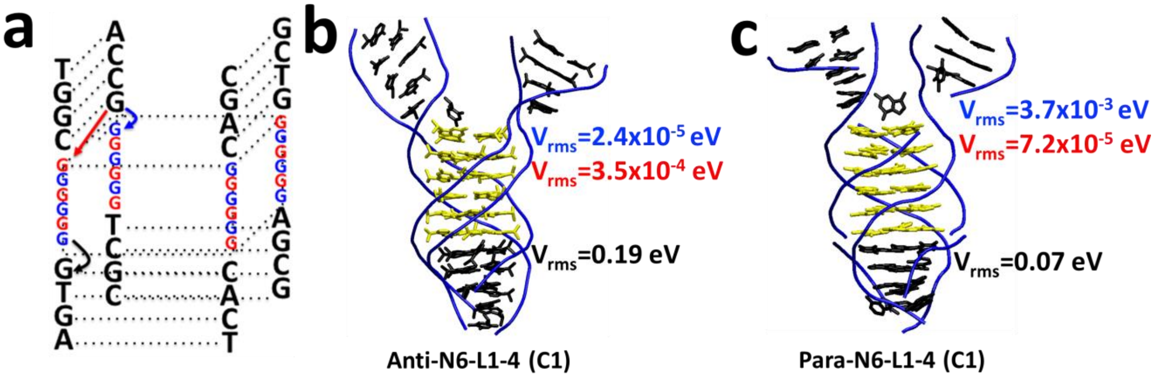

Anti-N6-L1-4 (C1)

Para-N6-L1-4 (C1)

Figure 3.17: Molecular dynamics simulations and coupling strength for non-modified G4-duplex junctions in Anti and Para conformations**. (a).** The sequence of non-modified G4-duplex junctions. The blue arrow and red arrow indicate the intra-strand and cross-strand GG coupling pathways at the top interface. The black arrow indicates the GG coupling pathway at the bottom interface. **(b).** A snapshot of the C1-conformational Anti-

N6-L1-4 extracted from the production MD run. The G4-duplex stacking is broken and some hydrogen bonds around the top interface are disrupted (minor groove side). The hydrogen bonds and stacking remain well at the bottom interface (major groove side). V_{RMS} is averaged from 25 ns MD simulations. The bases in G4 are colored yellow and the bases in duplexes are colored black. Blue lines are the backbones. **(c).** A snapshot of C1-conformational Para-N6-L1-4 extracted from the production MD run. The G4-duplex stacking at the top interface are disrupted (minor groove side). The stacking is well maintained at the bottom interface (major groove side). V_{RMS} is averaged from 20 ns MD simulations.

3.6 Measurements and simulations of modified G4-duplex structures

To recover the base stacking at the top interface and improve the conductance, the G4-duplex structures to obtain the second series of G4-duplex structures are modified. First, the duplex at the top interface that is not involved in the charge transport pathway is removed to solve the backbone repulsion problem (Blue in Figure 3.18a). Second, a 9-atom polyethylene glycol (PEG) linker between G4 and duplex at the top interface is inserted (purple in Figure 3.18a) to release the possible geometrical mismatch. Notice that the sequence in the purple frame (Figure 3.18a) is exchanged to avoid the PEG being involved in the charge transport pathway, i.e. between two Guanines. Finally, the strand 2 with strand 4, and also strand 1 with strand 3 are connected using a T loop consisting of four T bases to stabilize the structure. The second series of G4-duplex structures are shown in Figure 3.18b and corresponding double-stranded DNA is shown in Figure 3.18c.

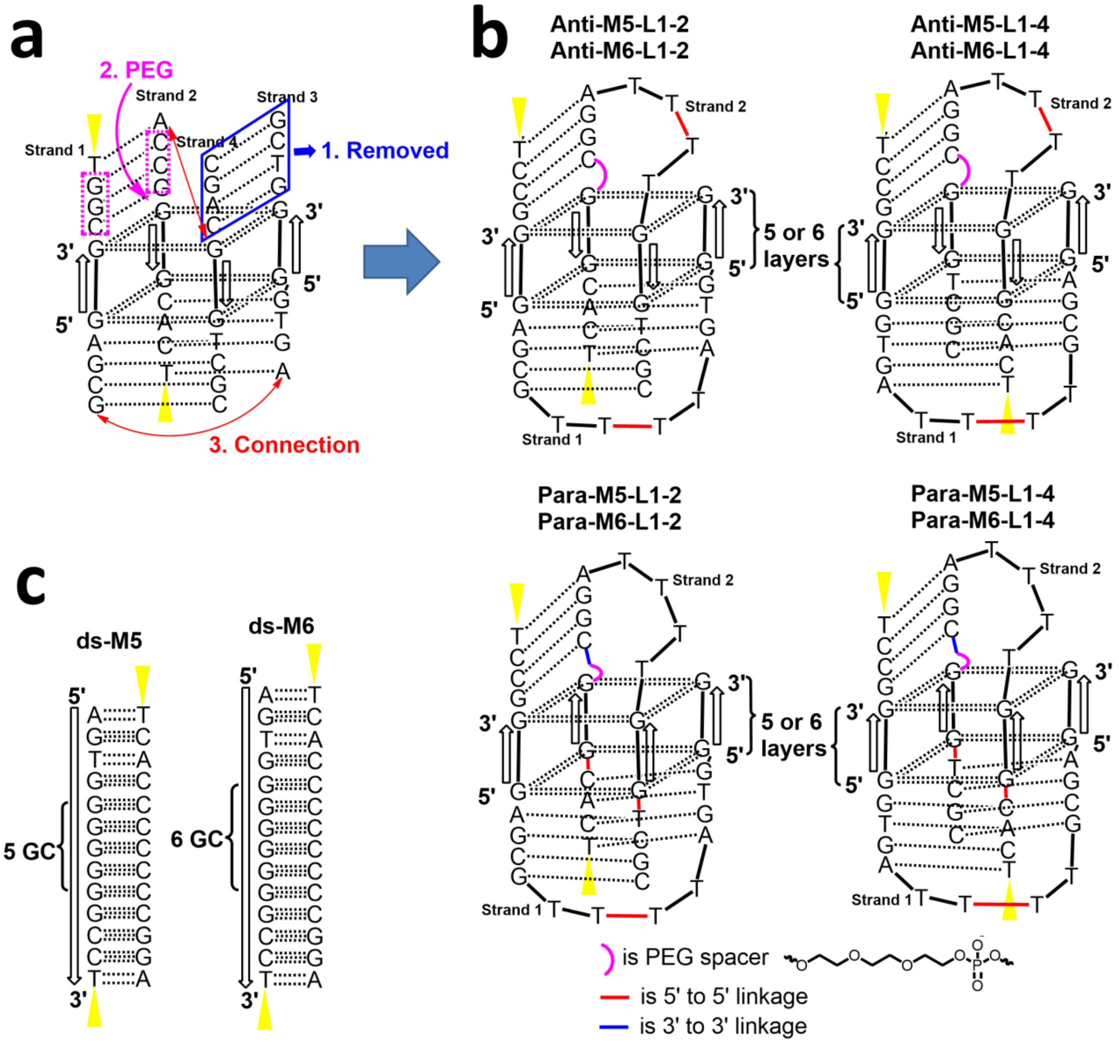

Figure 3.18: The modification, structures and sequence design of modified G4-duplex junctions and the corresponding DNA duplex. **(a).** The modification on the G4-duplex takes three steps. Step 1: Remove one duplex at the top interface (shown in blue); Step 2: Insert a PEG linker at the top interface and exchange parts of the sequence (shown in purple frame); Step 3: Connect strand 2 with strand 4, and strand 1 with strand 3 using T loop consisting of four T bases (shown in red). **(b).** L1-2 (left) and L1-4 (right) G4-duplex with 5 or 6 layers of G4 in Anti (top) and Para (bottom) conformation after the modification. **(c).** New DNA duplex with 5 GC or 6 GC base pairs instead of the G4

layers in the G4-duplex structure. Notice that the sequence changes accordingly with the change in the G4-duplex. Arrows indicate the direction of the backbone from 5’ to 3’. Black dashed lines indicate hydrogen bonds. Gold triangles indicate the binding points of Au electrodes.

I carried out conductance measurements and Figure 3.19a (also see Table 3.2, for conductance histograms see Figure 3.20 to Figure 3.22) shows the conductance of modified Anti conformation (black points), modified Para conformation (red points) and double-stranded DNA (blue points). The charge splitter-like behavior still remains, as one can see the conductance values of L1-2 and L1-4 are nearly the same, regardless of the number of G4 layers and the Anti or Para conformation. Meanwhile, the conductance values of G4-duplex all increase up to the level close to the conductance of duplex with the same sequence, indicating the base stacking at the interface is recovered or at least partially recovered after the modification.

Molecular dynamics simulations and snapshots are shown in Figure 3.19c and Figure 3.19d for Anti-M6-L1-4 and Para-M6-L1-4 respectively. Notice that the stacking at the top interface is recovered by the structural modifications. Coupling calculations between the two G’s at the top interface (intra-strand pathway as indicated by the blue arrow in Figure 3.19b) shows that the V_{rms} is 0.13 eV and 0.09 eV for Anti-M6-L1-4 and Para-M6-L1-4 respectively, similar to the V_{rms} between nearest neighbor stacked guanines in B-DNA (0.07eV). The coupling strength calculations, together with the molecular dynamics simulations, approve that the modification recovers the base stacking at the top interface, thus increasing the conductance value up to 5-fold, and close to that of DNA duplex. Notice that T loops are not included in the MD simulations in Figure

3.19c and Figure 3.19d. Including T loops in the MD simulations does not affect the conclusions (Figure 3.23).

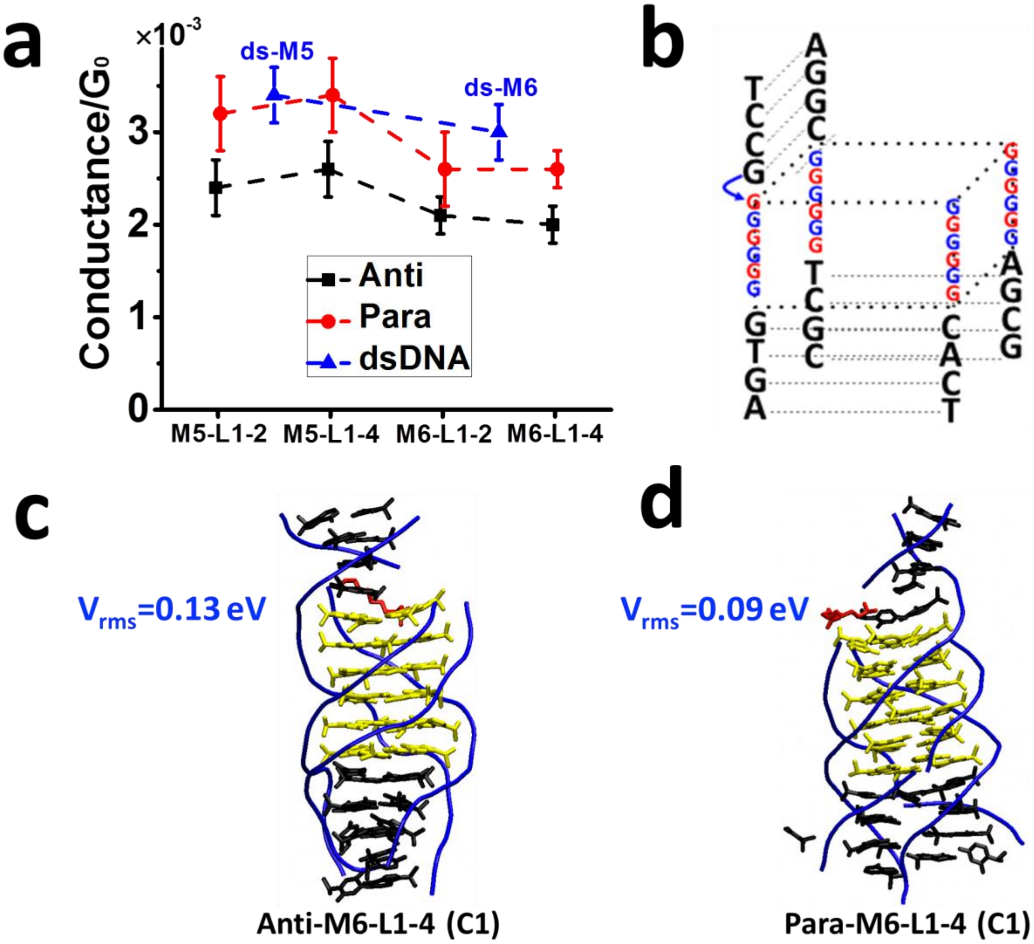

Figure 3.19: Conductance, molecular dynamics simulations and coupling strength calculations for modified G4-duplex junctions in Anti and Para conformation. (**a).** Comparison of the conductance for the modified G4-duplex junctions and the dsDNA. The conductance of all the G4-duplex (red and black points) are all around 2.5×10^{-3} G_0 (see Table 3.2), close to the conductance of dsDNA (blue points) with the same sequence. Error is from the standard deviation of three to seven sets of experiments. **(b).** The sequence of modified G4-duplex (T loops and the PEG linker are not shown). The blue

arrow indicates the intra-strand pathway between the two Guanines at the top interface. GG coupling strength value V_{rms} is shown in Figure 3.19c and 3.19d. **(c).** A snapshot of the C1-conformational Anti-M6-L1-4 extracted from the production MD run. The base stacking and the base paring are maintained at the top interface, in contrast with the broken stacking and hydrogen bonds in Figure 3.17b. V_{RMS} is averaged from 5 ns MD simulations. The bases in G4 are colored yellow while the bases in duplexes are colored black. PEG is colored red. Blue tubes are backbones. **(d).** A snapshot of the C1-conformational Para-M6-L1-4 extracted from the production MD run. V_{RMS} is averaged from 5 ns MD simulations. Base stacking and hydrogen bonds remain well at the top interface, in contrast with the broken ones in Figure 3.17c.

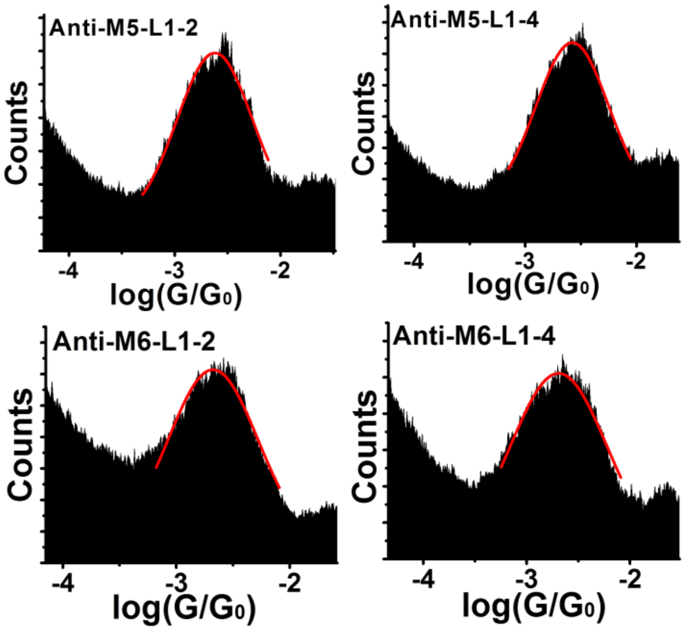

Figure 3.20: Conductance histograms of modified antiparallel G4-duplex.

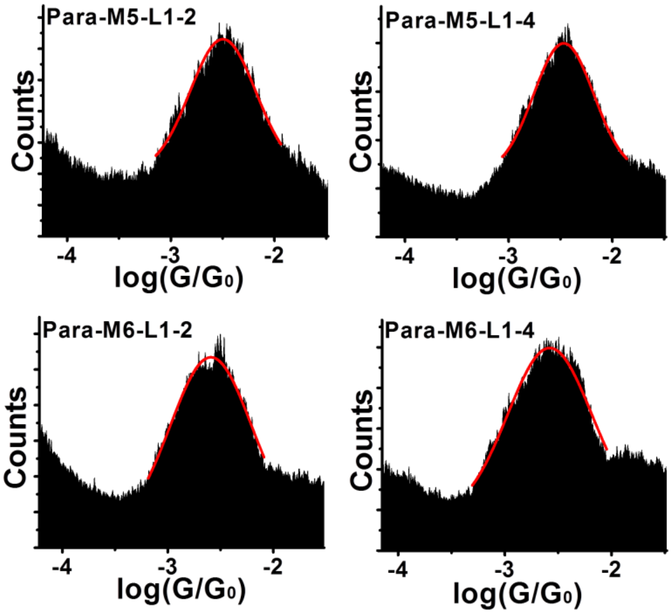

Figure 3.21: Conductance histograms of modified parallel G4-duplex.

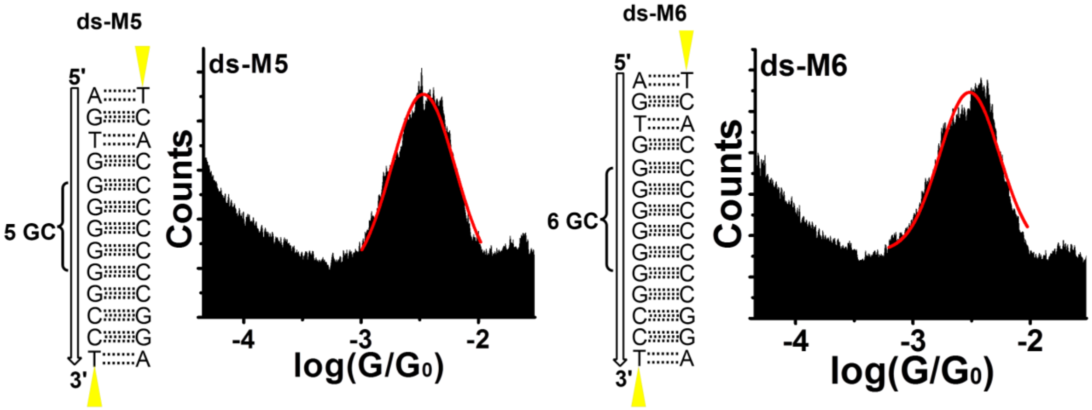

Figure 3.22: Structures and conductance histograms of double-stranded DNA as a comparison for modified G4-duplex.

Table 3.2: Conductance values for all the G4-duplexes and dsDNA**.** Error is from the standard deviation of three to seven sets of experiments.

Non-modified G4-duplex		Modified G4-duplex	
Anti-N5-L1-2	$(4.7 \pm 0.2) \times 10^{-4}\ G_0$	Anti-M5-L1-2	$(2.4 \pm 0.3) \times 10^{-3}\ G_0$
Anti-N5-L1-4	$(4.6 \pm 0.2) \times 10^{-4}\ G_0$	Anti-M5-L1-4	$(2.6 \pm 0.3) \times 10^{-3}\ G_0$
Anti-N6-L1-2	$(5.2 \pm 0.4) \times 10^{-4}\ G_0$	Anti-M6-L1-2	$(2.1 \pm 0.2) \times 10^{-3}\ G_0$
Anti-N6-L1-4	$(4.0 \pm 0.4) \times 10^{-4}\ G_0$	Anti-M6-L1-4	$(2.0 \pm 0.2) \times 10^{-3}\ G_0$
Para-N5-L1-2	$(4.0 \pm 0.2) \times 10^{-4}\ G_0$	Para-M5-L1-2	$(3.2 \pm 0.4) \times 10^{-3}\ G_0$
Para-N5-L1-4	$(4.6 \pm 0.2) \times 10^{-4}\ G_0$	Para-M5-L1-4	$(3.4 \pm 0.4) \times 10^{-3}\ G_0$
Para-N6-L1-2	$(3.7 \pm 0.3) \times 10^{-4}\ G_0$	Para-M6-L1-2	$(2.6 \pm 0.4) \times 10^{-3}\ G_0$
Para-N6-L1-4	$(4.9 \pm 0.2) \times 10^{-4}\ G_0$	Para-M6-L1-4	$(2.6 \pm 0.2) \times 10^{-3}\ G_0$
DNA duplex		DNA duplex	
ds-N5	$(3.3 \pm 0.3) \times 10^{-3}\ G_0$	ds-M5	$(3.4 \pm 0.3) \times 10^{-3}\ G_0$
ds-N6	$(2.8 \pm 0.2) \times 10^{-3}\ G_0$	ds-M6	$(3.0 \pm 0.3) \times 10^{-3}\ G_0$

In self-assembly of these modified G4-duplex junctions, the removed duplex can be in either minor groove side or major groove side. If the removed duplex is on the minor groove side (as in the MD simulations), the modification can effectively remove the backbone collision and obtain well-stacked G4-duplex junctions. However, if the duplex is removed from the major groove side, the two duplex at the minor groove side still cannot stack. Both of the possibilities can coexist in the molecules. Thermodynamics may favor the well-stacked G4-duplex junctions because stacking lowers the free energy.

To verify the necessity of the PEG linker, the Anti-M6-L1-2 and Para-M6-L1-4 without the PEG linker is simulated. Notice that in the Anti conformation G4 without PEG linker, the base paring in the duplex (attached to the short side) breaks and form a zip-like structure. In Para conformation without the PEG linker, the duplex on the top interface can stack but the stacking distance is much longer than that in B-DNA. One expect these will cause a decrease in the coupling strength between the two G's at the interface, thus lowering the conductance. Meanwhile, the two T loops are also necessary to keep the whole G4-duplex stable, as one do not get stable G4-duplex structures when removing the two T loops (Figure 3.24). To study the effect of the two T loops on the structure, molecular dynamics simulation on the G4-duplex structures with the two T loops is performed (Figure 3.23). Comparing to the G4-duplex structure without the two T loops, No obvious changes in the base stacking at the interface were seen, thus the two T loops will have limited impact on the charge transport. This is reasonable because the T loops are not involved in the charge transport pathway. The result is also confirmed by the conductance measurements for another type of T loop modification that only connects the strand 3 with 4 (Figure 3.25), as no obvious changes in the conductance in this new type of T loop modification were seen.

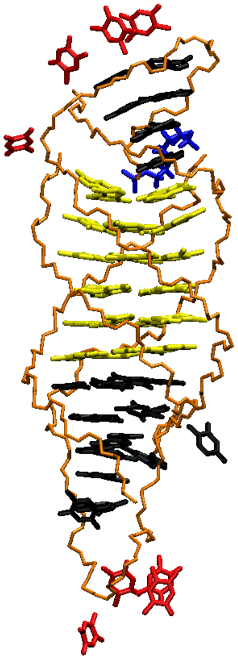

Figure 3.23: A snapshot of Anti-M6-L1-2 (C2 conformation) with T loops**.** One duplex at the top is removed. A 9-atom PEG linker (colored blue) is added at the G4-duplex interface to bridge the geometric mismatch between G4 and duplex. Thymine loops (colored red) are employed to connect the diagonal backbones. Bases in G4 are colored yellow and bases in duplexes are colored black.

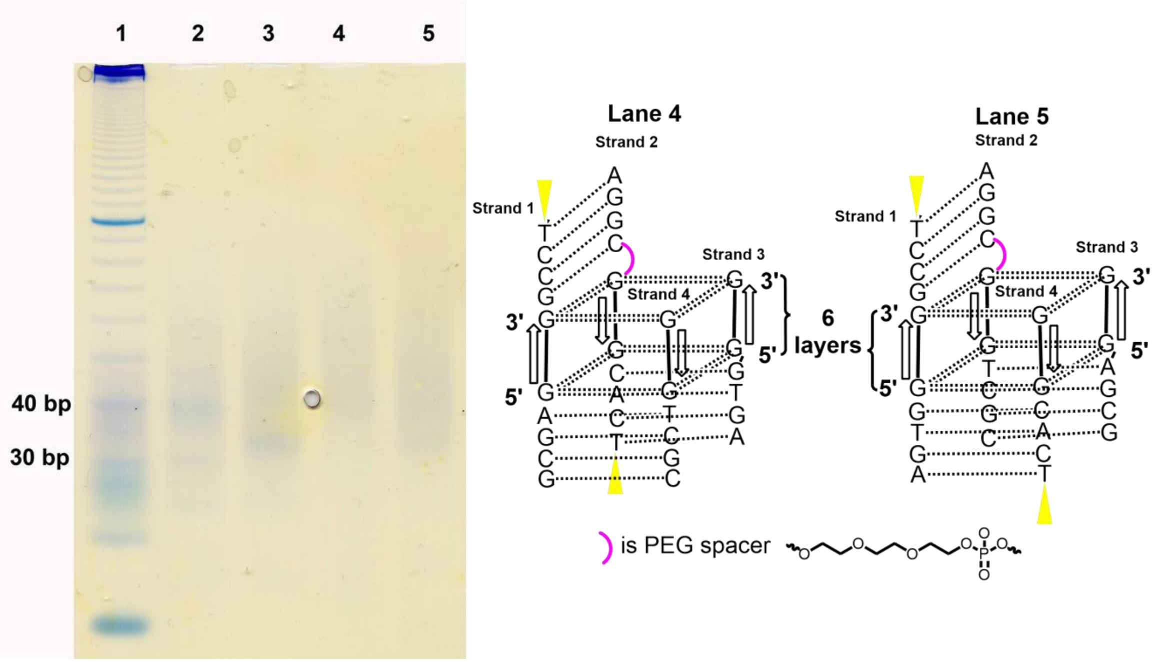

Figure 3.24: Gel electrophoresis of modified G4-duplex without T loops in Anti conformation. 10% native PAGE was run at 20 ℃ in 100 mM Na_2HPO_4, 100 mM KH_2PO_4, 10 mM Mg Acetate, pH ~7.5. Lane 1 contains the DNA molecular weight marker. Lane 2 and lane 3 are other designs with unstable G4-duplex structures which are not used in this work. Lane 4 and lane 5 contains the G4-duplex without the two T loops. Their structures are shown on the right. The smear bands indicate their structures are not stable at 20 ℃. Therefore the two T loops are necessary to stabilize the G4-duplex structure.

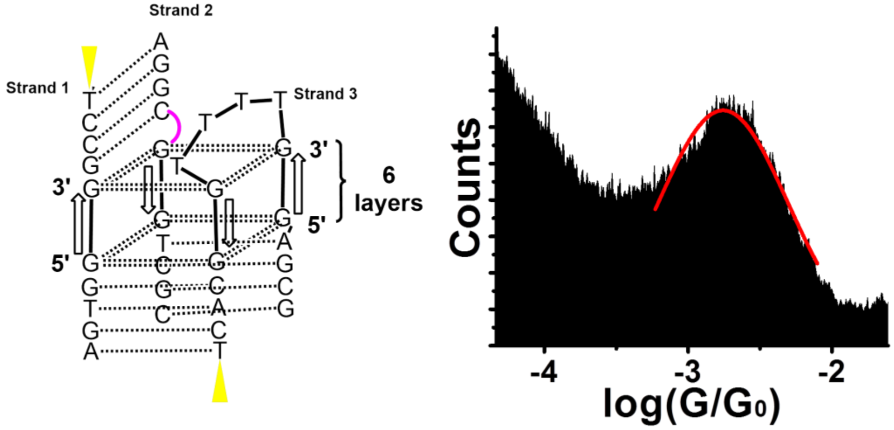

Figure 3.25: Structures and conductance histograms of modified G4-duplex with new type of T loop connecting strand 3&4. The conductance is similar to the modified G4-duplex with two T loops, indicating the T loops do not have significant impact on the charge transport.

3.7 Conclusions and perspectives.

In this chapter, I demonstrated a single molecular junction based on extending Guanine quadruplex structure with duplexes (G4-duplex) that behaves like a charge splitter. Charge injected into one duplex on the top will come out from another two different duplexes on the bottom with nearly the same transport efficiency. Two series of G4-duplex were studied. The first series of G4-duplex structures have a much lower conductance value than that of DNA duplex. Molecular dynamics simulation and coupling strength calculations confirmed this is due to the weak base stacking at the interface between the G4 and duplex. By removing one duplex on the top and adding a PEG linker at the interface, the second series of G4-duplex that has almost the same conductance value with DNA duplex. Molecular dynamics simulation and coupling strength confirmed the recovery of the base stacking at the interface after the modification. The work successfully constructed a three-terminal single molecular charge splitter based on DNA G-quadruplex with high transport efficiency, which will provide useful insights towards building up complicated network-like electronic devices.

Most of previous study on DNA charge transport only focus on 1D structures with two terminals including dsDNA or DNA G-quadruplex[60, 63, 87, 104, 112]. From electric circuit point of view, using a two-terminal structure can only build up a linear structure. To construct a network structure, at least a three-terminal structure is highly desired, and this can be realized via the G4-duplex structure (Figure 3.26a). Constructing a network-like structure based on DNA will provides useful insights into building up electronic circuits with arbitrary shape and size. On the other hand, G-quadruplex plays an important role in biological system. The formation of G-quadruplexes in telomeres can decrease the activity of the telomerase, an enzyme that is responsible for regulating the length of telomeres and involved in around 85% diseases of cancer. Using the G4-duplex junction constructed in this chapter to study the interactions between the enzyme and the G-quadruplex may also have some significant impacts on oncology (Figure 3.26b).

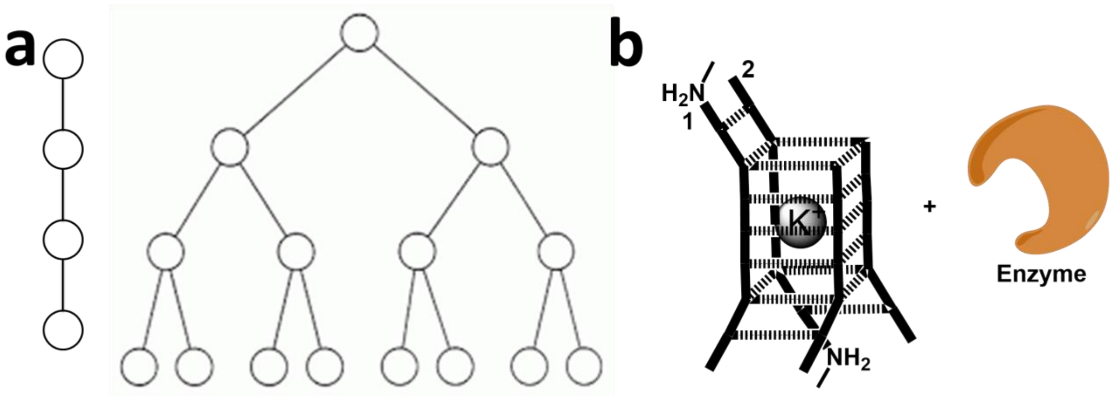

Figure 3.26: Prospective for G4-duplex study in this chapter. (a). A linear structure compared with a tree structure. To construct a network-like structure, at least three

terminals are needed. (b). G-quadruplex can interact with an enzyme, which could induce some changes in the charge transport properties.

CHAPTER 4

GATE-CONTROLLED CONDUCTANCE SWITCHING IN DNA

The work in this chapter is contributed by my collaborators Julio L. Palma, Yueqi Li, Vladimiro Mujica, Mark A. Ratner, Nongjian Tao and me.

4.1 Introductions

An ultimate goal in the field of molecular electronics is to build up electronic device on molecular level[2, 23, 29]. To date, a number of molecular devices with different functionalities such as diodes[30-33], transistors[34-36, 113] and switches[37-41, 43, 44, 114-116] have been demonstrated to mimic the traditional electronic components in circuits. Among them, precisely controlled conductance switching between two discrete states on a single molecular level has been achieved by an external stimulus such as light[40, 117], force[39, 41] and bias voltage[115, 118]. For example, He et al. reported the conductance switching behavior of a diarylethene derivative based molecular junction under UV light[40]. Under the UV light, the molecule will undergo a ring-close reaction to form a larger conjugated structure through the whole backbone of the molecule, thus giving a higher conductance value. The reversible reaction (ring-open reaction) can occur when Vis light is given (Figure 4.1a). Moreno-García et al. reported a force-induced conductance switching behavior based on a molecular junction with C_{60} as the terminated group[39]. Two distinct conductance states were observed during the approaching/retracting process of the STM tip. The two states are attributed to the electron tunneling through one C_{60} terminated group and the fully extended molecule, respectively (Figure 4.1b). Although the conductance switching can be realized by many different ways of stimulus, this kind of precisely controlled conductance switching is hard to be achieved by electrochemical gate control. That is because the conductance of molecule-mediated junctions will usually change continuously by tuning molecular orbital levels with respect to the Fermi level of the electrodes[36, 54, 59]. Moreover, there is a lack of kinetics study on the switching behavior under an external stimulus. Developing single molecular switches requires a systematic study and precisely controlled of single molecular conductance switching behavior.

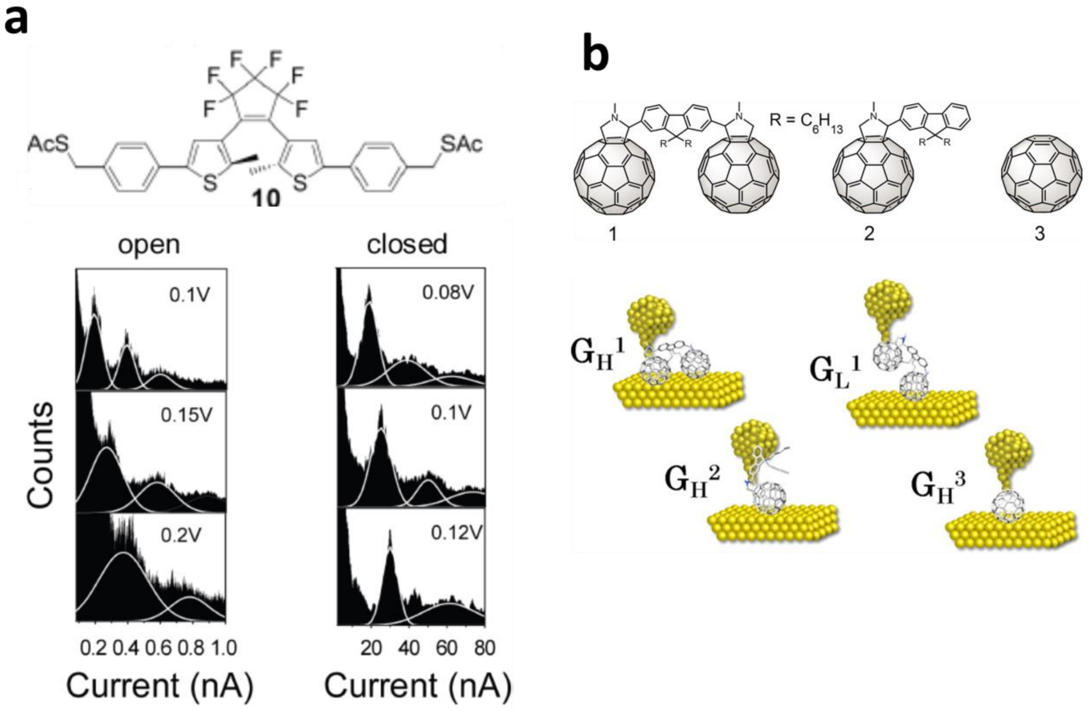

Figure 4.1: Conductance switching behavior induced by light and force. (a) A diarylethene derivative based molecular junction can be reversibly switched by UV light and Vis light, thus giving a higher conductance and low conductance respectively. Reprinted with permission from ref. [40]. (b) A molecular junction with C_{60} terminated group exhibits two different conductance states during the approaching/retracing process

of the STM tip, which is due to two different transport pathways. One is through a single C_{60} group. The other is through the whole extended molecule. Reprinted with permission from ref. [[39]].

DNA is a unique molecule because not only its role in living systems, but also its double helical structure with π-electron stacking of the base pairs that has inspired many to explore DNA as a molecular wire[60, 62, 69, 78, 81-84, 87]. In addition, recent advances have made it possible to design and synthesize DNA with programmable 3D nanostructures[80], which have further stimulated efforts to study DNA as intriguing device building blocks. Extensive theoretical and experimental works have indeed established that long-range charge transport can occur along double helical DNA[62, 71, 73, 78, 79]. However, for an active electronic component, one wishes to switch DNA conductance between different states, which has not yet been demonstrated.

In this chapter a molecular switch by replacing a DNA base in double helical DNA with a redox group will be presented. By controlling the electrochemical gate voltage, I reversibly switch the DNA conductance between two discrete levels via the redox group. The population of the reduced and oxidized states follows the Nernst Equation, and analysis of the conductance switching allows determination of the rate constants of the redox process at the single molecule level. Theoretical calculation shows that the conductance switching arises from a change in the molecular energy alignment associated with the redox state switching.

4.2 Methods

Anthraquinone modified oligonucleotide was purchased from Alpha DNA (HPLC purified). All the other oligonucleotides were purchased from Integrated DNA Technologies (HPLC purified). One of the oligonucleotides (Figure 4.2) was modified with 3'-thiol C3 S-S and 5'-thiol C6 S-S in its protected form. The oligonucleotides were dissolved in 18.4 MΩ·cm deionized (DI) water to reach a concentration of 100 μM and stored at -20 °C. Sodium cacodylate trihydrate (≥ 98%), magnesium perchlorate (ACS reagent, and ≥ 98%) and cacodylic acid (≥98%) were purchased from SIGMA-Aldrich, and sodium perchlorate monohydrate (for HPLC, ≥99.0%) was purchased from Fluka. All the reagents were used without further purification. Multigene Mini Thermal Cycler (Model: TC-050-18) was used to anneal DNA solution samples. Cacodylate buffer (pH = 7.0) was prepared by dissolving 21.4 mg sodium cacodylate trihydrate, 22.3 mg magnesium perchlorate, 196.6 mg Sodium perchlorate monohydrate and 2 mg cacodylic acid in 10 mL18.4 MΩ·cm DI water. The oligonucleotide with thiolate linkers was deprotected with dithiothreitol (DTT) solution for 1 hour, then transferred to a spin column (Roche Applied Science quick spin column sephadex G-25) and centrifuged to remove DTT and the protection group. The oligonucleotide was then mixed with the complementary strand with a stoichiometric ratio of 1:1 (calibrated by absorption intensity at 260 nm) and annealed by varying temperature from 80 ℃ to 8 ℃ at the rate of 4 min/℃, and then kept at 4 ℃ prior to measurements.

Gold substrates were prepared by thermally evaporating ~160 nm of gold (99.999% purity, Alfa Aesar) onto freshly cleaved mica slides and annealed in ultra-high vacuum (10^{-8} torr) for 3 hours. Before each experiment, the gold substrate was flame annealed for 1 min with a hydrogen flame. The STM tip was freshly cut from gold wire (99.95%

purity, Alfa Aesar) and coated with Apiezon wax to reduce the leakage current directly through aqueous solution.

All measurements were carried out in cacodylate buffer at room temperature (22 ℃). A small bias voltage was applied between the tip and substrate (5 mV, otherwise stated). As a control the STM break junction measurement was initially performed without DNA in cacodylate buffer, and the measured conductance histogram was found to featureless. Then 50 uL 5 uM double strand DNA was added to the buffer. A large number of current–distance traces (~4,000) were recorded for each experiment, from which the conductance histogram was constructed with an algorithm described elsewhere[110]. To minimize noise, the algorithm counted only the traces showing counts exceeding a preset threshold in the histograms. For each double strand DNA, the measurement was repeated three times to estimate the experimental error. The electrochemical gate controlled measurements were performed under nitrogen atmosphere and the cacodylate buffer was purged by nitrogen (99.99% purity) for 30 min before use. The gate voltage was controlled by a biopotentiostat (Agilent). DNA was immobilized on the gold substrate by exposing the substrate in 10 uM DNA solution for 1 hour, followed by rinsing with cacodylate buffer to remove non-bound DNA, and then filled with the buffer.

Cyclic voltammetry was performed on the DNA modified gold substrate with a platinum wire as the counter electrode, a Ag/AgCl (in 1M KCl solution) as reference electrode using an Autolab potentiostat. Ten repeated potential cycles of cyclic voltammograms were obtained for each sample with a typical sweeping rate of 100 mV/s (or otherwise stated. In addition to characterizing Aq-DNA immobilized on the gold substrate, cyclic voltammetry was performed before and after each STM break junction experiment to check the stability of the silver quasi reference electrode, and the difference in the redox potential of Aq-DNA was taken as the error in the gate voltages.

Quantum chemical calculations to obtain energy and electronic couplings of the hopping sites were performed using molecular fragments, G-Aq-G:C and G-H_2Aq-G:C. The systems were set up based on the canonical B-DNA structure and the 2KK5 of the Protein Data Bank (PDB), which is conformed by a similar structure than this one with a terminal purine DNA base followed by an anthraquinone[119]. The Hamiltonian is from a ZINDO/S calculation and divided it into their segments, which represent the hopping sites (G and Aq/H_2Aq). The energy and electronic coupling is obtained using the HOMO wave function of the Guanine and the neighbor occupied orbitals of the Aq/H_2Aq. These energy levels have been widely used as a reasonable approximation of the adiabatic wave function for the charge donor and acceptor[120].

4.3 Structure and characterization of modified DNA

To switch DNA conductance, I replaced one of the regular DNA bases with anthraquinone (Aq), a redox group that can be reversibly oxidized and reduced (Figure 4.2a). NMR and molecular dynamics analysis of a similar structure suggest that the Aq moiety stacks on the adjacent GC base pair, and the non-paired Guanine ring rests atop the Aq ring (Figure 4.2b)[119]. This conformation is highly stable as indicated by the melting temperature increasing effect after this modification[119, 121]. As a control experiment I also studied DNA without the Aq moiety (Figure 4.2c). I refer the redox modified DNA as Aq-DNA, and unmodified DNA as u-DNA.

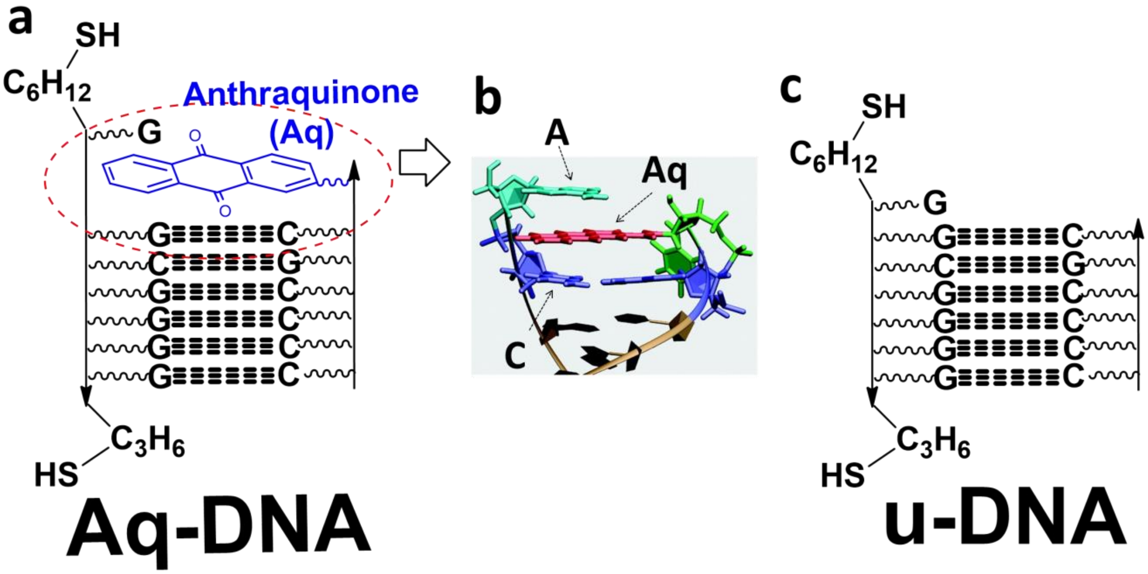

Figure 4.2: Structure of Aq-DNA and u-DNA studied in this chapter. (a) Structure of Aq-DNA. One of the base was replaced with anthraquinone. (b) 3D structure of a similar DNA structure with Aq intercalating between a non-paired Adenine and paired Cytosine base by NMR study. Reprinted with permission from ref. [119]. (c) Structure of u-DNA without the modification as the control experiment.

I first characterize the DNA samples via gel electrophoresis, UV-Vis spectroscopy, Circular Dichroism and melting temperature study**.** The electrophoretic measurement was performed at 200 V, and 22 ℃ for 2.5 hrs using 50 pmol of each sample and with 8% nondenaturing PAGE gels in 1×TAE Mg^{2+} buffer. The gels were subsequently stained with ethidium bromide (EB) and scanned in a Biorad Gel Doc XR+ system for sample visualization. The DNA samples were annealed by ramping the temperature from 80 ℃ to 8 ℃ within 4 hours at the rate of one Celsius degree per 4 minutes, and then kept at 4 ℃. Only a single band was observed for each of the sequences (Figure 4.3).

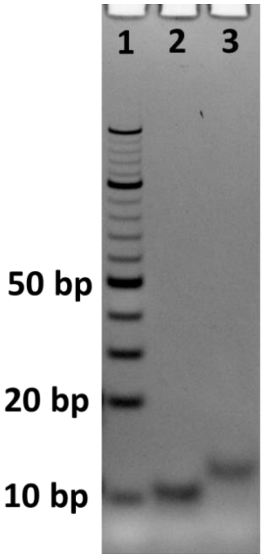

Figure 4.3: Gel electrophoresis of G-DNA and u-DNA. Column 2 is u-DNA. Column 3 is Aq-NDA. Longer DNA sequences have slower mobility as indicated by column 1 for the DNA ladder sample (DNA mixture consisting of 10 bp-200 bp dsDNA in 10bp intervals, also referred to as DNA ruler). Aq-DNA has a slight slower mobility than u-DNA, due to the extra Aq moiety.

UV-Vis absorption spectra were collected on a Varian Cary 300 Bio UV spectrophotometer at room temperature. Both have strong absorption at 260 nm, which is a typical absorption peak for DNA. The Aq-DNA has a weak absorption at around 340 nm, due to the anthraquinone n to π* transition absorption (Figure 4.4). The UV-Vis spectra confirmed the anthraquinone was successfully introduced into the DNA.

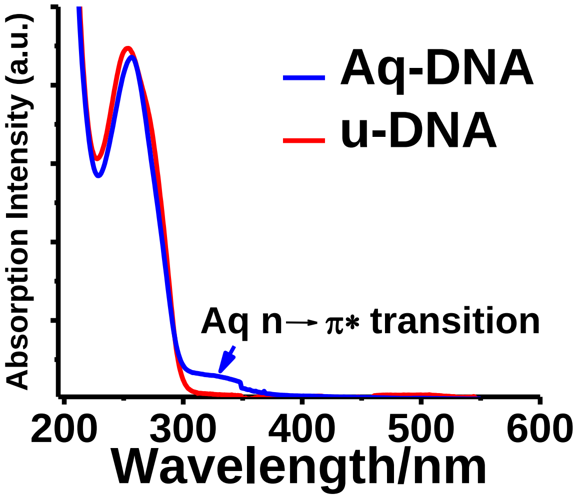

Figure 4.4: UV-Vis absorption spectra for Aq-DNA and u-DNA.

Melting temperature experiments were performed in a Varian Cary 300 Bio UV spectrophotometer with a Peltier thermal controller to determine melting temperature. 10 uM dsDNA were prepared with cacodylate buffer and annealed as for STM-BJ measurements, then heated at a rate of 0.2℃/min from 20℃ to 80℃ with the absorbance at 260 nm recorded in 60s intervals. Melting temperature was obtained by fitting the melting temperature curves to a two state thermodynamic model (Figure 4.5). The melting temperature of G-DNA (44 ^{o}C) is much higher than that of u-DNA (32 ^{o}C), indicating that the intercalation of Aq stabilizes the ending base pairs[119, 121].

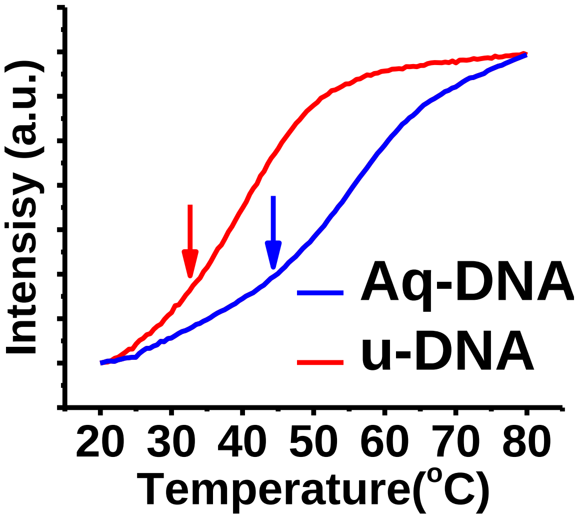

Figure 4.5: Melting temperature study via UV-Vis absorption for G-DNA and u-DNA.

Circular dichroism spectra were collected on a Jasco (Easton, MD) J-815 Spectropolarimeter from 320 nm to 220 nm with a scanning rate of 50 nm/min. The spectra were compiled by averaging the results from 5 scans, taken in cadodylate buffer solution at room temperature to replicate the environment during STM break junction experiments. The negative band at 245 nm, and positive band at around 265 nm indicates B-form structure for both Aq-DNA and u-DNA (Figure 4.6).

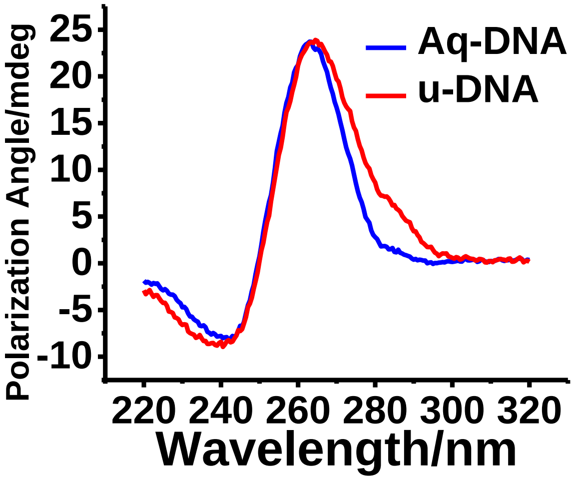

Figure 4.6: Circular dichroism study of Aq-DNA and u-DNA.

4.4 Electrochemistry study of Aq-DNA modified Au substrate

To switch the DNA conductance, I controlled the redox state of Aq-DNA by inserting a silver electrode into the solution (Figure 4.7a)[122, 123]. The silver electrode serves as an electrochemical gate, and the tip and substrate serve as source and drain electrodes. The gate voltage and the source-drain bias were controlled using the standard four-electrode electrochemical configuration with a platinum coil as an auxiliary electrode (not shown in Figure 4.7a) in addition to the tip, substrate and silver quasi-reference electrodes. I first characterized redox-switching properties of Aq-DNA immobilized on the gold substrate with cyclic voltammetry, a widely used electrochemical technique that measures electrochemical current while linearly sweeping the substrate potential back and forth. The measured cyclic voltammograms show a peak in the forward potential sweep, and a negative peak in the reverse potential sweep (Figure 4.7b), corresponding to reversible oxidation and reduction of the Aq group in Aq-DNA (Figure 4.7c). The redox potential of Aq-DNA, determined by taking the average of the oxidation and reduction peak potentials, is -0.46 V vs. Ag/AgCl reference. This finding is consistent with that reported for other anthraquinone DNA intercalation complexes[124, 125]. The separation between the oxidation and reduction peaks increases with potential sweeping rate (Figure 4.7d), and the peak magnitudes increase linearly with the sweep rate (Figure 4.7e), indicating that the Aq-DNA was immobilized on the gold substrate. From the areas of the oxidation and reduction peaks, I determined the Aq-DNA surface coverage to be 1.48±0.03 pmol/cm^2, a typical value for thiolate modified DNA molecules on gold electrodes[67].

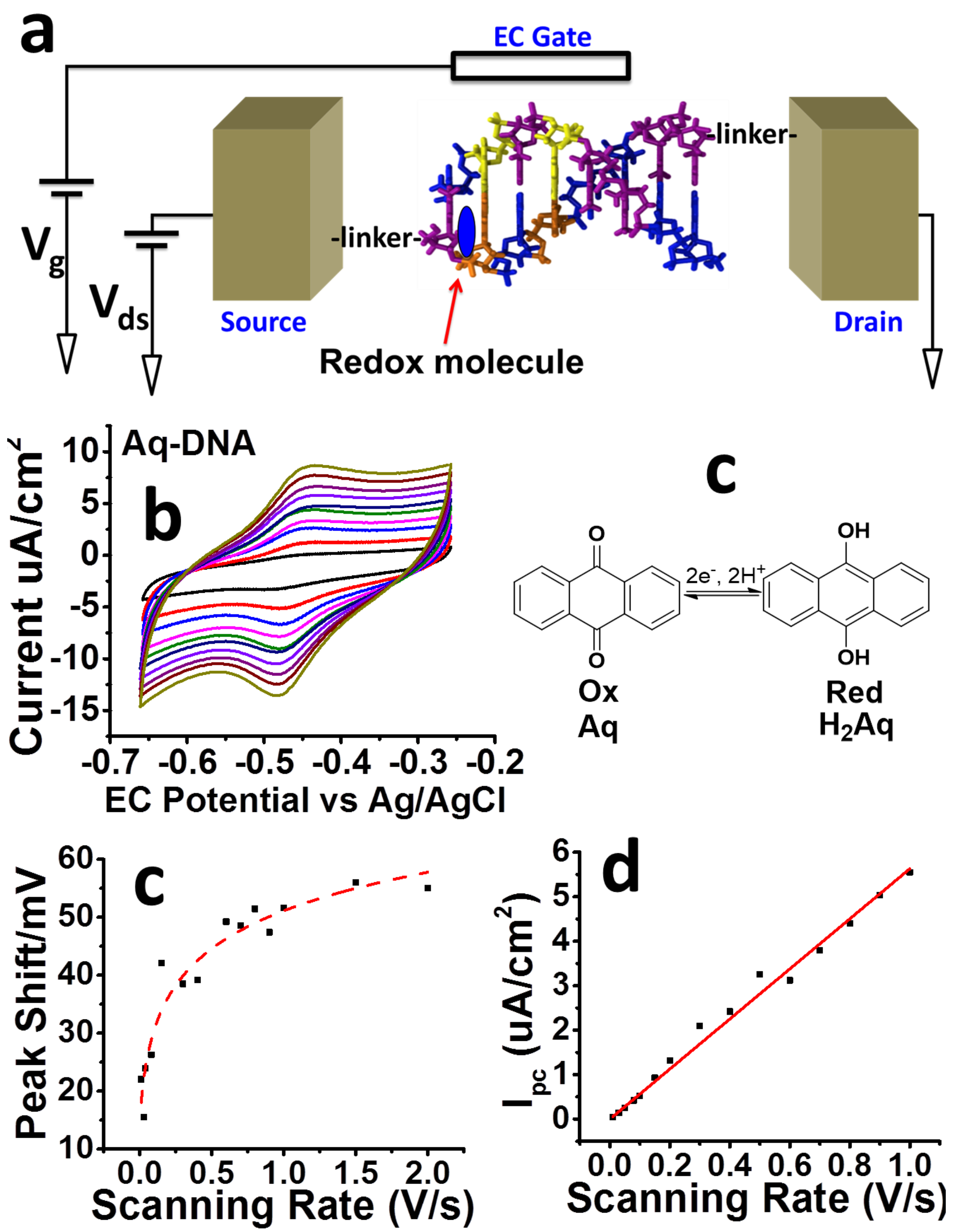

Figure 4.7: Electrochemical characterization of Aq-DNA modified on Au substrate. (a) Illustration of the experiment, where the source and drain electrodes are the STM tip and

substrate, and EC gate is a silver electrode inserted in the solution. A DNA molecule modified with a redox group bridged between the source and drain electrodes via the thiolate linker groups. The source-drain bias (V_{ds}), and the EC gate voltage (V_g) are controlled independently. (b) Cyclic voltammograms of Aq-DNA immobilized on gold substrate with potential sweeping rate varying from 0.01 (black line) to 0.1 V/s (green line) showing oxidation and reduction peaks. (c) Reversible redox reaction of the anthraquinone moiety involving two electrons in aqueous solution. (d) Separation between the oxidation and reduction peaks) vs. potential sweeping rate. (e) The cathodic peak current I_{pc} versus potential sweeping rate. The linear relation confirms that the redox peaks were due surface bound Aq-DNA molecules.

4.5 Conductance histogram when EC gate voltage is off

I measured the DNA conductance using an Scanning Tunneling Microscope (STM) break junction technique[12]. The technique used a gold tip coated with wax to minimize ionic conduction, and a gold substrate. The tip was repeatedly brought into and pulled out of contact with the substrate in a buffer solution containing the DNA molecules, during which the current between the tip and substrate was continuously monitored. Individual current vs. tip-substrate distance traces were recorded during the pulling process (Figure 4.8a) and a plateau in the current traces signaled the formation of a single gold-DNA-gold molecular junction[104]. Thousands of the current traces were collected, and used to construct a conductance histogram, where the peak position indicates the most probable conductance value of the DNA molecules.

I first measured the conductance of both Aq-DNA and u-DNA without applying electrochemical gate voltage, and found that the conductance values for Aq-DNA and u-DNA were $4.0 \pm 0.2 \times 10^{-4}$ G_0 and $1.4 \pm 0.1 \times 10^{-3}$ G_0, respectively, where $G_0 = 7.748 \times 10^{-5}$ S, which is the conductance quantum (Figure 4.8c). Control experiments in the buffer solution without DNA molecules (Figure 4.8b), and with single stranded DNA terminated with two thiolate linkers did not reveal peaks in the conductance histogram. The observed conductance difference between Aq-DNA and u-DNA indicates that the Aq moiety was intercalated into the base pairs in DNA, as shown in literature[119] (Figure 4.2b).

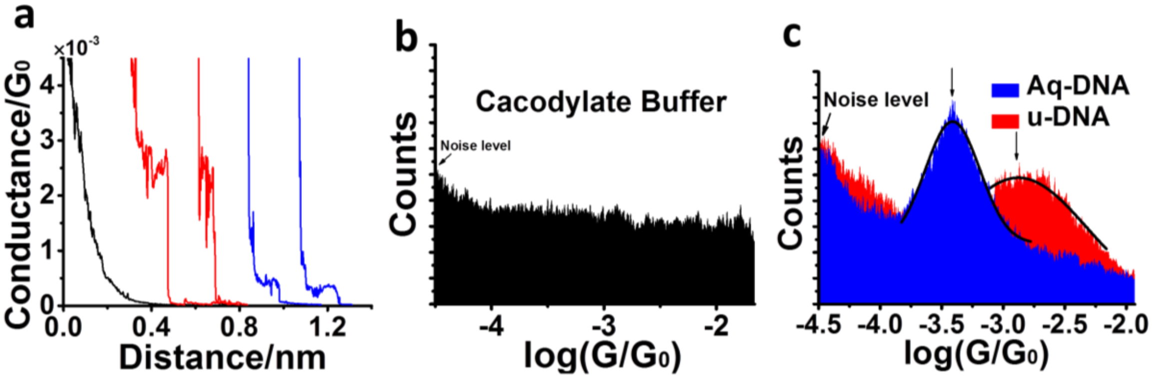

Figure 4.8: Conductance histogram when EC gate voltage is off. (a) Representative current–distance traces (current converted to conductance) of Aq-DNA (blue) and u-DNA (red) in aqueous solution, showing plateaus originated from the formation of the DNA junctions. Control experiments performed in the absence of DNA molecules showing smooth exponential decay (black trace). (b) Conductance measurements in cacodylate buffer. No peaks in the conductance histogram detected within the conductance range, ruling out the possibility of solvent-based molecular junction formation. The noise level is due to the lower limit of the current amplified in the STM scanner. (c) Conductance histograms of Aq-DNA (in blue) and u-DNA (in red), showing

the difference in the conductance peaks. The peak was fitted with a Gaussian distribution and the peak position was taken as the conductance.

To examine the reproducibility of the conductance measurements in the conductance measurements when electrochemical gate voltage was off, the experiments for u-DNA and Aq-DNA were repeated three times, each consisting of ~3000 curves. The results were also listed in Table 4.1, showing the reproducibility of the conductance measurements. The experimental error was calculated by: $\sigma = \sqrt{\frac{1}{N}\sum_{i=1}^{N}\left(x_i - \mu\right)^2}$, where N is the number of sets, x_i is the peak position in each individual set of experiment (on a logarithm scale) and μ is the peak position obtained by compiling all the 3 histograms. I used the fitting errors (Gaussian fitting) in each of the histograms at different gate voltages as the experimental errors[126]. The broad distribution (the width in the Gaussian fit) in the conductance histogram is not measurement error, rather than an inherent property of single molecule measurement originated from the variation in the molecule-electrode contact coupling, and dependence of the conductance on the couplings[127, 128].

Table 4.1: Experimental errors for conductance measurements when EC gate voltage is off.

	1st time	2nd time	3rd time	Result
Aq-DNA	-3.41	-3.41	-3.39	-3.40 ±0.01
u-DNA	-2.82	-2.83	-2.87	-2.85 ±0.02

4.6 Conductance histogram when EC gate voltage is on

In the electrochemical gate controlled conductance measurement, the use of silver quasi reference electrode introduced variations in the actual applied gate voltages. To study the variations, I recorded the cyclic voltammograms for Aq-DNA modified Au surface for 3 hours (all the conductance measurements on the Au surface can be finished within 3 hours) in 10 minutes intervals. In Figure 4.9 I found the redox potential of Aq-DNA shifted to the positive direction with time, from which I concluded that the reference potential shifted to the negative direction. This phenomenon is robust as one can see from the cyclic voltammograms before and after the EC-STM break junction conductance measurements. Hence, I used the differences in the redox potential as the errors in the gate voltages (V_g).

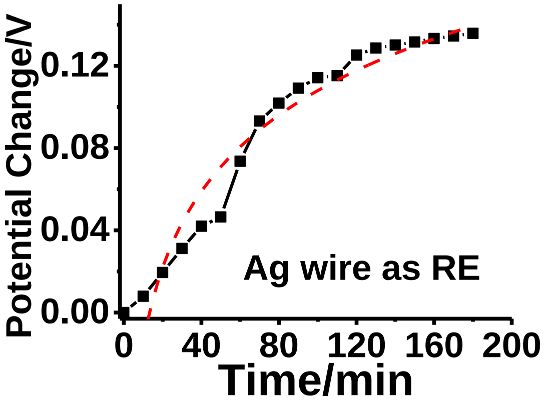

Figure 4.9: Plot of the redox potential changes vs. time, where the red line is a guide to eyes.

After characterizing the conductance and redox property of Aq-DNA, I studied conductance switching of Aq-DNA by controlling the gate voltage. For simplicity, I quoted the gate voltage with respect to the redox potential of Aq-DNA, at which the chances of oxidation and reduction are equal. At each gate voltage, I performed repeated

STM break junction measurement, and constructed a conductance histogram from thousands of individual conductance traces. When the gate voltage is well above 0 V, most Aq-DNA molecules are in the oxidized state and the conductance histogram shows a peak at 3.6×10^{-4} G_0, which is the conductance of Aq-DNA in the oxidized state (top, Figure 4.10). Lowering the gate voltage towards 0 V, a second peak at a higher conductance value (3.0×10^{-3} G_0) appears. I attribute the high conductance peak to Aq-DNA in the reduced state. The high conductance peak increases in height while the low conductance peak decreases in height with decreasing the gate voltage, which is expected as increasing number of Aq-DNA became reduced. The high and low conductance peaks reach a similar height when the gate voltage ~0 V, corresponding to an equal number of Aq-DNA in the reduced and oxidized states (middle, Figure 4.10). Further decreasing the gate voltage below 0 V, the high conductance continues to increase while the low conductance peak decreases and eventually disappears as all the molecules becomes reduced (bottom, Figure 4.10).

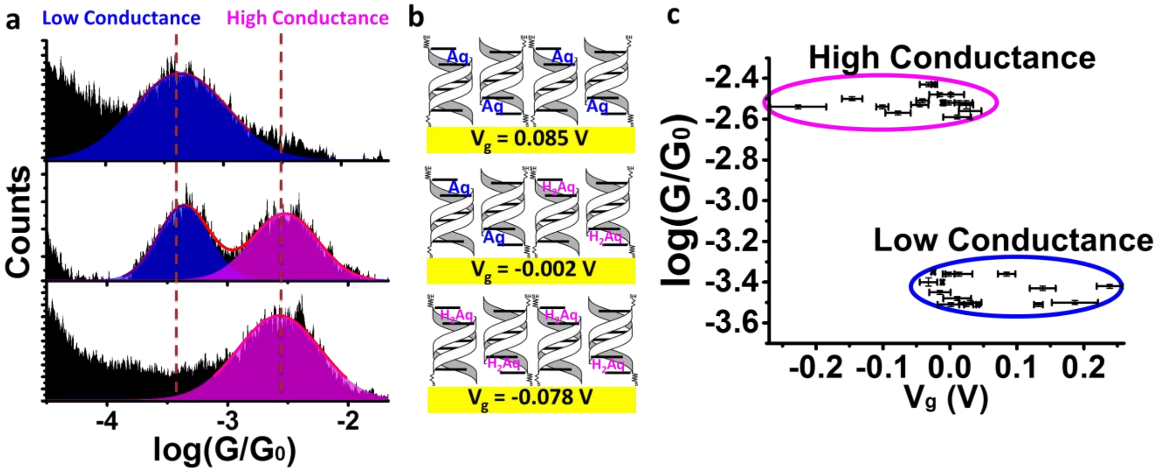

Figure 4.10: Two discrete conductance states of Aq-DNA and their dependence on electrochemical gate voltage. **(a)** Conductance histograms of Aq-DNA with the gate voltage set above (0.085 V), at (-0.002 V) and below (-0.078 V) the redox potential, where the red curves are Gaussian fits to the conductance peaks. **(b)** Populations of Aq-DNA in the oxidized (Aq) and reduced (H_2Aq) states at the corresponding gate voltages. **(c)** Conductance values at different gate voltages showing two discrete conductance states, high (circled with magenta line) and low (circled with blue line) conductance states.

The experiment described above shows that one could switch the DNA conductance between two levels by controlling the Aq redox state. Aq-DNA in the reduced state is nearly an order of magnitude more conductive than that in the oxidized state. Another interesting observation shown in Figure 4.10a is that despite the sensitive dependence of the peak heights in the conductance histograms with the gate voltage, the peak positions change little with the gate voltage. This observation indicates that the conductance of the oxidized and reduced Aq-DNA take two discrete values, and the gate voltage can only switch the conductance between the two values. The switching of conductance between two discrete levels is more clearly shown in the plot of conductance vs. gate voltages in Figure 4.11a. Previous studies of redox molecules typically show continuous changes of conductance with the gate voltage[36, 59, 129]. I will return to the mechanism of this discrete conductance switching in Aq-DNA later.

To confirm that the gate switching is due to the Aq moiety rather than DNA, I carried out a control experiment with u-DNA, and did not observe any significant changes in the conductance histogram over the same gate voltage range (Figure 4.11b). A previous study of gate dependent measurement of DNA conductance also failed to detect conductance switching in regular double helical DNA[130]. The control experiment shows that the two-level conductance switching was originated from the redox species Aq moiety.

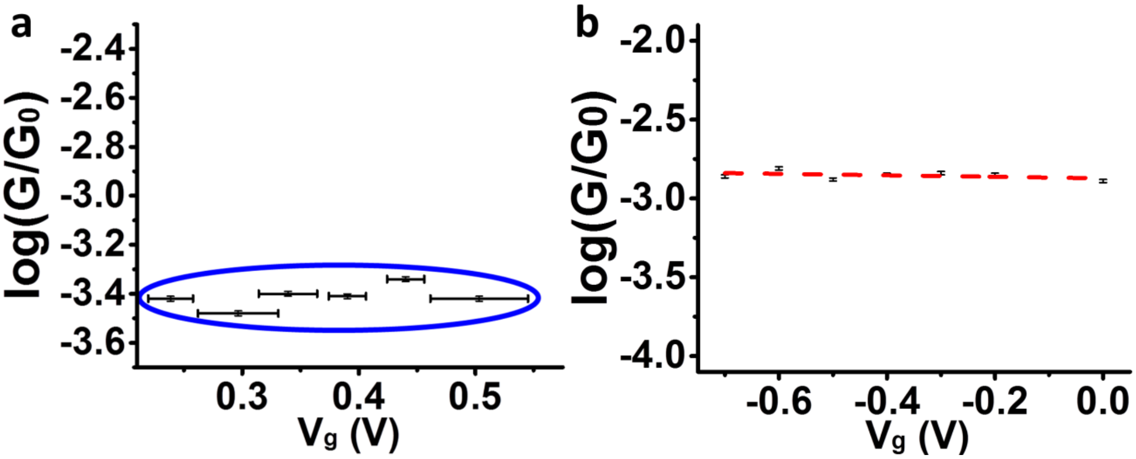

Figure 4.11: Gate dependence of the conductance for Aq-DNA (left) and u-DNA (right). (a) Low conductance values of Aq-DNA vs. gate voltages at gate voltage from 0.2 V to 0.55 V. (b) Conductance of u-DNA vs. gate voltage **(**vs. silver wire quasi-reference electrode), where the red line is a guide to eyes.

The conductance histograms of Aq-DNA, u-DNA and the single-stranded DNA (Figure 4.2) with two thiol terminated groups under different gate voltages were shown from Figure 4.12 to Figure 4.17.

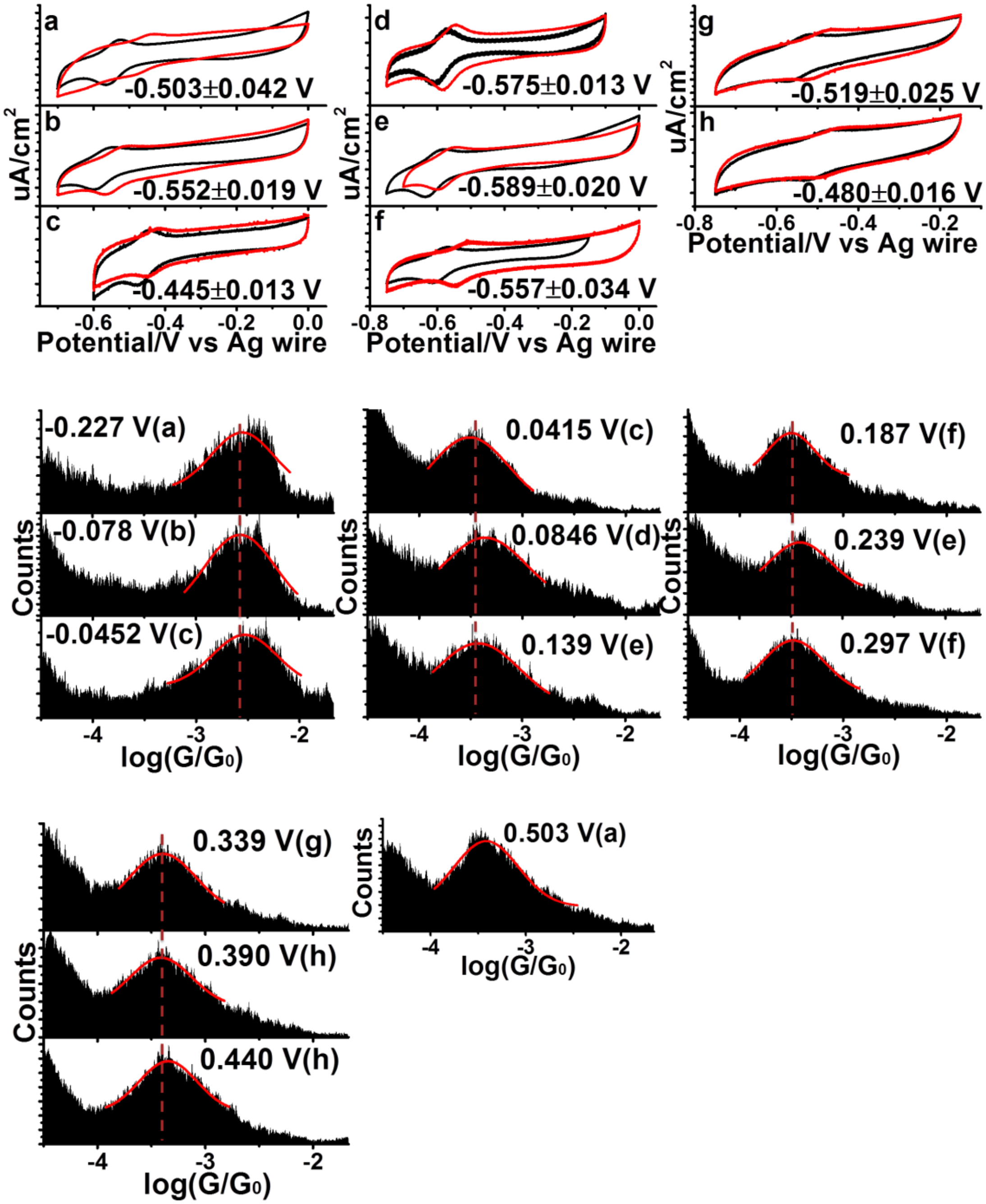

Figure 4.12: Cyclic voltammograms (CVs) before and after electrochemical gate controlled conductance measurements and conductance histograms of Aq-DNA**.** Note that the applied gate voltage was shown in each conductance histogram, where the label

(a, b, … or h) marks the corresponding CV in the first panel. The black and red curves are the CVs before and after the conductance measurement, respectively. The shifts in the redox peaks were taken as error bars in the gate voltages. The applied gate voltage is far away from the redox potential of Aq, thus only one peak was given in each of the conductance histograms.

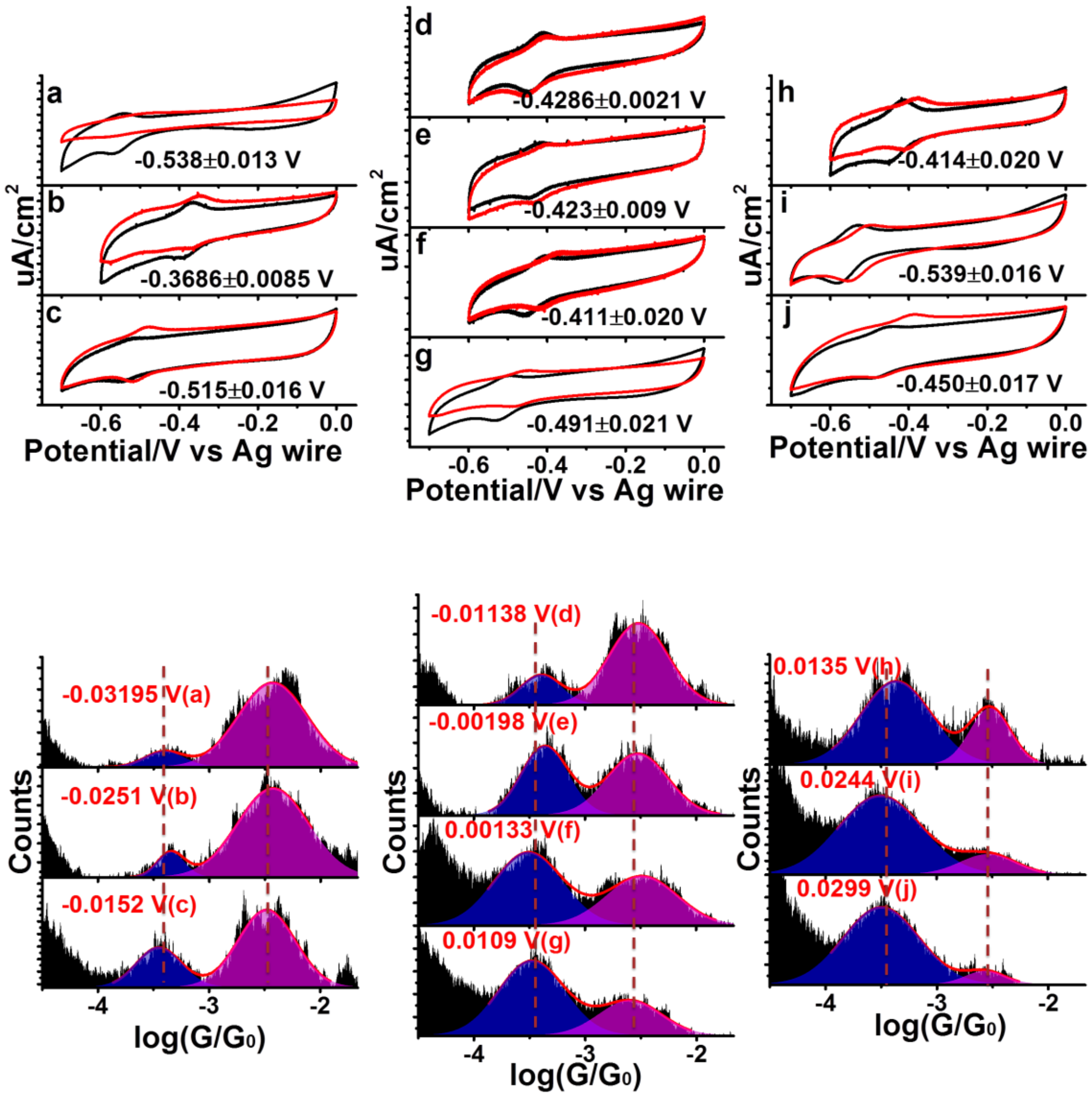

Figure 4.13: Cyclic voltammograms (CV) of Aq-DNA before and after electrochemical gate controlled conductance measurements and high and low conductance peaks in the

conductance histograms, where the red solid lines in the lower panel are Two-Gaussian fitting to the conductance peaks. The applied gate voltage is close to the redox potential of Aq, thus two peaks were given in each of the conductance histograms.

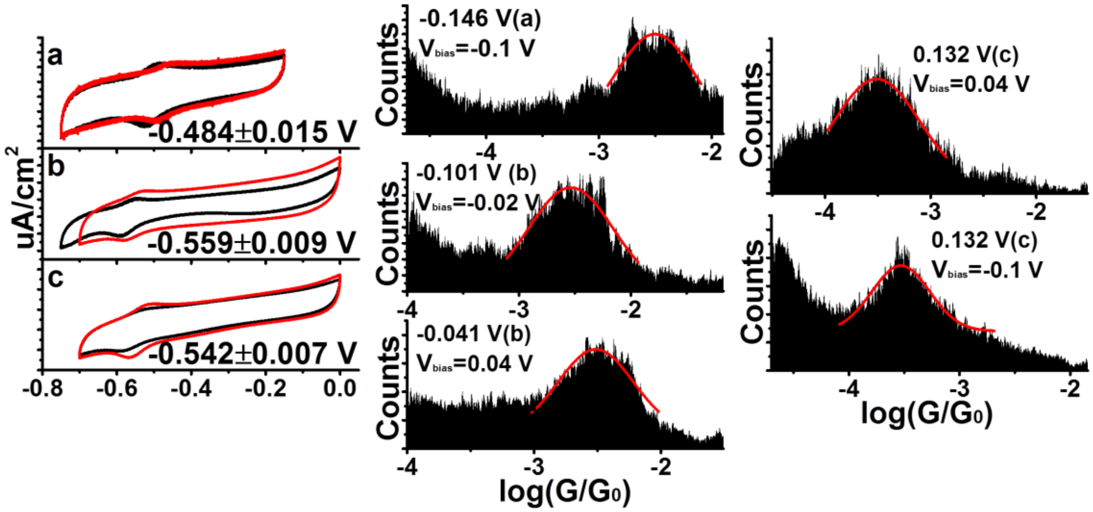

Figure 4.14: Cyclic voltammograms (CVs) before and after electrochemical gate controlled conductance measurements and conductance histograms of Aq-DNA, where the bias voltages are shown in the conductance histograms. These show that the conductance of low and high conductance peak is not dependent on bias voltage or bias polarity.

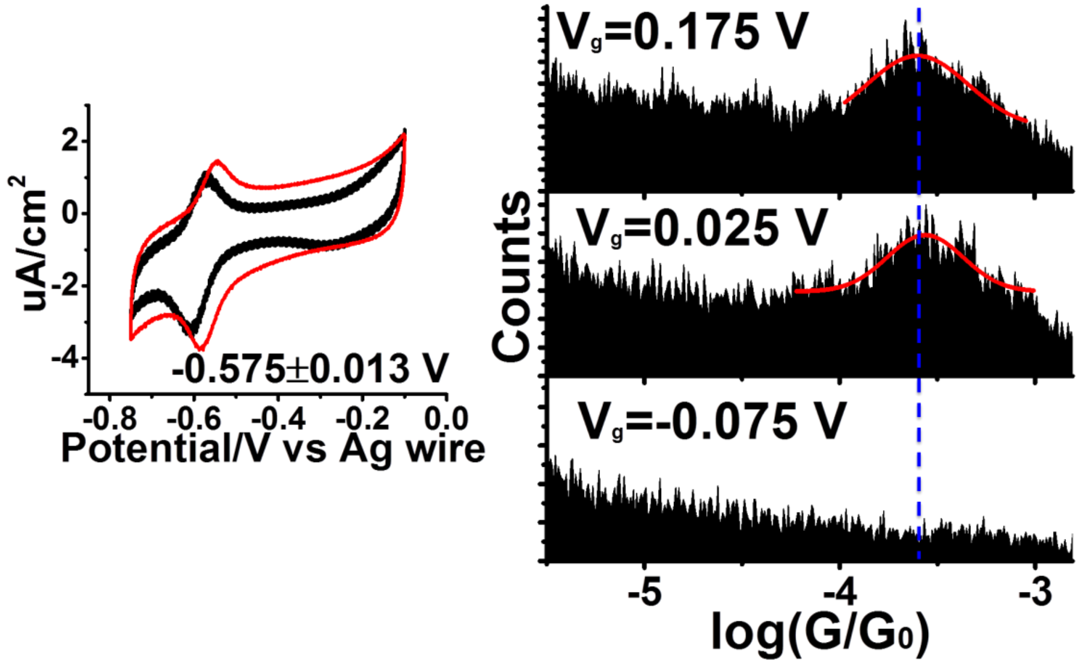

Figure 4.15: Cyclic voltammograms (CVs) before and after electrochemical gate controlled conductance measurements and conductance histograms of Aq-DNA. The applied gate voltages were marked in the conductance histograms. There are no conductance peaks in the range from ~$10^{-5.5}$ to ~10^{-4} G_0. Note that the whole conductance range is from ~$10^{-5.5}$ to ~$10^{-2.8}$ G_0, different from Figure 4.12 to 4.14.

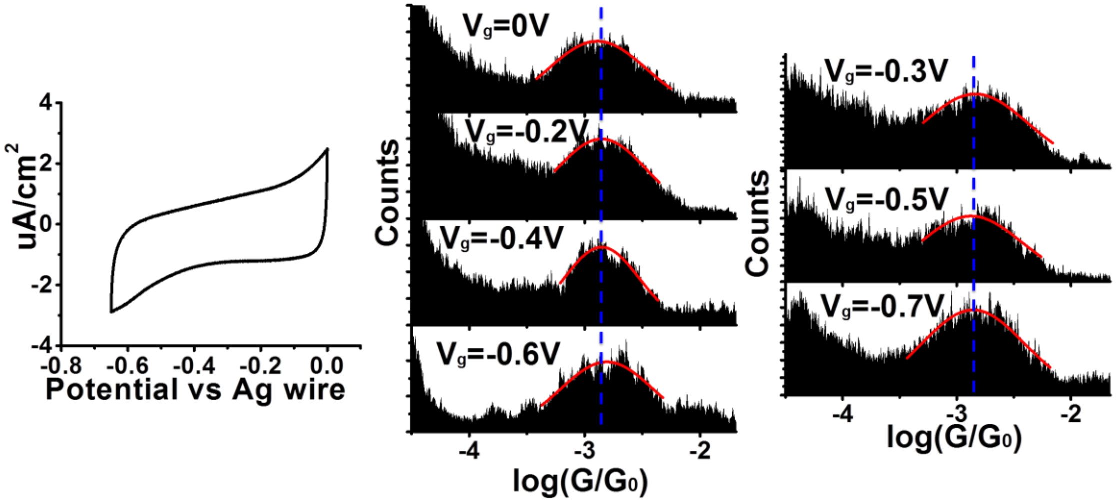

Figure 4.16: Conductance histogram of u-DNA at different applied gate voltages and cyclic voltammograms (CV). Note that the CV does not show redox peaks.

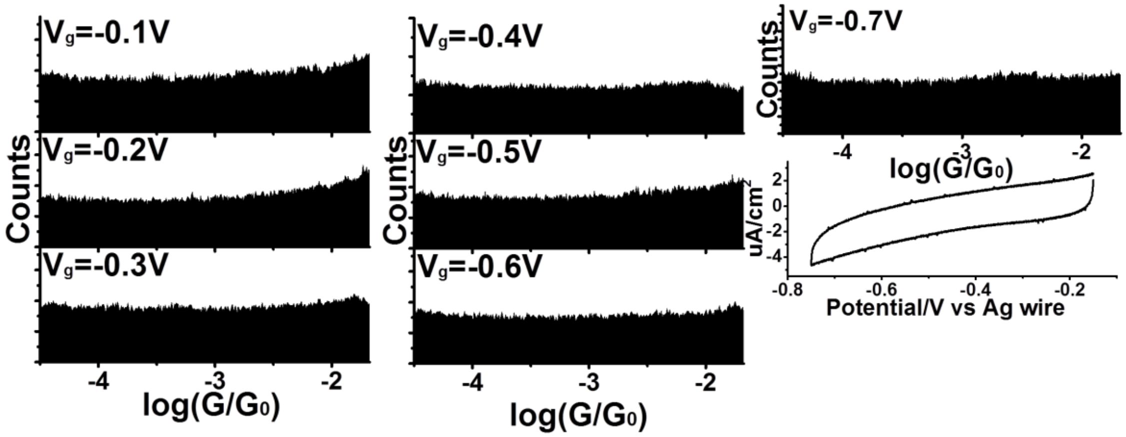

Figure 4.17: Conductance histograms of ssDNA with two thiolate linkers at different gate voltages and cyclic voltammogram (CV). Note that the CV does not show redox peaks.

4.7 Peak areas in the conductance histogram with two conductance peaks

I further analyzed the gate-voltage dependence of the peaks in the conductance histograms of Aq-DNA by calculating the peak areas at different gate voltage (Figure 4.19a). This analysis allows us to determine the relative probability of Aq-DNA in the oxidized and reduced states at each gate voltage because the peak area S is expected to be proportional to the number of Aq-DNA in the corresponding states Γ. To confirm that there are only two conductance states, I checked the conductance ranging from 3.2×10^{-6} to 2.5×10^{-2} G_0 and did not detect any other conductance peaks (see Figure 4.15). Also, it is unlikely that more than one DNA molecule could bridge between the tip and substrate, due to repulsion between the negatively charged DNA. Thus I attribute each of the individual current-distance traces in the conductance histograms to one single DNA molecular junction. In this way, the peak area S in a conductance histogram can be expressed by[131]:

$$S = n_j \cdot \frac{Lf}{vU}\text{, Equation 4.1}$$

where n_j is the number of molecular junctions (traces that have plateau), L is the length of the plateau regime, or step length, f is the sampling frequency, v is the pulling rate in nm/s and U is the bin number in the conductance histogram. The step lengths L for the two conductance states are the same (see Figure 4.18), so the peak area S is proportional to the number of molecular junctions, n_j.

In STM break junction experiment, n_j can be expressed as:

$$n_j = N \cdot Y\text{, Equation 4.2}$$

Where *N* is the total current-distance trace collected and *Y* is the chance of forming a molecular bridge during one current-distance trace. The oxidized state and reduced state were measured under the same circumstance (e.g. same solution, temperature, Au tip and substrate), and their structures only differ by the Aq moiety. Therefore, I conclude that the *Y* is proportional to the surface coverage of the species Γ. Thus ideally the peak area *S* is proportional to Γ.

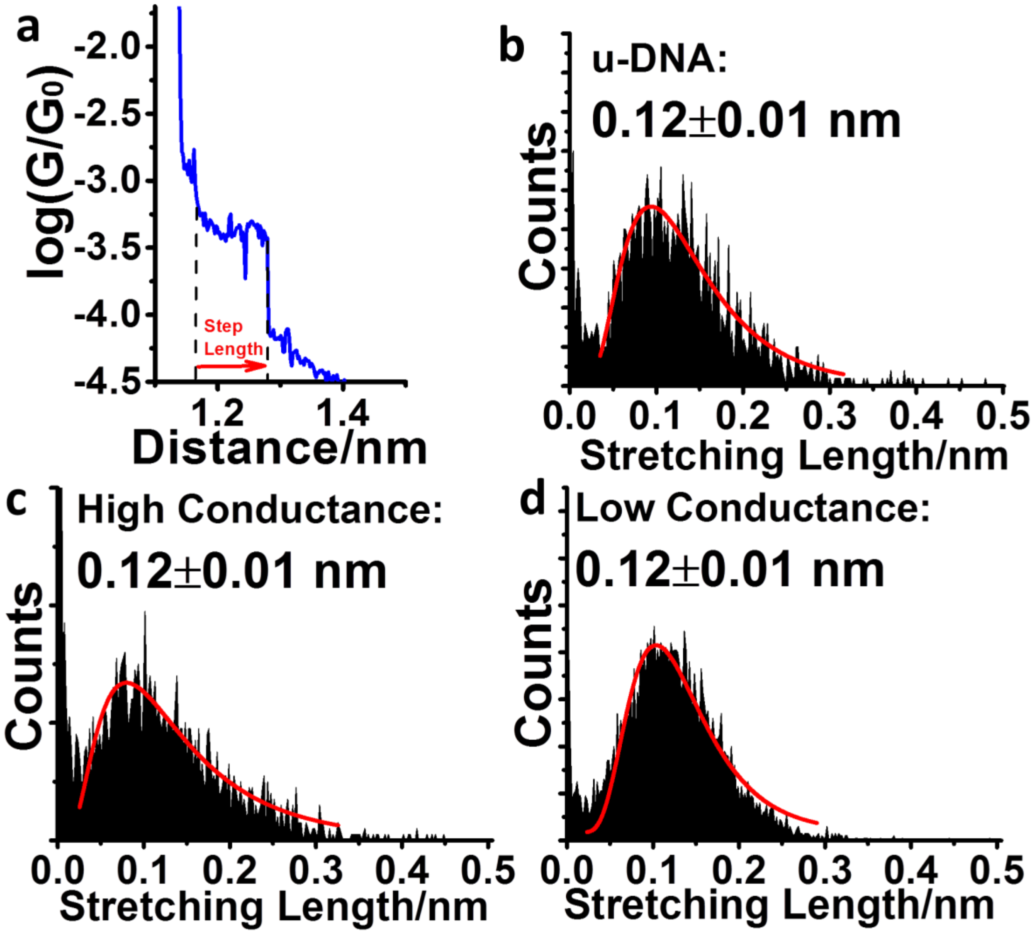

Figure 4.18: Step length histogram for Aq-DNA and u-DNA. (a). Step length is the distance over which a molecular junction can be stretched before breakdown, which corresponds to the length of the conductance plateau in the current-distance traces. (b)-(d).

Step length histograms for u-DNA, high conductance state of Aq-DNA and low conductance state of Aq-DNA. The peaks were fitted with a lognormal distribution and the mean values were taken as the step length. Errors were the fitting errors.

The probability of oxidized Aq-DNA vs. the gate voltage shows a sigmoidal dependence (black points in Figure 4.19b). The result shown in Figure 4.19b was obtained from the statistical analysis of single molecule measurement, which can be compared with the cyclic voltammetry that measures a large number of DNA molecules. As shown in Figure 4.7, the cyclic voltammetry reveals oxidation and reduction peaks, and integration of the peak areas provides the amount of charge transfer (Q). Because the number of charge involved in the oxidation (reduction) of Aq-moiety is 2, I determined the percentage of the molecules in the oxidized state at different gate voltages[132], and the result is plotted together with the single molecule data from the conductance histograms in Figure 4.19b (see Figure 4.13 for details). Note that forward (blue curve) and reverse (magenta curve) gate sweeping curves display hysteresis, but both have the sigmoidal shape. The hysteresis was due to that the charge transfer rate between the electrode and Aq moiety is comparable to the sweeping rate[59]. The data obtained from the single molecule measurement falls in between the forward and reverse gate sweeping curves. This is expected because each data point was measured by holding the gate at a fixed voltage, corresponding to an extremely slow scanning rate.

The relative probability of Aq-DNA in the oxidized and reduced states at thermal equilibrium is expected to follow the Nernst Equation,

$$E = E_{\mathrm{ox/red}} + 2.303\frac{RT}{nF}\log\left(\frac{\Gamma_{\mathrm{ox}}}{\Gamma_{\mathrm{red}}}\right), \text{ Equation 4.3}$$

where E is the gate voltage and $E_{\mathrm{ox/red}}$ is the redox potential of anthraquinone (gate voltage= $E - E_{\mathrm{ox/red}}$), n is the number of charge transfer per molecule, R is the universal gas constant, T is the temperature in K and F is the faraday constant. Γ_{ox} and Γ_{red} are the numbers of the DNA molecules in the oxidized and reduced states, which are proportional to the probabilities of oxidation and reduction, and can be determined from the areas of oxidized and reduced peaks (S_{ox} and S_{red}) in the conductance histograms. Figure 4.19c plots log($S_{\mathrm{ox}}/S_{\mathrm{red}}$) vs. gate voltage ($V_g$), and fitting the data with Nernst Equation yields n=2.0 ±0.4 for n. This value is expected for anthraquinone, which is a prototypical reversible redox species with a two-electron transfer process. The agreement between the single molecule conductance measurement and the Nernst Equation provides further evidence that the observed conductance switching in Aq-DNA is controlled by the redox state of the Aq moiety.

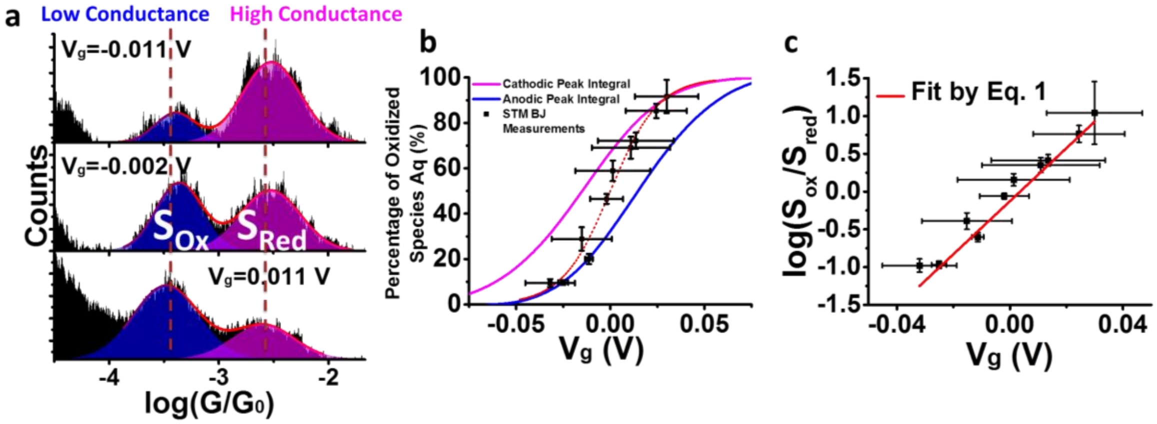

Figure 4.19: Thermodynamic analysis of the two-level conductance switching. **(a)** Conductance histograms at different gate voltages (V_g), where the red lines are Gaussian

fits, from which the areas of the low (S_{ox}) and high (S_{red}) conductance peaks are determined. **(b)** Percentage of Aq-DNA in the oxidized form vs. gate voltage obtained from the reduction (magenta curve) and oxidation (blue curve) peaks in the cyclic voltammograms with a sweeping rate of 0.1 V/s, and the high and low conductance peaks in the conductance histograms. Red dashed line is guide to eye. **(c)** Log(S_{ox}/S_{red}) vs. gate voltages (V_g) and fitting of the data with the Nernst Equation (red line).

The magenta curve and blue curve were obtained by integrating the cathodic peak and anodic peak in the cyclic voltammogram of Aq-DNA modified Au substrate at a sweeping rate of 0.1 V/s. The calculation method is described in Figure 4.20.

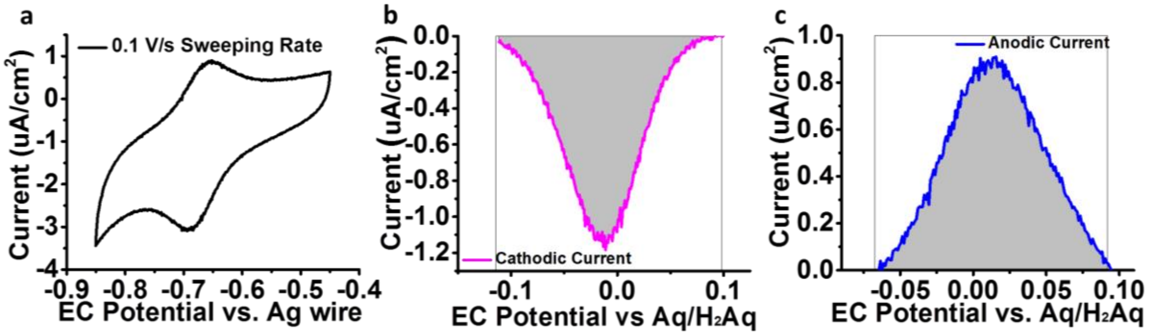

Figure 4.20: Percentage of the oxidized species (Aq) obtained by integrating the cathodic and anodic peaks in the cyclic voltammogram (CV) under 0.1 V/s sweeping rate. **(a).** Cyclic voltammogram obtained with 0.1 V/s sweeping rate, from which a cathodic peak and anodic peak were determined after baseline correction. Note: A silver wire was used as quasi-reference electrode to be consistent with the STM break junction experiments. The redox potential was determined by averaging the cathodic peak and anodic peak. **(b).** Cathodic peak in the CV. **(c).** Anodic peak in the CV. Note: The potential in b and c are

quoted with respect to the redox potential of anthraquinone. The areas of the cathodic and anodic peaks provide the number of molecules participated in the redox reaction.

4.8 Conductance-time histogram and kinetics study

The conductance histogram analysis described above provides averaged properties of single DNA conductance switching events. To further understand conductance switching in DNA, I also studied the individual conductance switching events by monitoring the DNA conductance (G) over time (t) at different gate voltages. I first detected a plateau regime in a conductance-distance trace (grey points Figure 4.21a) at a fixed gate voltage[110], which corresponds to the formation of a DNA junction between the tip and substrate electrodes, and then froze the tip in position while recording the conductance (G) vs. time (t) for 0.1 s.

Figure 4.21b shows four representative G-t curves at a gate voltage of 0 ±0.005 V, each starts when the conductance is at the high conductance level, or Aq-DNA in the reduced state. The four G-t curves illustrate three types of conductance changes over time. Type 1 (30-40% probability): The conductance fluctuates but does not change large enough to be attributed to the switching of the redox state within the 0.1 s time window (black curve). This type of small conductance fluctuations is commonly observed in single molecule junctions, which are attributed to the atomic scale rearrangement in the molecule-electrode contact[127, 128]. Type 2 (20%): The conductance drops abruptly to the noise level, signaling the breakdown of a molecular junction (red curve). This type is also a characteristic of single molecules junctions, arising from the finite lifetime in the molecule-electrode contact[133-135]. Type 3 (40%~50%): The conductance switches from the high level to a lower level (blue curve), or switches back and forth between the high and low levels (magenta curve). The high level conductance is about an order of magnitude higher than the low level conductance. This two-level conductance switching is a unique feature of Aq-DNA, which measures reversible switching of the molecule between oxidized and reduced states. To confirm this conclusion, I performed control experiment with u-DNA and did not observe Type 3 switching behaviors (Figure 4.28).

To further analyze the two-level transient conductance switching, I constructed a 2D G-t histogram for Type 1&3 conductance curves (Figure 4.21c). The 2D histogram reveals two distinct bands at the high and low conductance levels, which confirms the two-level switching of the Aq-DNA redox state discussed earlier. When the gate voltage is close to zero, one expects equal probabilities of finding Aq-DNA in the reduced and oxidized states. Figure 4.21d shows the conductance histogram at t = 0 and 0.1 s, which indeed shows that if the molecule starts at the high conductance level (reduced state), the probabilities of high (reduced state) and low (oxidized state) conductance levels equalizes over time. Similar results were observed when the molecule starts at the low conductance level (oxidized state) (Figure 4.27).

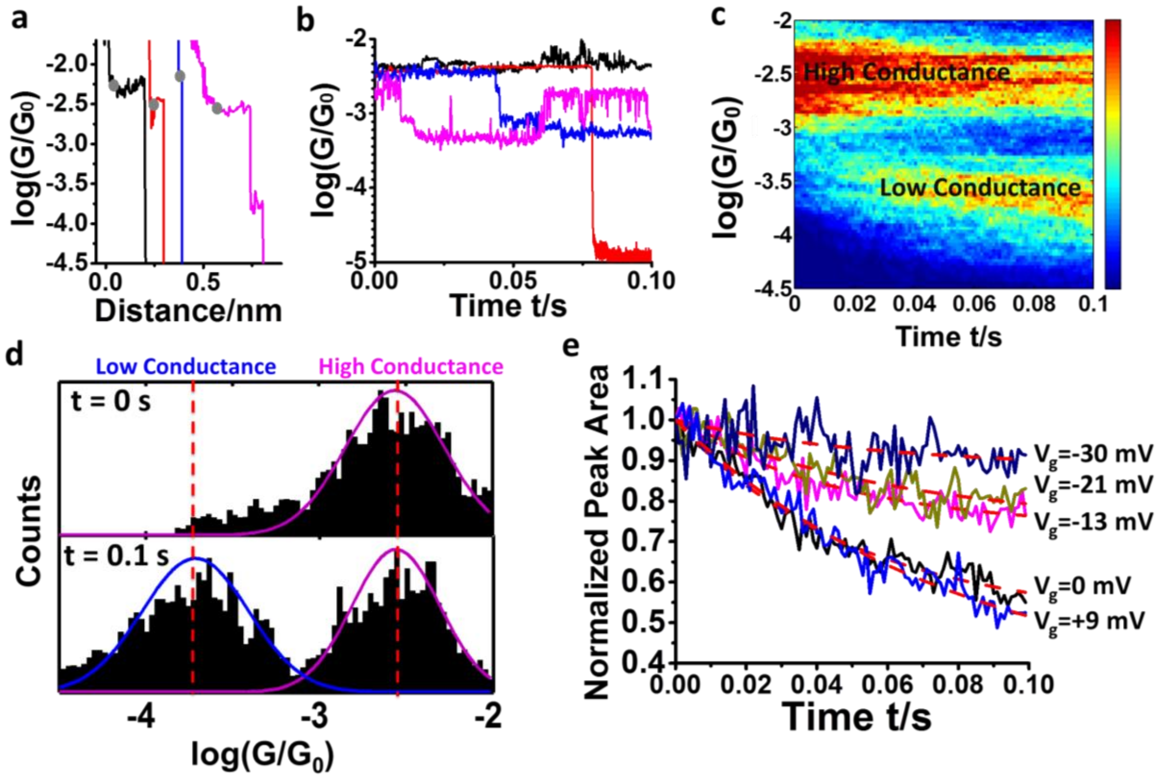

Figure 4.21: Individual conductance switching events and kinetic analysis of redox reactions in single DNA molecules**. (a)** Conductance vs. distance traces, each shows a plateau that corresponds to a DNA molecule bridged between the tip (source) and substrate (drain). The grey dots mark the locations where the tip was fixed in position, and conducting switching events vs. time were studied. **(b)** Three conductance switching behaviors: conductance stays at the high conductance level over the time window (black), conductance switches to the low conductance level and stays at that level (blue) and conductance switches back and forth between the two levels (magenta). Note that red trace shows that conductance drops to zero, due to the breakdown of the DNA junction. See text for more details. **(c)** 2D conductance (G) vs. time (t) histogram with the gate voltage (V_g) set at 0 ±0.005 V, showing two discrete conductance bands, and dependence on time. **(d)** Conductance histogram at t=0 and 0.1 s, showing transition from high

conductance state to a mixture of high and low conductance states. **(e)** Normalized peak area of the high conductance peak vs. time under different gate voltages, where the red dashed lines are the fitting of the curves with the rate Equation (Equation 4.6).

The 2D G-t histogram shown in Figure 4.21c describes the evolution of the high and low conductance states over time, from which I extracted kinetic constants of redox switching at the single molecule level. At a given time, I obtained a conductance histogram like the ones plotted in Figure 4.21d, which shows the histogram at t=0 and 0.1 s. The peak area reflects the probabilities of the molecule in reduced and oxidized states at the given time. Figure 4.21e plots the normalized peak area of the high conductance state (reduced state) vs. time at different gate voltages. The peak area decays over time with a rate that depends on the gate voltage. The more positive is the gate voltage (V_g), the faster it decays, which is expected because the probability of Aq-DNA switching from the high conductance reduced state to the low conductance oxidized state increases with the gate voltage. This process can be described with a kinetic model[136] that is used in electrochemical study of DNA charge transport[137, 138],

$$H_2Aq \underset{k_b}{\overset{k_f}{\rightleftharpoons}} Aq + 2e^- + 2H^+, \text{ Equation 4.4}$$

where k_f and k_b are forward and backward rate constants, respectively, which are related by

$$k_f / k_b = K = \Gamma_{\text{ox}} / \Gamma_{\text{red}}, \text{ Equation 4.5}$$

where K is the equilibrium constant that depends on V_g according to Equation 4.3. The probability of Aq-DNA remaining in the reduced state, p can be expressed as

$$p = \frac{k_f e^{-(k_b+k_f)t} + k_b}{k_b + k_f}, \quad \text{Equation 4.6}$$

By fitting the decay curve at $V_g = 0 \pm 0.005$ V (black curve in Figure 4.21e) with Equation 4.6, I found that $k_f = 9.8 \pm 0.3\ s^{-1}$ and $k_b = 10 \pm 1\ s^{-1}$. These values are within the range of charge transfer rate constants obtained from electrochemistry study on DNA charge transfer[67, 125, 139]. Using these rate constants, I obtained Γ_{ox}/Γ_{red} with Equation 4.5, and substituting it into Equation 4.3 leads to $V_g = 0 \pm 0.002$ V, which is consistent with the actual applied gate voltage. I carried out the experiment at other gate voltages and found the fitted and actual gate voltages agree with each other (Figure 4.23 to Figure 4.26), which further confirms the kinetic model.

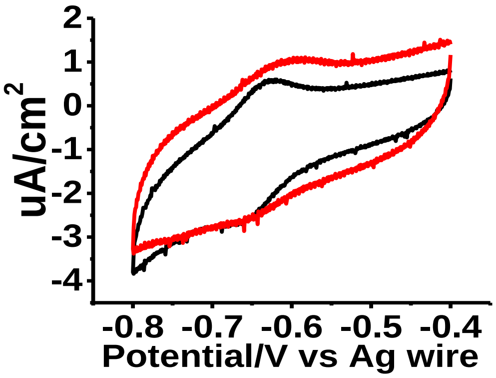

Figure 4.22: Cyclic voltammograms at $V_g = 0 \pm 5$ mV (before and after the conductance measurements). The 2D G-t histogram is shown in Figure 4.21.

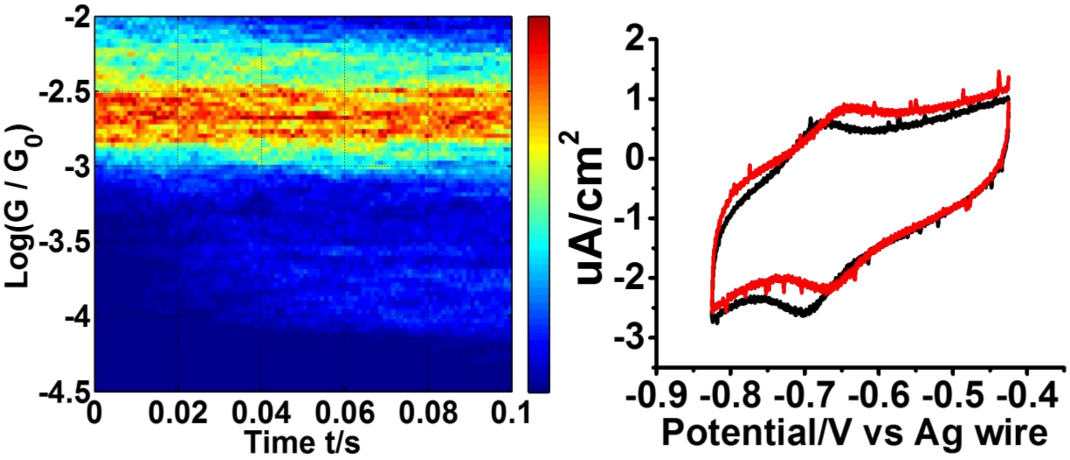

Figure 4.23: 2D conductance-time (G-t) histogram at V_g = -30 ±17 mV and cyclic voltammograms (before and after the conductance measurements).

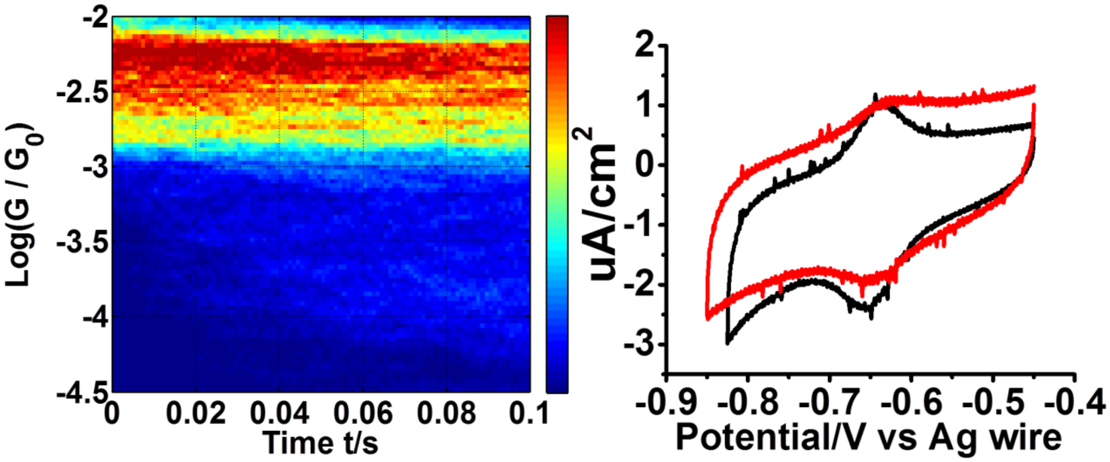

Figure 4.24: 2D conductance-time (G-t) histogram at V_g = -21 ±7 mV and cyclic voltammograms (before and after the conductance measurements).

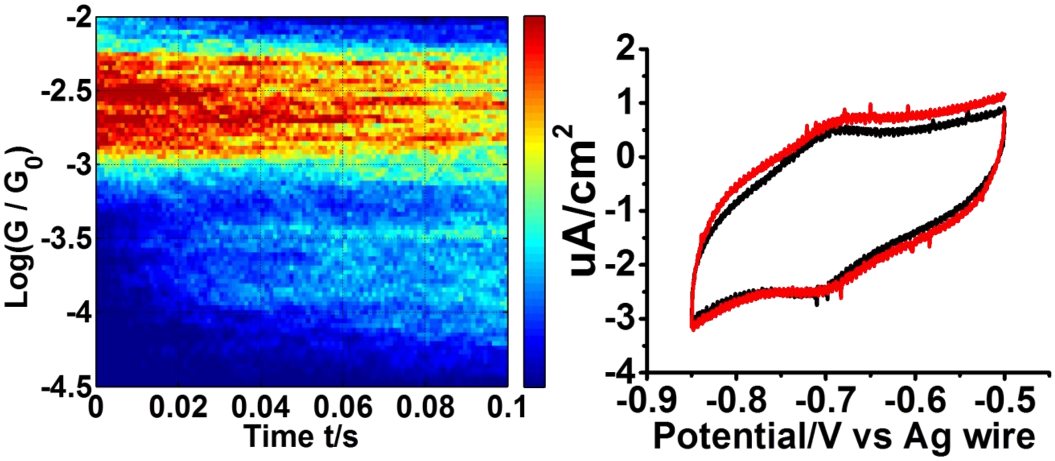

Figure 4.25: 2D conductance-time (G-t) histogram at V_g = -13±8 mV and cyclic voltammograms (before and after the conductance measurements).

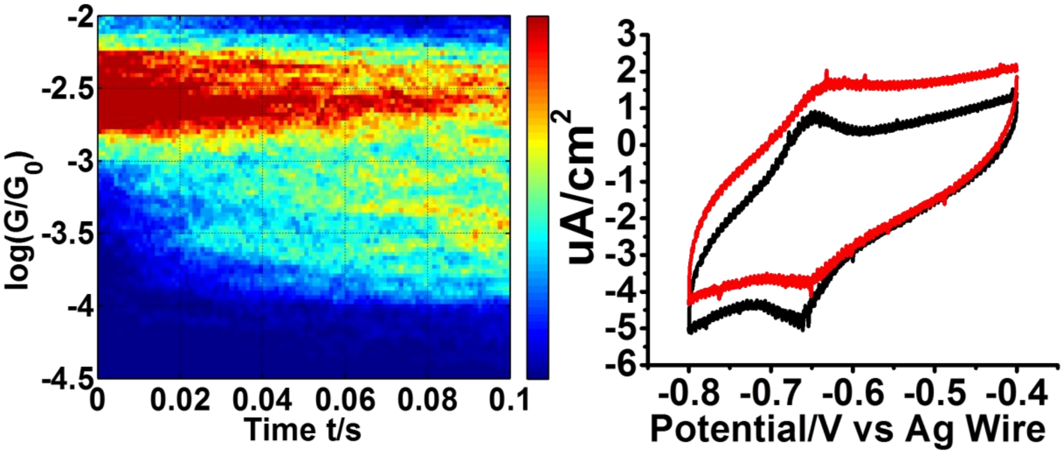

Figure 4.26: 2D conductance-time (G-t) histogram at V_g = 9±10 mV and cyclic voltammograms (before and after the conductance measurements).

By fitting the curves in Figure 4.21e (The peak area of the high conductance states versus time plot in the 2D G-t histograms) with Equation 4.6, I was able to obtain k_f and k_b. Combing these values with Equation 4.3, the fitted gate voltages can be determined to compare with the applied gate voltages. Those values were listed in Table 4.2.

Table 4.2: k_f and k_b values, fitted gate voltages and the applied gate voltages from 2D G-t histograms.

k_f	k_b	Fitted V_g/mV	Applied V_g/mV
8.49+0.30	4.0+0.9	9+3	9+10
9.78+0.34	10.0+1.0	0+2	0+5
5.65+0.38	15.3+2.2	-13+3	-13+8
4.17+0.37	12.0+2.7	-13+4	-21+7
2.09+0.58	16+9	-25+11	-30+17

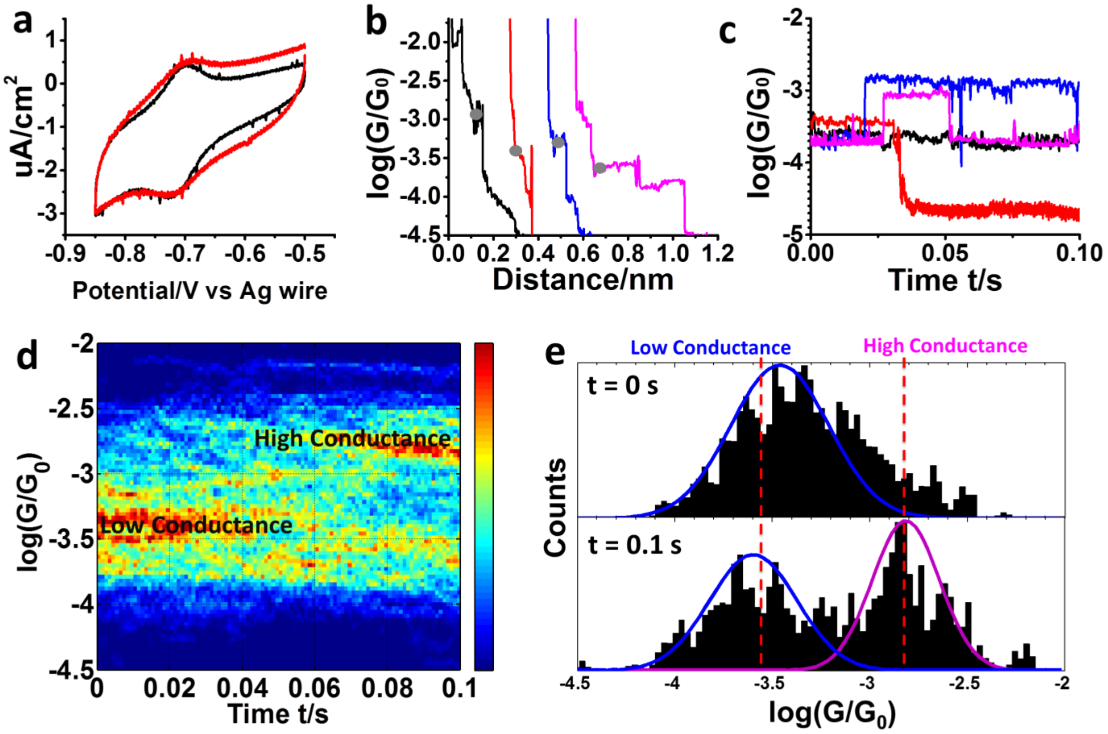

Figure 4.27: 2D G-t histogram study started with the low conductance state of Aq-DNA. **(a).** cyclic voltammograms (before and after the conductance measurements). **(b).** Conductance-distance trace with plateau at low conductance was detected. Then the tip was fixed in position (grey points) and held for 0.1 s while the current was recorded. **(c).** Similar to Figure 4.21b, three major types of conductance-time (G-t) traces were observed (black, red and blue traces). A few of the traces have multiple switching events occurring (magenta trace). **(d).** 2D G-t histogram showing two bands. As the low conductance band fades away with time, and the high conductance starts to appear. **(e).** 1D conductance histograms at t = 0 and t = 0.1 s, showing the switching from low conductance state to high conductance state.

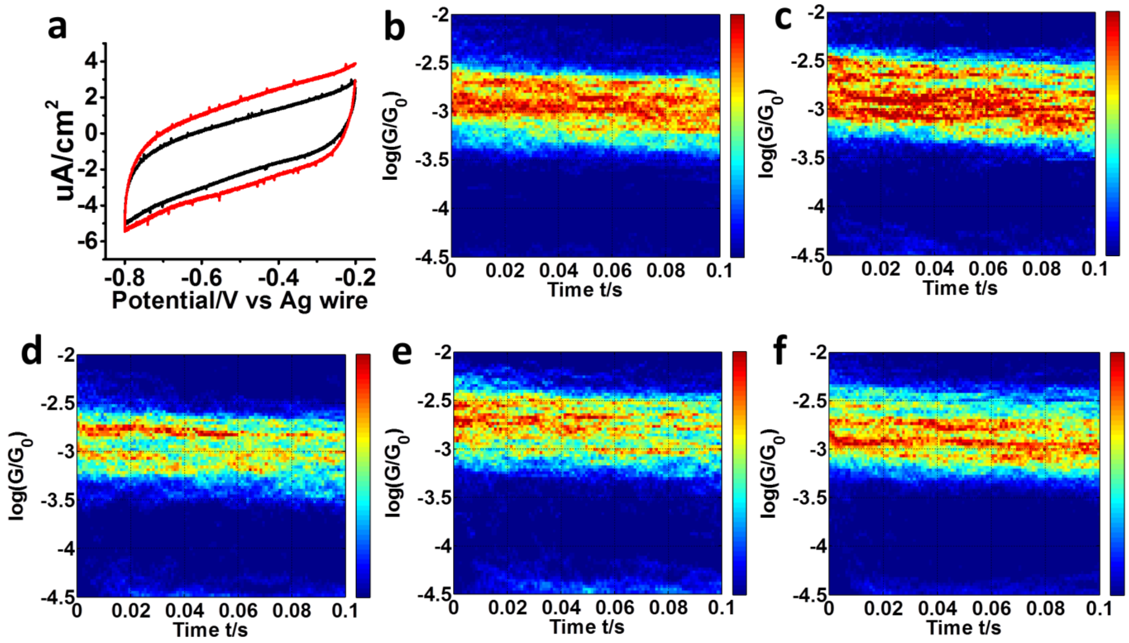

Figure 4.28: 2D conductance-time (G-t) histogram at different gate voltages and cyclic voltammograms for u-DNA. **(a).** Cyclic voltammograms (before and after the conductance measurements) for u-DNA, showing no redox peaks. **(b)-(f).** 2D G-t histograms at V_g of -0.65 V, -0.60 V, -0.55 V, -0.50 V and -0.45 V, showing only one band, which is consistent with the conductance measurement at difference gate voltages in Figure 4.11b.

4.9 Explanation of the conductance difference between the two states

The above analysis shows that the kinetic model developed for redox reactions can describe the observed conducting switching in Aq-DNA. However, the kinetic model cannot explain why the conductance in the reduced state is much greater than that in the oxidized state. To understand the conductance difference between the two states, ZINDO/S theoretical calculations were carried out. Two molecular fragments, G-Aq-G:C (oxidized state) and G-H_2Aq-G:C (reduced state), were built based on the canonical B-DNA structure and the 2KK5 of the Protein Data Bank (PDB)[119]. It is widely accepted that charge transport through DNA is hopping through the guanine HOMO[71, 79, 87], so only on the Aq and H_2Aq molecular levels that are the closest to the guanine HOMO level is considered. The calculation shows that the Aq HOMO and the H_2Aq HOMO-1 levels are the closest to the guanine HOMO level (Figure 4.29). Furthermore, the molecular orbitals of the Aq HOMO and H_2Aq HOMO-1 have similar spatial distributions; both are mainly localized at the anthraquinone moiety. Finally, Aq and H_2Aq have similar coupling strengths with neighboring guanine bases (Table 4.3), but their energy level alignments are different. The H_2Aq HOMO-1 level is ~0.6 eV closer to the guanine HOMO levels compared to the Aq HOMO level. The closer energy level alignment explains the higher Aq-DNA conductance in the reduced state than that in the oxidized state. The observation is consistent with other reported results[38, 113, 140-142], which shows the conductance of anthraquinone in the reduced state is more conductive than that in the oxidized state.

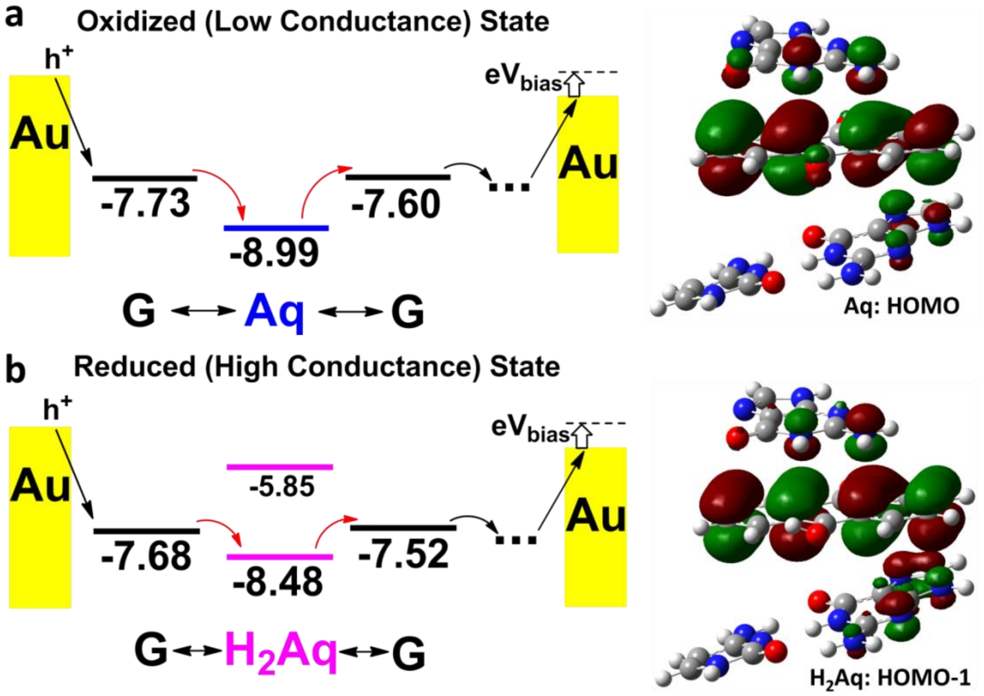

Figure 4.29: Energy diagram for the charge transport and molecular orbital spatial distribution in oxidized state and reduced state. **(a)** For oxidized state, HOMO level of Aq is the closest to the HOMO levels of Guanine. Hole hops from the left Guanine (non-paired) to Aq, then to the right Guanine (paired with C) as indicated by the red arrows. Molecular orbital spatial distribution indicates the HOMO level mainly localized on Aq. **(b)** For reduced state, HOMO-1 level of H_2Aq is the closest to the HOMO levels of Guanine. Comparing to the oxidized state, the energy alignment between H_2Aq and Guanines is better. Molecular orbital spatial distribution also indicates the HOMO-1 level mainly localized on H_2Aq. The unit is eV for all the energy levels.

Table 4.3: Coupling strengths from the calculation (unit is eV).

	HOMO of Aq	HOMO of H_2Aq	HOMO-1 of H_2Aq
Non-paired Guanine	0.27	0.29	0.07
Paired Guanine	0.06	0.13	0.16

4.10 Conclusions and perspectives

This chapter demonstrates one can introduce an active control to DNA conductance by modifying a base with a redox group, and switch the DNA conductance reversibly between two levels by oxidizing or reducing the redox group with an electrochemical gate. This strategy could be implemented in more sophisticated DNA nanostructures for active device building blocks. As the DNA conductance is an indicator of the molecule in the reduced or oxidized state, it is possible to study redox reaction kinetics at the single molecule level by monitoring the DNA conductance.

The anthraquinone modification in this chapter can only be implemented at the 3'-end or 5'-end of a DNA sequence, due to the limitation on the synthetic route. If modification can be applied into the internal strand of a DNA sequence, then multiple anthraquinone modifications can be introduced into a more complicated DNA structure. This could lead to more complicated logic controls (e.g. a "AND" control or a "OR" control) in DNA nanostructure. Moreover, many other redox active groups, such as methylene blue, nile blue and ferrocene can also be introduced into a DNA sequence, which opens up the route towarding the study of multiple-switch controlled DNA molecular junction. By controlling the redox states of multiple groups, on may switch the electric properties of DNA between multiple states. Introducing redox active groups into DNA is an efficient strategy to realize the device application based on DNA, especially for building up three-terminal devices.

CHAPTER 5

CONCLUSIONS AND PERSPECTIVES

The central dogma of molecular biology[143] tells us DNA is the most important and fundamental molecule in the biological system (Figure 5.1a). In the past two decades, people used different experimental methods and keep trying to understand the charge transport/transfer properties through DNA molecules, including this thesis. First, I introduce the field of molecular electronics and summarize the study of DNA charge transport/transfer using other experimental techniques. Then in the chapter 2 of this thesis, I studied two simple series of DNA sequences with alternating GC and stacked GC sequences respectively[104]. I found a new intermediate tunneling-hopping transport mechanism through stacked GC sequences. Coherence can exists over a distance of 2-3 GC base pairs in DNA duplex. This helps us better understand the role of coherence in biological electron transfer process. In the chapter 3, I utilized the G-quadruplex structure and constructed a single molecular charge splitter based on DNA. By connecting DNA duplex to DNA G-quadruplex in different ways, I found the charge transport efficiency is sensitive to the stacking conformation at the connection point. A flexible connection (PEG linker) and less DNA duplexes will facilitate the transport efficiency. This helps us understand the basic principles when one starts to build up more sophisticated electronic devices based on complicated DNA nanostructures. In the chapter 4, I constructed a single molecular switch with precisely controlled two discrete states by modified one

DNA base with a redox group (anthraquinone) via electrochemical gate-controlled STM-BJ technique. I systematically studied the thermodynamics and kinetics of this switching behavior. I hope this study can shed light on building up single molecular three-terminal devices based on DNA in the future. In sum, I think that charge transport/transfer process is the language which biomolecules (DNA, RNA and proteins) use to communicate between them. The studies not only aim to understanding those biological processes in our body, but also trying to learn from them to realize device application and make some changes to our society.

The central dogma of molecular biology[143] tells us that DNA means life, but something that it didn't tell us is the role of water molecule. A lot of studies support that water plays an important role in the charge transport process in our human bodies[144-146]. Water molecule may directly gate the transport through DNA (Figure 5.1b). Moreover, scientists believe that "life origins from water". During the searching for life in our universe, the first priority task is to find water. For example, a lot of studies have confirmed the existing of liquid water on Mars[147-150], which could potentially lead to the finding of life. Comparing to DNA, RNA and protein, water molecule is much simpler but more difficult to study. Studying the charge transport/transfer through DNA, RNA and protein can be an important topic, but the study of water molecule can be another interesting topic as well. After its rapid developments in the past two decades, the field of molecular electronics is seeking to utilize its chemical and physical principles to solve the most frontier issues in the biological systems.

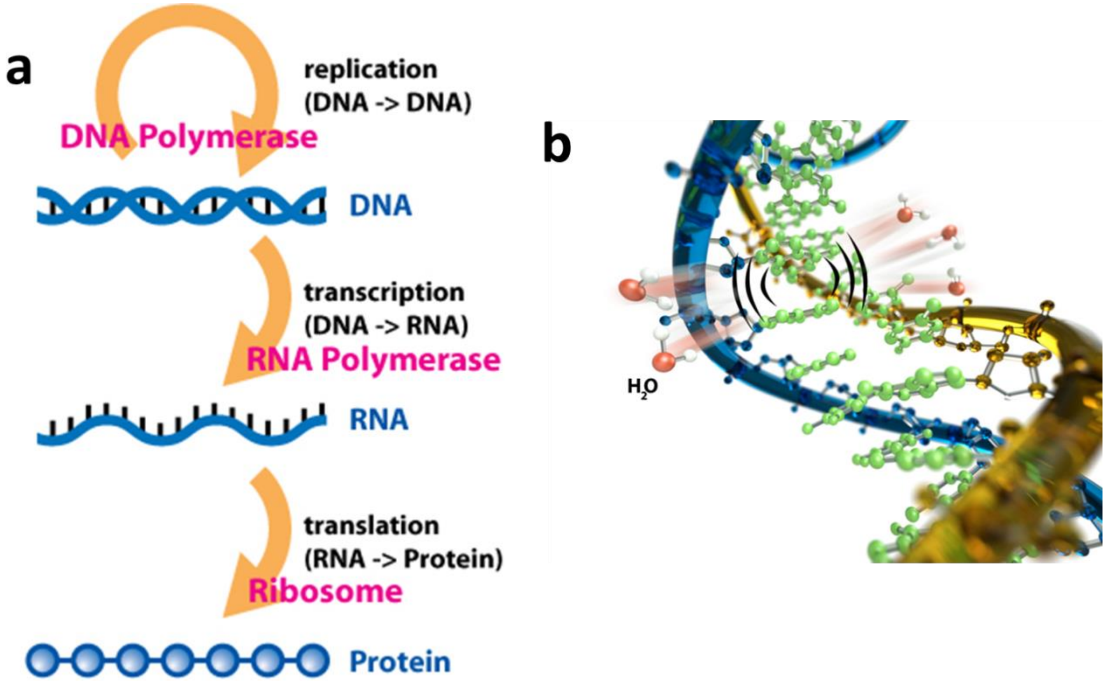

Figure 5.1: DNA in biological system and the water molecule. (a) The central dogma of molecular biology. DNA replicates to produce itself. DNA transcription generates RNA under the help of RNA polymerase. RNA translation generates protein in ribosome. Reprinted with permission from the website of “en.wikipedia”. (b) Water molecule surrounding DNA. Credit to George Foulsham, University of California, Santa Barbara.

REFERENCES

1. Nitzan, A. Electron Transmission Through Molecules and Molecular Interfaces. *Annu. Rev. Phy. Chem.* **52**, 681-750 (2001).

2. Aviram, A. & Ratner, M.A. Molecular rectifiers. *Chem. Phys. Lett.* **29**, 277-283 (1974).

3. Anariba, F. & McCreery, R.L. Electronic Conductance Behavior of Carbon-Based Molecular Junctions with Conjugated Structures. *J. Phys. Chem. B* **106**, 10355-10362 (2002).

4. Slowinski, K., Fong, H.K.Y. & Majda, M. Mercury−Mercury Tunneling Junctions. 1. Electron Tunneling Across Symmetric and Asymmetric Alkanethiolate Bilayers. *J. Am. Chem. Soc.* **121**, 7257-7261 (1999).

5. Holmlin, R.E. *et al.* Electron Transport through Thin Organic Films in Metal−Insulator−Metal Junctions Based on Self-Assembled Monolayers. *J. Am. Chem. Soc.* **123**, 5075-5085 (2001).

6. Blum, A.S. *et al.* Molecularly inherent voltage-controlled conductance switching. *Nature Mater.* **4**, 167-172 (2005).

7. Kushmerick, J.G. *et al.* Effect of Bond-Length Alternation in Molecular Wires. *J. Am. Chem. Soc.* **124**, 10654-10655 (2002).

8. Kim *et al.* Temperature and Length Dependence of Charge Transport in Redox-Active Molecular Wires Incorporating Ruthenium(II) Bis(σ-arylacetylide) Complexes. *J. Phys. Chem. C* **111**, 7521-7526 (2007).

9. Leatherman, G. *et al.* Carotene as a Molecular Wire: Conducting Atomic Force Microscopy. *J. Phys. Chem. B* **103**, 4006-4010 (1999).

10. Cui, X.D. *et al.* Reproducible Measurement of Single-Molecule Conductivity. *Science* **294**, 571-574 (2001).

11. Kelley, T.W., Granstrom, E. & Frisbie, C.D. Conducting Probe Atomic Force Microscopy: A Characterization Tool for Molecular Electronics. *Adv. Mater.* **11**, 261-264 (1999).

12. Xu, B. & Tao, N.J. Measurement of Single-Molecule Resistance by Repeated Formation of Molecular Junctions. *Science* **301**, 1221-1223 (2003).

13. Venkataraman, L., Klare, J.E., Nuckolls, C., Hybertsen, M.S. & Steigerwald, M.L. Dependence of single-molecule junction conductance on molecular conformation. *Nature* **442**, 904-907 (2006).
14. Haiss, W. *et al.* Redox State Dependence of Single Molecule Conductivity. *J. Am. Chem. Soc.* **125**, 15294-15295 (2003).
15. Reed, M.A., Zhou, C., Muller, C.J., Burgin, T.P. & Tour, J.M. Conductance of a Molecular Junction. *Science* **278**, 252-254 (1997).
16. Smit, R.H.M. *et al.* Measurement of the conductance of a hydrogen molecule. *Nature* **419**, 906-909 (2002).
17. Reed, M.A. *et al.* The Electrical Measurement of Molecular Junctions. *Ann. N. Y. Acad. Sci.* **852**, 133-144 (1998).
18. Song, H. *et al.* Observation of molecular orbital gating. *Nature* **462**, 1039-1043 (2009).
19. Lee, T. *et al.* Comparison of Electronic Transport Characterization Methods for Alkanethiol Self-Assembled Monolayers†. *J. Phys. Chem. B* **108**, 8742-8750 (2004).
20. Andres, R.P. *et al.* Coulomb Staircase at Room Temperature in a Self-Assembled Molecular Nanostructure. *Science* **272**, 1323-1325 (1996).
21. Chen, J., Reed, M.A., Rawlett, A.M. & Tour, J.M. Large On-Off Ratios and Negative Differential Resistance in a Molecular Electronic Device. *Science* **286**, 1550-1552 (1999).
22. Joachim, C. & Ratner, M.A. Molecular electronics: Some views on transport junctions and beyond. *Proc. Natl. Acad. Sci. U. S. A.* **102**, 8801-8808 (2005).
23. Metzger, R.M. Unimolecular Electronics. *Chem. Rev.* **115**, 5056-5115 (2015).
24. Sedghi, G. *et al.* Comparison of the Conductance of Three Types of Porphyrin-Based Molecular Wires: β,meso,β-Fused Tapes, meso-Butadiyne-Linked and Twisted meso-meso Linked Oligomers. *Adv. Mater.* **24**, 653-657 (2012).
25. Luo, L., Choi, S.H. & Frisbie, C.D. Probing Hopping Conduction in Conjugated Molecular Wires Connected to Metal Electrodes. *Chem. Mater.* **23**, 631-645 (2011).
26. Ho Choi, S., Kim, B. & Frisbie, C.D. Electrical Resistance of Long Conjugated Molecular Wires. *Science* **320**, 1482-1486 (2008).

27. Haiss, W. *et al.* Anomalous length and voltage dependence of single molecule conductance. *PhysChemChemPhys* **11**, 10831-10838 (2009).
28. Zhao, X. *et al.* Oligo(aryleneethynylene)s with Terminal Pyridyl Groups: Synthesis and Length Dependence of the Tunneling-to-Hopping Transition of Single-Molecule Conductances. *Chem. Mater.* **25**, 4340-4347 (2013).
29. Song, H., Reed, M.A. & Lee, T. Single Molecule Electronic Devices. *Adv. Mater.* **23**, 1583-1608 (2011).
30. Díez-Pérez, I. *et al.* Rectification and stability of a single molecular diode with controlled orientation. *Nature Chem.* **1**, 635-641 (2009).
31. Nerngchamnong, N. *et al.* The role of van der Waals forces in the performance of molecular diodes. *Nature Nanotech.* **8**, 113-118 (2013).
32. Capozzi, B. *et al.* Single-molecule diodes with high rectification ratios through environmental control. *Nature Nanotech.* **10**, 522-527 (2015).
33. Elbing, M. *et al.* A single-molecule diode. *Proc. Natl. Acad. Sci. U. S. A.* **102**, 8815-8820 (2005).
34. Diez-Perez, I. *et al.* Gate-controlled electron transport in coronenes as a bottom-up approach towards graphene transistors. *Nat. Commun.* **1**, 31 (2010).
35. Park, H. *et al.* Nanomechanical oscillations in a single-C60 transistor. *Nature* **407**, 57-60 (2000).
36. Osorio, H.M. *et al.* Electrochemical Single-Molecule Transistors with Optimized Gate Coupling. *J. Am. Chem. Soc.* (2015).
37. Li, Z. *et al.* Regulating a Benzodifuran Single Molecule Redox Switch via Electrochemical Gating and Optimization of Molecule/Electrode Coupling. *J. Am. Chem. Soc.* **136**, 8867-8870 (2014).
38. Baghernejad, M. *et al.* Electrochemical Control of Single-Molecule Conductance by Fermi-Level Tuning and Conjugation Switching. *J. Am. Chem. Soc.* **136**, 17922-17925 (2014).
39. Moreno-García, P. *et al.* Charge Transport in C60-Based Dumbbell-type Molecules: Mechanically Induced Switching between Two Distinct Conductance States. *J. Am. Chem. Soc.* **137**, 2318-2327 (2015).
40. He, J. *et al.* Switching of a Photochromic Molecule on Gold Electrodes: Single-molecule Measurements. *Nanotechnology* **16,** 695-702 (2005).

41. Su, T.A., Li, H., Steigerwald, M.L., Venkataraman, L. & Nuckolls, C. Stereoelectronic switching in single-molecule junctions. *Nature Chem.* **7**, 215-220 (2015).
42. Repp, J., Liljeroth, P. & Meyer, G. Coherent electron-nuclear coupling in oligothiophene molecular wires. *Nature Phys.* **6**, 975-979 (2010).

43. Donhauser, Z.J. *et al.* Conductance Switching in Single Molecules Through Conformational Changes. *Science* **292**, 2303-2307 (2001).

44. Gittins, D.I., Bethell, D., Schiffrin, D.J. & Nichols, R.J. A nanometre-scale electronic switch consisting of a metal cluster and redox-addressable groups. *Nature* **408**, 67-69 (2000).

45. Mujica, V., Kemp, M. & Ratner, M.A. Electron conduction in molecular wires. I. A scattering formalism. *J. Chem. Phys.* **101**, 6849-6855 (1994).

46. Li, X. *et al.* Conductance of Single Alkanedithiols: Conduction Mechanism and Effect of Molecule−Electrode Contacts. *J. Am. Chem. Soc.* **128**, 2135-2141 (2006).

47. Xiao, Xu & Tao Conductance Titration of Single-Peptide Molecules. *J. Am. Chem. Soc.* **126**, 5370-5371 (2004).

48. He, J. *et al.* Electronic Decay Constant of Carotenoid Polyenes from Single-Molecule Measurements. *J. Am. Chem. Soc.* **127**, 1384-1385 (2005).

49. Yamada, R., Kumazawa, H., Noutoshi, T., Tanaka, S. & Tada, H. Electrical Conductance of Oligothiophene Molecular Wires. *Nano Lett.* **8**, 1237-1240 (2008).

50. Nitzan, A. The relationship between electron transfer rate and molecular conduction 2. The sequential hopping case. *Isr. J. Chem.* **42**, 163-166 (2002).

51. Li, C. *et al.* Charge Transport in Single Au | Alkanedithiol | Au Junctions: Coordination Geometries and Conformational Degrees of Freedom. *J. Am. Chem. Soc.* **130**, 318-326 (2008).

52. Park, J. *et al.* Coulomb blockade and the Kondo effect in single-atom transistors. *Nature* **417**, 722-725 (2002).

53. Kubatkin, S. *et al.* Single-electron transistor of a single organic molecule with access to several redox states. *Nature* **425**, 698-701 (2003).

54. Capozzi, B. *et al.* Tunable Charge Transport in Single-Molecule Junctions via Electrolytic Gating. *Nano Lett.* **14**, 1400-1404 (2014).

55. Mujica, V., Nitzan, A., Datta, S., Ratner, M.A. & Kubiak, C.P. Molecular Wire Junctions: Tuning the Conductance. *J. Phys. Chem. B* **107**, 91-95 (2003).

56. Kasibhatla, B.S.T. *et al.* Reversibly Altering Electronic Conduction through a Single Molecule by a Chemical Binding Event. *J. Phys. Chem. B* **107**, 12378-12382 (2003).

57. Piva, P.G. *et al.* Field regulation of single-molecule conductivity by a charged surface atom. *Nature* **435**, 658-661 (2005).

58. Xiao, X., Xu, B. & Tao, N. Changes in the Conductance of Single Peptide Molecules upon Metal-Ion Binding. *Angew. Chem. Int. Ed.* **43**, 6148-6152 (2004).

59. Migliore, A. & Nitzan, A. Irreversibility in redox molecular conduction: single versus double metal-molecule interfaces. *Electrochim. Acta* **160**, 363-375 (2015).

60. Giese, B.A., J. Kohler, A.-K.; Spormann, M.; Wessely, S. Direct observation of hole transfer through DNA by hopping between adenine bases and by tunneling. *Nature* **412**, 318 (2001).

61. Lewis, F.D. *et al.* Distance-Dependent Electron Transfer in DNA Hairpins. *Science* **277**, 673-676 (1997).

62. Lewis, F.D., Letsinger, R.L. & Wasielewski, M.R. Dynamics of Photoinduced Charge Transfer and Hole Transport in Synthetic DNA Hairpins. *Acc. Chem. Res.* **34**, 159-170 (2000).

63. Lewis, F.D., Zhu, H., Daublain, P., Cohen, B. & Wasielewski, M.R. Hole Mobility in DNA A Tracts. *Angew. Chem. Int. Ed.* **45**, 7982-7985 (2006).

64. Kelley, S.O., Jackson, N.M., Hill, M.G. & Barton, J.K. Long-Range Electron Transfer through DNA Films. *Angew. Chem. Int. Ed.* **38**, 941-945 (1999).

65. CellArnold, Anna R., Grodick, Michael A. & Barton, Jacqueline K. DNA Charge Transport: from Chemical Principles to the Cell. *Cell Chem. Bio.* **23**, 183-197 (2016).

66. Laviron, E. General expression of the linear potential sweep voltammogram in the case of diffusionless electrochemical systems. *J. Electroanal. Chem. Interfac.* **101**, 19-28 (1979).

67. Pheeney, C.G. & Barton, J.K. DNA Electrochemistry with Tethered Methylene Blue. *Langmuir* **28**, 7063-7070 (2012).

68. Cohen, H., Nogues, C., Naaman, R. & Porath, D. Direct measurement of electrical transport through single DNA molecules of complex sequence. *Proc. Natl. Acad. Sci. U. S. A.* **102**, 11589-11593 (2005).

69. Xu, Zhang, Li & Tao Direct Conductance Measurement of Single DNA Molecules in Aqueous Solution. *Nano Lett.* **4**, 1105-1108 (2004).

70. Risser, S.M., Beratan, D.N. & Meade, T.J. Electron transfer in DNA: predictions of exponential growth and decay of coupling with donor-acceptor distance. *J. Am. Chem. Soc.* **115**, 2508-2510 (1993).

71. Jortner, J., Bixon, M., Langenbacher, T. & Michel-Beyerle, M.E. Charge transfer and transport in DNA. *Proc. Natl. Acad. Sci. U. S. A.* **95**, 12759-12765 (1998).

72. Conwell, E.M. Charge transport in DNA in solution: The role of polarons. *Proc. Natl. Acad. Sci. U. S. A.* **102**, 8795-8799 (2005).

73. Renaud, N., Berlin, Y.A., Lewis, F.D. & Ratner, M.A. Between Superexchange and Hopping: An Intermediate Charge-Transfer Mechanism in Poly(A)-Poly(T) DNA Hairpins. *J. Am. Chem. Soc.* **135**, 3953-3963 (2013).

74. Roche, S. Sequence Dependent DNA-Mediated Conduction. *Phys. Rev. Lett.* **91**, 108101 (2003).

75. Wang, X.F. & Chakraborty, T. Charge Transfer via a Two-Strand Superexchange Bridge in DNA. *Phys. Rev. Lett.* **97**, 106602 (2006).

76. Wallace, S.S. Biological consequences of free radical-damaged DNA bases1,2. *Free Radic. Biol. Med.* **33**, 1-14 (2002).

77. Kawanishi, S., Hiraku, Y. & Oikawa, S. Mechanism of guanine-specific DNA damage by oxidative stress and its role in carcinogenesis and aging. *Mutat. Res. Rev. Mutat. Res.* **488**, 65-76 (2001).

78. Murphy, C. *et al.* Long-range photoinduced electron transfer through a DNA helix. *Science* **262**, 1025-1029 (1993).

79. Giese, B. Long-Distance Charge Transport in DNA: The Hopping Mechanism. *Acc. Chem. Res.* **33**, 631-636 (2000).

80. Seeman, N.C. Nanomaterials Based on DNA. *Annu. Rev. Biochem.* **79**, 65-87 (2010).

81. Porath, D., Bezryadin, A., de Vries, S. & Dekker, C. Direct measurement of electrical transport through DNA molecules. *Nature* **403**, 635-638 (2000).

82. Fink, H.-W. & Schonenberger, C. Electrical conduction through DNA molecules. *Nature* **398**, 407-410 (1999).

83. Kawai, K. & Majima, T. Hole Transfer Kinetics of DNA. *Acc. Chem. Res.* **46**, 2616-2625 (2013).

84. van Zalinge, H. *et al.* Variable-Temperature Measurements of the Single-Molecule Conductance of Double-Stranded DNA. *Angew. Chem. Int. Ed.* **45**, 5499-5502 (2006).

85. Grib, N.V., Ryndyk, D.A., Gutiérrez, R. & Cuniberti, G. Distance-dependent coherent charge transport in DNA: crossover from tunneling to free propagation. *J. Biophys. Chem.* **01**, 77-85 (2010).

86. Zhang, Y., Liu, C., Balaeff, A., Skourtis, S.S. & Beratan, D.N. Biological charge transfer via flickering resonance. *Proc. Natl. Acad. Sci. U. S. A.* **111**, 10049-10054 (2014).

87. Genereux, J.C. & Barton, J.K. Mechanisms for DNA Charge Transport. *Chem. Rev.* **110**, 1642-1662 (2010).

88. McCreery, R.L. Molecular Electronic Junctions. *Chem. Mater.* **16**, 4477-4496 (2004).

89. Segal, D., Nitzan, A., Ratner, M. & Davis, W.B. Activated Conduction in Microscopic Molecular Junctions. *J. Phy. Chem. B* **104**, 2790-2793 (2000).

90. Voityuk, A.A., Rösch, N., Bixon, M. & Jortner, J. Electronic Coupling for Charge Transfer and Transport in DNA. *J. Phys. Chem. B* **104**, 9740-9745 (2000).

91. Šponer, J., Leszczyński, J. & Hobza, P. Nature of Nucleic Acid−Base Stacking: Nonempirical ab Initio and Empirical Potential Characterization of 10 Stacked Base Dimers. Comparison of Stacked and H-Bonded Base Pairs. *J. Phys. Chem.* **100**, 5590-5596 (1996).

92. Di Felice, R., Calzolari, A., Molinari, E. & Garbesi, A. Ab initio study of model guanine assemblies: The role of coupling and band transport. *Phys. Rev. B* **65**, 045104 (2001).

93. Saito, I. *et al.* Photoinduced DNA Cleavage via Electron Transfer: Demonstration That Guanine Residues Located 5' to Guanine Are the Most Electron-Donating Sites. *J. Am. Chem. Soc.* **117**, 6406-6407 (1995).

94. Berlin, Y.A., Burin, A.L. & Ratner, M.A. Charge Hopping in DNA. *J. Am. Chem. Soc.* **123**, 260-268 (2000).

95. Smit, R.H.M., Untiedt, C., Rubio-Bollinger, G., Segers, R.C. & van Ruitenbeek, J.M. Observation of a Parity Oscillation in the Conductance of Atomic Wires. *Phys. Rev. Lett.* **91**, 076805 (2003).

96. Tada, T., Nozaki, D., Kondo, M., Hamayama, S. & Yoshizawa, K. Oscillation of Conductance in Molecular Junctions of Carbon Ladder Compounds. *J. Am. Chem. Soc.* **126**, 14182-14189 (2004).

97. O'Neil, M.A. & Barton, J.K. DNA Charge Transport: Conformationally Gated Hopping through Stacked Domains. *J. Am. Chem. Soc.* **126**, 11471-11483 (2004).

98. Venkatramani, R. *et al.* Evidence for a Near-Resonant Charge Transfer Mechanism for Double-Stranded Peptide Nucleic Acid. *J. Am. Chem. Soc.* **133**, 62-72 (2011).

99. Buttiker, M. Coherent and sequential tunneling in series barriers. *IBM J. Res. Dev.* **32**, 63-75 (1988).

100. Jortner, J., Bixon, M., Voityuk, A.A. & Rösch, N. Superexchange Mediated Charge Hopping in DNA†. *J. Phys. Chem. A* **106**, 7599-7606 (2002).

101. Liu, T. & Barton, J.K. DNA Electrochemistry through the Base Pairs Not the Sugar−Phosphate Backbone. *J. Am. Chem. Soc.* **127**, 10160-10161 (2005).

102. Conron, S.M.M., Thazhathveetil, A.K., Wasielewski, M.R., Burin, A.L. & Lewis, F.D. Direct Measurement of the Dynamics of Hole Hopping in Extended DNA G-Tracts. An Unbiased Random Walk. *J. Am. Chem. Soc.* **132**, 14388-14390 (2010).

103. Pacher, T., Cederbaum, L.S. & Köppel, H. Approximately diabatic states from block diagonalization of the electronic Hamiltonian. *J. Chem. Phys.* **89**, 7367-7381 (1988).

104. Xiang, L. *et al.* Intermediate tunnelling–hopping regime in DNA charge transport. *Nature Chem.* **7**, 221-226 (2015).

105. Molen, S.J.V.d. *et al.* Visions for a molecular future. *Nature Nanotech.* **8**, 385-389 (2013).

106. Odom, D.T., Dill, E.A. & Barton, J.K. Charge transport through DNA four-way junctions. *Nucleic Acids Res.* **29**, 2026-2033 (2001).

107. Young, R.M. *et al.* Charge Transport across DNA-Based Three-Way Junctions. *J. Am. Chem. Soc.* **137**, 5113-5122 (2015).

108. Venczel, E.A. & Sen, D. Synapsable DNA. *J. Mol. Biol.* **257**, 219-224 (1996).

109. Venkatramani, R., Wierzbinski, E., Waldeck, D.H. & Beratan, D.N. Breaking the simple proportionality between molecular conductances and charge transfer rates. *Farad. Discuss.* **174**, 57-78 (2014).

110. Guo, S., Hihath, J., Díez-Pérez, I. & Tao, N. Measurement and Statistical Analysis of Single-Molecule Current–Voltage Characteristics, Transition Voltage Spectroscopy, and Tunneling Barrier Height. *J. Am. Chem. Soc.* **133**, 19189-19197 (2011).

111. Woiczikowski, P.B., Kubař, T., Gutiérrez, R., Cuniberti, G. & Elstner, M. Structural stability versus conformational sampling in biomolecular systems: Why is the charge transfer efficiency in G4-DNA better than in double-stranded DNA? *J. Chem. Phys.* **133**, 035103 (2010).

112. Livshits, G.I. *et al.* Long-range charge transport in single G-quadruplex DNA molecules. *Nature Nanotech.* **9**, 1040-1046 (2014).

113. Koole, M., Thijssen, J.M., Valkenier, H., Hummelen, J.C. & Zant, H.S.J.v.d. Electric-Field Control of Interfering Transport Pathways in a Single-Molecule Anthraquinone Transistor. *Nano Lett.* **15**, 5569-5573 (2015).

114. Artés, J.M., López-Martínez, M., Díez-Pérez, I., Sanz, F. & Gorostiza, P. Conductance Switching in Single Wired Redox Proteins. *Small* **10**, 2537-2541 (2014).

115. Liljeroth, P., Repp, J. & Meyer, G. Current-Induced Hydrogen Tautomerization and Conductance Switching of Naphthalocyanine Molecules. *Science* **317**, 1203-1206 (2007).

116. Auwarter, W. *et al.* A surface-anchored molecular four-level conductance switch based on single proton transfer. *Nature Nanotech.* **7**, 41-46 (2012).

117. Roldan, D. *et al.* Charge Transport in Photoswitchable Dimethyldihydropyrene-Type Single-Molecule Junctions. *J. Am. Chem. Soc.* **135**, 5974-5977 (2013).

118. Lörtscher, E., Ciszek, J.W., Tour, J. & Riel, H. Reversible and Controllable Switching of a Single-Molecule Junction. *Small* **2**, 973-977 (2006).

119. Patra, A. & Richert, C. High Fidelity Base Pairing at the 3'-Terminus. *J. Am. Chem. Soc.* **131**, 12671-12681 (2009).

120. Berlin, Y.A., Voityuk, A.A. & Ratner, M.A. DNA Base Pair Stacks with High Electric Conductance: A Systematic Structural Search. *ACS Nano* **6**, 8216-8225 (2012).

121. Haug, R., Kramer, M. & Richert, C. Three-Pronged Probes: High-Affinity DNA Binding with Cap, β-Alanines and Oligopyrrolamides. *Chem. Euro. J.* **19**, 15822-15826 (2013).

122. Chen, F. *et al.* A Molecular Switch Based on Potential-Induced Changes of Oxidation State. *Nano Lett.* **5**, 503-506 (2005).

123. Tao, N.J. Probing Potential-Tuned Resonant Tunneling through Redox Molecules with Scanning Tunneling Microscopy. *Phys. Rev. Lett.* **76**, 4066-4069 (1996).

124. Gorodetsky, A.A., Green, O., Yavin, E. & Barton, J.K. Coupling into the Base Pair Stack Is Necessary for DNA-Mediated Electrochemistry. *Bioconjugate Chem.* **18**, 1434-1441 (2007).

125. Abi, A. & Ferapontova, E.E. Unmediated by DNA Electron Transfer in Redox-Labeled DNA Duplexes End-Tethered to Gold Electrodes. *J. Am. Chem. Soc.* **134**, 14499-14507 (2012).

126. Richter, P. Estimating errors in least-squares fitting. *Telecommun. Dat. Acqu. Progres. Rep.* **42-122**, 107-137 (1995).

127. Malen, J.A. *et al.* The Nature of Transport Variations in Molecular Heterojunction Electronics. *Nano Lett.* **9**, 3406-3412 (2009).

128. Quan, R., Pitler, C.S., Ratner, M.A. & Reuter, M.G. Quantitative Interpretations of Break Junction Conductance Histograms in Molecular Electron Transport. *ACS Nano* **9**, 7704-7713 (2015).

129. Huang, C., Rudnev, A.V., Hong, W. & Wandlowski, T. Break junction under electrochemical gating: testbed for single-molecule electronics. *Chem. Soc. Rev.* **44**, 889-901 (2015).

130. Hihath, J., Chen, F., Zhang, P. & Tao, N. Thermal and electrochemical gate effects on DNA conductance. *J. Phy. Conden. Matter* **19**, 215202 (2007).

131. Arielly, R., Vadai, M., Kardash, D., Noy, G. & Selzer, Y. Real-Time Detection of Redox Events in Molecular Junctions. *J. Am. Chem. Soc.* **136**, 2674-2680 (2014).

132. Eckermann, A.L., Feld, D.J., Shaw, J.A. & Meade, T.J. Electrochemistry of redox-active self-assembled monolayers. *Coord. Chem. Rev.* **254**, 1769-1802 (2010).

133. Diez-Perez, I. *et al.* Controlling single-molecule conductance through lateral coupling of [pi] orbitals. *Nature Nanotech.* **6**, 226-231 (2011).

134. Huang, Z., Chen, F., Bennett, P.A. & Tao Single Molecule Junctions Formed via Au−Thiol Contact: Stability and Breakdown Mechanism. *J. Am. Chem. Soc.* **129**, 13225-13231 (2007).

135. Huang, Z. *et al.* Local ionic and electron heating in single-molecule junctions. *Nature Nanotech.* **2**, 698-703 (2007).

136. O'Dea, J.J. & Osteryoung, J.G. Characterization of quasi-reversible surface processes by square-wave voltammetry. *Anal. Chem.* **65**, 3090-3097 (1993).

137. McWilliams, M.A., Bhui, R., Taylor, D.W. & Slinker, J.D. The Electronic Influence of Abasic Sites in DNA. *J. Am. Chem. Soc.* (2015).

138. Wohlgamuth, C.H. *et al.* Electrochemistry of DNA Monolayers Modified With a Perylenediimide Base Surrogate. *J. Phys. Chem. C* **118**, 29084-29090 (2014).

139. Gorodetsky, A.A., Buzzeo, M.C. & Barton, J.K. DNA-Mediated Electrochemistry. *Bioconjugate Chem.* **19**, 2285-2296 (2008).

140. Darwish, N. *et al.* Observation of Electrochemically Controlled Quantum Interference in a Single Anthraquinone-Based Norbornylogous Bridge Molecule. *Angew. Chem. Int. Ed.* **51**, 3203-3206 (2012).

141. Markussen, T., Schiötz, J. & Thygesen, K.S. Electrochemical control of quantum interference in anthraquinone-based molecular switches. *J. Chem. Phys.* **132**, 224104 (2010).

142. Markussen, T., Stadler, R. & Thygesen, K.S. The Relation between Structure and Quantum Interference in Single Molecule Junctions. *Nano Lett.* **10**, 4260-4265 (2010).

143. Crick, F. Central Dogma of Molecular Biology. *Nature* **227**, 561-563 (1970).

144. Lin, J., Balabin, I.A. & Beratan, D.N. The Nature of Aqueous Tunneling Pathways Between Electron-Transfer Proteins. *Science* **310**, 1311-1313 (2005).

145. Khesbak, H., Savchuk, O., Tsushima, S. & Fahmy, K. The Role of Water H-Bond Imbalances in B-DNA Substate Transitions and Peptide Recognition Revealed by Time-Resolved FTIR Spectroscopy. *J. Am. Chem. Soc.* **133**, 5834-5842 (2011).

146. Donaldson, S.H., Lee, C.T., Chmelka, B.F. & Israelachvili, J.N. General hydrophobic interaction potential for surfactant/lipid bilayers from direct force measurements between light-modulated bilayers. *Proc. Natl. Acad. Sci. U. S. A.* **108**, 15699-15704 (2011).

147. Villanueva, G.L. *et al.* Strong water isotopic anomalies in the martian atmosphere: Probing current and ancient reservoirs. *Science* **348**, 218-221 (2015).

148. Di Achille, G. & Hynek, B.M. Ancient ocean on Mars supported by global distribution of deltas and valleys. *Nature Geosci.* **3**, 459-463 (2010).

149. Grotzinger, J.P. *et al.* A Habitable Fluvio-Lacustrine Environment at Yellowknife Bay, Gale Crater, Mars. *Science* **343** (2014).

150. Michalski, J.R. *et al.* Groundwater activity on Mars and implications for a deep biosphere. *Nature Geosci.* **6**, 133-138 (2013).